

**Beyond modelocking: High repetition-rate frequency  
combs derived from a continuous-wave laser**

by

**Daniel C. Cole**

B.S., Washington University in St. Louis, 2012

M.S., University of Colorado, 2015

A thesis submitted to the  
Faculty of the Graduate School of the  
University of Colorado in partial fulfillment  
of the requirements for the degree of  
Doctor of Philosophy  
Department of Physics  
2018

This thesis entitled:  
Beyond modelocking: High repetition-rate frequency combs derived from a continuous-wave laser  
written by Daniel C. Cole  
has been approved for the Department of Physics

---

Scott A. Diddams

---

Reader Two

Date \_\_\_\_\_

The final copy of this thesis has been examined by the signatories, and we find that both the content and the form meet acceptable presentation standards of scholarly work in the above mentioned discipline.

Cole, Daniel C. (Ph.D., Physics)

Beyond modelocking: High repetition-rate frequency combs derived from a continuous-wave laser

Thesis directed by Dr. Scott A. Diddams

Optical frequency combs based on modelocked lasers have revolutionized precision metrology by facilitating measurements of optical frequencies, with implications both for fundamental scientific questions and for applications such as fast, broadband spectroscopy. In this thesis, I describe advances in the generation of frequency combs without modelocking in platforms with smaller footprints and higher repetition rates, with the ultimate goal of bringing frequency combs to new applications in a chip-integrated package. I discuss two approaches for comb generation: parametric frequency conversion in Kerr microresonators and active electro-optic modulation of a continuous-wave laser. After introducing microresonator-based frequency combs (microcombs), I discuss two specific developments in microcomb technology: First, I describe a new, extremely reliable method for generation of soliton pulses through the use of a phase-modulated pump laser. This technique eliminates the dependence on initial conditions that was formerly a universal feature of these experiments, presenting a solution to a significant technical barrier to the practical application of microcombs. Second, I present observations of *soliton crystal* states with highly structured ‘fingerprint’ optical spectra that correspond to ordered pulse trains exhibiting crystallographic defects. These pulse trains arise through interaction of solitons with avoided mode-crossings in the resonator spectrum. I also discuss generation of Kerr soliton combs in the Fabry-Perot (FP) geometry, with a focus on the differences between the FP geometry and the ring geometry that has been the choice of most experimenters to date. Next, I discuss combs based on electro-optic modulation. I introduce the operational principle, and then describe the first self-referencing of a frequency comb of this kind and a proof-of-principle application experiment. Finally, I discuss a technique for reducing the repetition rate of a high repetition-rate frequency comb, which will be a necessary post-processing step for some applications.

## Contents

<b>1</b>	<b>Introduction</b>	<b>1</b>
1.1	Optical frequency combs . . . . .	3
1.1.1	Optical pulse trains and their spectra . . . . .	3
1.1.2	Frequency stabilization of optical pulse trains . . . . .	6
<b>2</b>	<b>Introduction to microresonator-based frequency combs</b>	<b>9</b>
2.1	Optical microring resonators . . . . .	10
2.1.1	Resonant enhancement in a microring resonator . . . . .	12
2.1.2	Thermal effects in microresonators . . . . .	14
2.2	Microring resonator Kerr frequency combs . . . . .	16
2.2.1	A model for Kerr-comb nonlinear optics: The Lugiato-Lefever equation . . . . .	18
2.3	Description of Kerr-comb outputs using the Lugiato-Lefever equation . . . . .	21
2.3.1	Analytical investigation of the resonator's CW response . . . . .	22
2.3.2	Kerr comb outputs: extended modulation-instability patterns . . . . .	25
2.3.3	Kerr comb outputs: solitons . . . . .	28
<b>3</b>	<b>Generation and control of single microresonator solitons using a phase-modulated pump laser</b>	<b>35</b>
3.1	Theoretical investigation of soliton generation with a phase-modulated pump laser . . . . .	36
3.2	Spontaneous generation of single solitons using a phase-modulated pump laser . . . . .	39
3.3	Soliton control using a phase-modulated pump laser . . . . .	42
3.4	Subharmonic phase modulation for high repetition-rate systems . . . . .	44

<b>4</b>	Soliton crystals in microresonators	<b>48</b>
4.1	Spectral and temporal characteristics of soliton crystals . . . . .	49
4.2	Soliton crystal generation . . . . .	50
4.3	Mechanism of soliton crystallization . . . . .	50
4.3.1	Simulation of soliton crystals . . . . .	54
4.4	Case study: pair distribution function for a superstructured crystal . . . . .	55
4.5	Soliton crystal configuration space . . . . .	59
4.6	Time-domain measurements of soliton crystals . . . . .	63
<b>5</b>	Theory of Kerr frequency combs in Fabry-Perot resonators	<b>66</b>
5.1	General relationship between the ring LLE and the FP-LLE . . . . .	69
5.2	Extended patterns in the FP-LLE . . . . .	70
5.3	Solitons in the FP-LLE . . . . .	71
5.3.1	Analytical approximation for solitons in the FP-LLE . . . . .	71
5.3.2	Existence range of single solitons . . . . .	72
5.3.3	Generation of single solitons through laser frequency scans . . . . .	75
<b>6</b>	Microresonator-based frequency combs: Summary and outlook	<b>77</b>
<b>7</b>	A frequency comb generated through active modulation of a continuous-wave laser	<b>80</b>
7.1	Principle of operation . . . . .	80
7.2	Generation of an EOM comb and detection of its carrier-envelope offset frequency .	83
7.3	Noise considerations in EOM comb generation . . . . .	88
7.4	Application: Optical frequency division via double pinning . . . . .	91
7.5	Outlook . . . . .	93
<b>8</b>	Downsampling of optical pulse trains	<b>95</b>
8.1	Proof-of-Concept Experiment . . . . .	97
8.2	Mathematical model for downsampling . . . . .	98

8.3	Experimental investigation of the effect of downsampling on the pulse train's noise properties . . . . .	100
8.4	Effects of ideal downsampling on a pulse train's noise properties . . . . .	102
8.5	Model for the effect of incomplete extinction of rejected pulses and amplification of a downsampled pulse train . . . . .	105
8.6	Further remarks on the application of downsampling . . . . .	108
<b>A</b>	<b>Derivation of the Lugiato-Lefever equation from the nonlinear Schrodinger equation</b>	<b>110</b>
A.1	<i>A posteriori</i> confirmation that $L_D \gg L$ and $L_{NL} \gg L$ for LLE solitons . . . . .	113
A.2	Normalization of the Ikeda map . . . . .	114
<b>B</b>	<b>Numerical simulations of nonlinear optics</b>	<b>115</b>
B.1	RK4IP algorithm . . . . .	115
B.2	Adaptive step-size algorithm . . . . .	116
B.3	Pseudocode for numerical simulation with the RK4IP algorithm and adaptive step size	117
B.3.1	Simulation of the LLE . . . . .	118
B.3.2	Simulation of the GNLSE . . . . .	119
<b>References</b>		<b>121</b>

## Figures

1.1	Optical frequency combs in the time and frequency domains . . . . .	4
1.2	Measurement of the carrier-envelope offset frequency via $f - 2f$ self-referencing . . . . .	8
2.1	Optical microdisk resonator . . . . .	11
2.2	Thermal bistability in microresonators . . . . .	16
2.3	An illustration of four-wave mixing and frequency-comb generation. . . . .	18
2.4	Solution space for the Lugiato-Lefever equation . . . . .	22
2.5	Investigation of the circulating CW power in a Kerr resonator . . . . .	24
2.6	Extended-pattern solutions to the LLE . . . . .	27
2.7	Soliton solutions to the LLE . . . . .	30
2.8	Kerr-soliton energy-level diagram . . . . .	32
3.1	Energy-level diagram with a phase-modulated pump laser . . . . .	36
3.2	Quasi-CW background in a PM-pumped resonator . . . . .	38
3.3	Mechanism for soliton generation with a PM pump . . . . .	40
3.4	Experimental setup for soliton generation with a phase-modulated pump laser . . . . .	41
3.5	Spontaneous generation of solitons using a phase-modulated pump laser . . . . .	42
3.6	Repetition-rate control using a phase-modulated pump laser . . . . .	44
3.7	Repetition-rate switching driven by a phase-modulated pump laser . . . . .	45
3.8	Subharmonic phase modulation for high repetition-rate soliton generation . . . . .	47
4.1	Spectral contrast of a soliton crystal . . . . .	51

4.2	Generation and characterization of a soliton crystal . . . . .	52
4.3	Stabilization and collapse of a soliton crystal . . . . .	56
4.4	Spectrum and waveform of a superstructured soliton crystal . . . . .	57
4.5	Simulated generation of a superstructured soliton crystal . . . . .	58
4.6	Pair distribution function for soliton crystal generation . . . . .	59
4.7	Taxonomy of soliton crystals . . . . .	62
4.8	Cross-correlation characterization of a soliton crystal . . . . .	64
5.1	Relationship between the physical field in the Fabry-Perot cavity and the co-moving field $\psi$ . . . . .	68
5.2	Extended patterns in the FP-LLE . . . . .	71
5.3	Boundaries of soliton existence in the FP-LLE . . . . .	74
5.4	Transition from extended patterns to single solitons in the FP-LLE . . . . .	76
7.1	Operating principle of an electro-optic modulation comb . . . . .	82
7.2	Experimental setup for detection of the carrier-envelope offset frequency of an EOM comb after generation of a coherent supercontinuum . . . . .	84
7.3	Spectral broadening for generation of an octave-spanning supercontinuum . . . . .	86
7.4	Self-referencing of an EOM comb . . . . .	88
7.5	Investigation of the noise properties of the EOM comb . . . . .	90
7.6	Photodetected carrier-envelope-offset frequency signal with different sources for $f_{rep}$ . . . . .	91
7.7	Stable microwave generation with an EOM comb via double pinning . . . . .	92
8.1	An illustration of pulse-train repetition-rate downsampling . . . . .	96
8.2	Demonstration of downsampling for $f_0$ detection . . . . .	98
8.3	Experimental investigation of noise introduced by downsampling . . . . .	101
8.4	Effect of downsampling on photocurrent fluctuations . . . . .	105
8.5	Investigation of incomplete pulse extinction and amplification . . . . .	108

# Chapter 1

## Introduction

The optical frequency comb is a versatile tool for science and technology. Its invention two decades ago initiated a revolution in precision measurement by dramatically improving the resolution with which we can conveniently measure time and frequency [1–5]. This revolution was brought about by advancements in nonlinear optics [6] that enabled the realization of a simple scheme by which the hundreds-of-terahertz-scale optical frequencies of a modelocked laser could be measured electronically, and was facilitated by the development of high performing solid-state femtosecond laser technology such as the Ti:sapphire laser. Since their introduction, optical frequency combs have found important roles in a range of experiments and applications, including the first demonstration of an optical atomic clock [7], systems for ultra-low-noise microwave synthesis [8, 9], broadband spectroscopy applications [10, 11], optical arbitrary waveform generation [12], and stable long-term calibration of astronomical spectrographs for exoplanet detection [13]. Further development of the technology beyond the first stabilization of the Ti:sapphire laser that heralded the frequency comb’s arrival has enabled combs to reach applications across many wavelength bands [14–17]. The technology is reaching maturity, and frequency combs have been commercially available for some time.

In the last decade, methods for generating optical frequency combs without a modelocked laser have emerged. These new frequency combs come with higher repetition rates and lower fundamental size, weight, and power (SWAP) requirements. Higher repetition rates make them particularly attractive for applications where high power per comb mode, individual accessibility of comb modes,

and fast acquisition times are desired; these applications include arbitrary microwave and optical waveform generation, telecommunications, and broadband, temporally-resolved spectroscopy. The lower SWAP requirements of these combs suggest the tantalizing possibility that they could be used in these and other applications outside the laboratory. These combs present a promising route towards truly portable and robust frequency comb technology, which would continue to drive forward the revolution that was initiated some twenty years ago. There remains much work to be done, however, to develop these combs that are based on continuous-wave lasers to the level of technological maturity that has been reached by modelocked-laser-based combs.

This thesis focuses on these new frequency combs, with several related, discrete areas of focus. The bulk of the thesis covers microresonator-based frequency combs (microcombs), and especially the nonlinear dynamics involved in the generation of these frequency combs via the Kerr nonlinearity. An introduction to this field is provided in Chapter 2. Chapters 3-5 describe advancements in the field, and Chapter 6 provides a brief summary and a discussion of avenues for further research on this topic. Then, Chapter 7 presents a second method for generating a high-repetition-rate frequency comb without modelocking that is based on active modulation of a CW seed laser and subsequent nonlinear spectral broadening. The first self-referencing of a comb of this type is described, and a proof-of-principle application to the generation of low-noise microwaves is discussed. An outlook for further development of this type of comb is presented. Finally, in Chapter 8, I present experimental and theoretical investigations of repetition-rate reduction of frequency combs via pulse gating, which may prove useful for adapting low-SWAP combs and their intrinsically high repetition rates to some applications as the technology continues to develop.

In the remainder of this chapter, I discuss the basic properties of frequency combs and explain how the optical frequencies making up a comb can be fully determined by electronics operating with gigahertz-scale bandwidths.

## 1.1 Optical frequency combs

An optical frequency comb is obtained by fully stabilizing the spectrum of an optical pulse train. The first frequency combs came about through full frequency-stabilization of modelocked lasers; this thesis focuses on frequency combs with pulse trains generated through other means.

### 1.1.1 Optical pulse trains and their spectra

In the time domain, a frequency comb consists of a train of uniformly spaced optical pulses arriving at the pulse train's repetition rate  $f_{rep}$ , which within the growing space of frequency comb technology is between  $\sim 10$  MHz and  $\sim 1$  THz; the combs discussed in this thesis have repetition rates between 10 GHz and 30 GHz. In most implementations the pulses are very short compared to the repetition period  $T = 1/f_{rep}$ , with durations on the order of 100 fs. In the frequency domain, the comb consists of a set of modes that are spaced by  $f_{rep}$  in frequency and that have amplitudes determined by an overall spectral envelope centered at the optical carrier frequency  $\nu_c$  ( $\sim 193$  THz in this thesis), with bandwidth inversely related to the temporal duration of the pulses. The usual description of a frequency comb, which is natural for modelocked-laser-based combs that are not derived from a CW laser, gives the frequencies of the comb modes as

$$\nu_n = n f_{rep} + f_0, \quad (1.1)$$

where  $n \sim \nu_c/f_{rep}$  for the optical modes that make up the comb and  $f_0$  is the carrier-envelope offset frequency, which may be defined to be between 0 and  $f_{rep}$ . The offset frequency results from the pulse-to-pulse evolution of the carrier wave underneath the temporal intensity envelope of the pulses due to a difference in group and phase velocities. An equivalent representation of the frequencies of the comb that is more natural for frequency combs directly derived from a CW laser, as described in this thesis, is

$$\nu_\mu = \nu_c + \mu f_{rep}, \quad (1.2)$$

where  $\nu_c$  is the frequency of the CW laser, the ‘pump’ or ‘seed’ laser, from which the frequency comb is derived and  $\mu$  is a pump-referenced mode number, in contrast with the zero-referenced

mode number  $n$  of Eq. 1.1. Now the carrier-envelope offset frequency  $f_0$  is found in the difference between  $\nu_c$  and the closest harmonic of  $f_{rep}$ :  $f_0 = \nu_c - Nf_{rep}$ , where  $N$  is the largest integer such that  $f_0 > 0$ . Fig. 1.1 depicts the properties of a frequency comb in the time domain and the frequency domain.

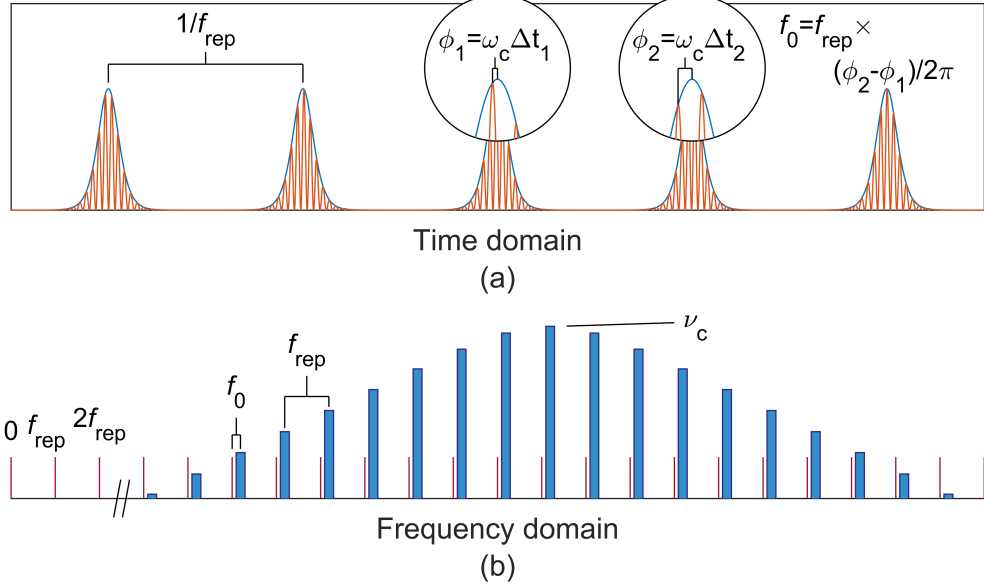


**Figure 1.1: Optical frequency combs in the time and frequency domains.** (a) Time-domain depiction of a frequency comb as a train of pulses spaced by  $1/f_{rep}$ . The intensity envelope is shown in blue, and the carrier wave is shown in orange. The carrier-envelope offset frequency  $f_0$  arises from a phase-slip of the carrier with respect to the intensity envelope from pulse to pulse. Specifically, if phases  $\phi_j = \omega_c \Delta t_j$  are traced out by the carrier wave between its maximum and the  $j^{\text{th}}$  peak of the pulse train, then  $f_0 = \frac{\phi_{j+1} - \phi_j}{2\pi} f_{rep}$ . (b) Frequency-domain depiction of the same frequency comb. The comb modes (shown in blue) are centered around an optical frequency  $\nu_c$  and offset from harmonics of the repetition rate  $f_{rep}$  (shown in red) by a frequency shift  $f_0$ . Note that the x-axis has been broken, and the zero-referenced mode numbers of the comb modes shown are large, e.g.  $n \sim 19340$  for a 10 GHz repetition-rate comb centered at 1550 nm wavelength (see Chapter 7).

It is useful to consider a mathematical treatment of an optical pulse train to understand the relationships presented above. In the time domain, the electric field  $E(t)$  of the pulse train consists of optical pulses that arrive periodically and have baseband (centered at zero frequency) field envelope  $A(t)$  multiplying the carrier wave of angular frequency  $\omega_c = 2\pi\nu_c$ :

$$E(t) = \sum_{k=-\infty}^{\infty} A(t - kT) e^{i\omega_c t}. \quad (1.3)$$

Here,  $T$  is the repetition period of the pulse train. Eq. 1.3 can be viewed as describing a laser

of angular frequency  $\omega_c$  with a time-varying amplitude. This temporal modulation leads to the distribution of the power across a spectrum whose width scales inversely with the temporal duration of  $A$ . Intuitively, the spectrum of the comb is the spectrum of the periodic baseband field envelope<sup>1</sup>  $\Sigma_k A(t - kT)$ , shifted in frequency by the multiplication with  $e^{i\omega_c t}$  so that it is centered around the optical carrier. More formally, we can calculate the frequency content of the comb by calculating

$$\mathcal{F}\{E\}(\omega) \sim \left( \sum_{k=-\infty}^{\infty} \mathcal{F}\{A(t - kT)\} \right) * \delta(\omega - \omega_c). \quad (1.4)$$

Here  $\mathcal{F}$  denotes Fourier transformation and  $*$  denotes convolution; this expression results from the Fourier transform's property that the transform of a product is the convolution of the transforms:  $\mathcal{F}(A \cdot B) = \mathcal{F}(A) * \mathcal{F}(B)$ . Now we use the Fourier transform's property that a temporal translation results in a linear spectral phase shift to obtain:

$$\mathcal{F}\{E\} \sim \left( \mathcal{F}\{A\} \times \sum_{k=-\infty}^{\infty} e^{-i\omega kT} \right) * \delta(\omega - \omega_c). \quad (1.5)$$

The quantity  $\sum_k e^{-i\omega kT}$  is the Fourier-series representation of the series of  $\delta$ -functions  $\sum_{\mu} \delta(\omega - 2\pi\mu/T)$  (the *Dirac comb*), so we have

$$\mathcal{F}\{E\}(\omega) \sim \left( \mathcal{F}\{A\} \times \sum_{\mu=-\infty}^{\infty} \delta(\omega - 2\pi\mu/T) \right) * \delta(\omega - \omega_c), \quad (1.6)$$

and performing the convolution leads to the replacement of  $\omega$  with  $\omega - \omega_c$ , leading to:

$$\mathcal{F}\{E\} \sim \sum_{\mu=-\infty}^{\infty} \delta(\omega - \omega_c - \mu\omega_r) \mathcal{F}\{A\}(\omega - \omega_c), \quad (1.7)$$

where  $\omega_{rep} = 2\pi f_{rep} = 2\pi/T$ . This expression indicates that the spectrum of the comb has frequency content at modes  $\nu_{\mu} = \nu_c + \mu f_{rep}$ , and that their amplitudes are determined by the spectrum of the baseband field envelope, shifted up to the optical carrier frequency  $\nu_c$ . This is the natural formulation in the case of a comb derived from a CW laser, but it obscures the carrier-envelope offset frequency in the difference between  $\nu_c$  and the nearest multiple of the repetition rate, as discussed above. In practice, if  $f_{rep}$  is known, then a measurement of  $f_0$  is equivalent to a measurement of the frequency of the input CW laser.

---

<sup>1</sup> which, as the spectrum of a periodic function, is already a comb.

### 1.1.2 Frequency stabilization of optical pulse trains

The scientific need for a method to measure optical frequencies motivated the development of optical frequency combs. While the measurement bandwidth of electronic frequency counters has improved since 1999, it remains limited to frequencies roughly *ten thousand* times lower than the frequency of, e.g., visible red light. Frequency combs present a method for measurement of the unknown frequency  $f_{opt}$  of an optical signal through heterodyne with a frequency comb—if  $f_{opt}$  falls within the bandwidth of the frequency comb, then the frequency of the heterodyne between the comb and the signal is guaranteed to be less than  $f_{rep}/2$ . If the frequencies of the comb are known, measurement of the heterodyne with the signal reveals its frequency  $f_{opt}$ , provided that the comb mode number and sign of the beat can be determined. This can be done via a wavelength measurement if sufficient precision is available, or by measuring the change  $\partial f_b / \partial f_{rep}$ , where  $f_b$  is the measured frequency of the beat.

The utility of the optical frequency comb lies in the fact that measurement of the two frequencies  $f_{rep}$  and  $f_0$  is sufficient to determine the optical frequencies of all of the modes of the comb, thereby enabling frequency measurement of optical signals. Measurement of the repetition rates of optical pulse trains was possible before the realization of optical frequency comb technology, as this can be done by simply impinging the pulse train on a photodetector. Some pulse trains generated in new platforms have repetition rates too high for direct measurement in this way, but this challenge can be addressed by e.g. spectrally interleaving a lower repetition-rate comb [18, 19]. In general, measurement of  $f_0$  presents the more difficult challenge. It was the confluence of several technological developments around the turn of the twenty-first century that allowed detection and measurement of this frequency, thereby enabling creation of fully-stabilized modelocked-laser pulse trains: optical frequency combs.

The carrier-envelope offset frequency of a pulse train is challenging to measure because it describes evolution of the optical carrier wave underneath the intensity envelope, and therefore cannot be measured through straightforward detection of the intensity of the pulse train. Presently,

the most straightforward way to measure  $f_0$  is  $f - 2f$  *self-referencing*. This can be performed only with a pulse train whose spectrum spans an octave—a factor of two in frequency. Given such an octave-spanning supercontinuum spectrum, a group of modes near mode number  $N$  is frequency-doubled in a medium with the  $\chi^{(2)}$  nonlinearity [20]. This frequency-doubled light is heterodyned with the native light in the supercontinuum with mode number near  $2N$ . The frequency of the resulting beat  $f_b$  is:

$$f_b = f_{doubled} - f_{native} \quad (1.8)$$

$$= 2(Nf_{rep} + f_0) - (2Nf_{rep} + f_0) \quad (1.9)$$

$$= f_0. \quad (1.10)$$

Such a scheme is implemented in an  $f - 2f$  *interferometer*, which is depicted in Fig. 1.2. Generating the necessary octave-spanning supercontinuum spectrum typically requires nonlinear spectral broadening of the pulse train after its initial generation except for in specific, carefully engineered cases (e.g. [19, 21]). Achieving the required degree of spectral broadening while preserving the coherence properties of the pulse train is a significant challenge—in the past this has typically required launching a train of high energy ( $\sim 1$  nJ), temporally short ( $\leq 100$  fs) pulses into the spectral-broadening stage. Recent developments in nonlinear fiber and waveguide technology have relaxed these requirements slightly (e.g. Ref. [22], also Chapter 7), but maintaining the coherence of the pulse train during spectral broadening remains an important consideration in designing optical frequency comb systems.

The application of  $f - 2f$  self-referencing for full frequency-comb stabilization is discussed in Chapters 7 and 8. Self-referencing of microresonator-based frequency combs is not a result presented explicitly in this thesis, but it is nonetheless a key step in the preparation of microcombs for applications and is a motivation for the investigations into microcomb nonlinear dynamics that are presented in Chapters 3-5.

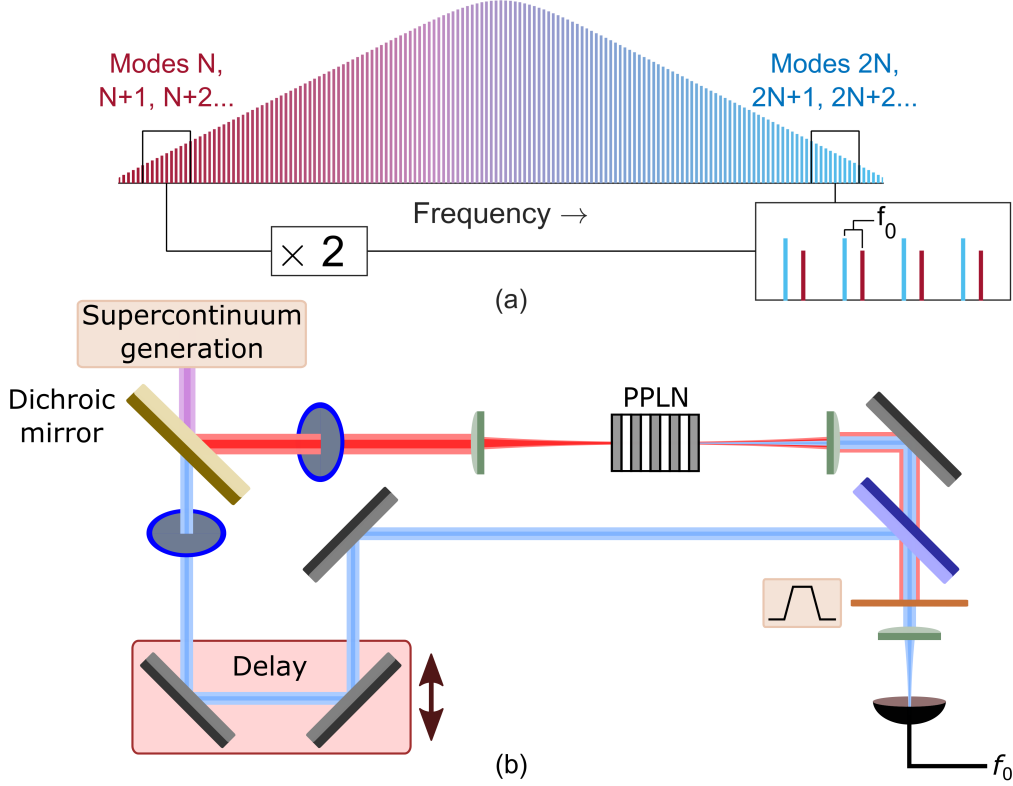


**Figure 1.2: Measurement of the carrier-envelope offset frequency  $f_0$  via  $f - 2f$  self-referencing.** (a) Frequency-domain depiction of  $f - 2f$  self-referencing: Light on the low frequency end of an octave-spanning supercontinuum is frequency-doubled, and then heterodyned with light on the high frequency end near twice its frequency, enabling measurement of the carrier-envelope offset frequency. (b) Schematic depiction of an  $f - 2f$  interferometer: After supercontinuum generation, a dichroic mirror splits the light by wavelength, and the low-frequency end of the supercontinuum (red) is sent through a nonlinear crystal for frequency-doubling. Here the crystal is periodically-poled lithium niobate (PPLN), where quasi-phased matching is employed for efficient doubling of the target modes [23]. The high-frequency end (blue) is sent through a delay stage, which can be adjusted to compensate for temporal walk-off between the spectral components (modes  $\sim N$  and modes  $\sim 2N$ ) required for self-referencing during the supercontinuum generation process. The two beams are then recombined by a beamsplitter and sent through a narrow optical band-pass filter centered around the doubled modes, which filters out light not necessary for  $f_0$  measurement to increase the signal-to-noise ratio of the detection. Photodetection of the band-passed beam then reveals  $f_0$ . Waveplates in each path are used to optimize the polarization of the long-wavelength light for frequency-doubling and to ensure co-polarization of the two beams on the detector.

## Chapter 2

### Introduction to microresonator-based frequency combs

This chapter introduces the basic physics of optical frequency-comb generation in Kerr-nonlinear microring resonators, with a particular emphasis on providing context for the results described in the subsequent chapters. This field emerged in 2007 with the first report of comb generation in silica microtoroids [24], and has evolved rapidly. There are facets to the field that are not discussed here; we note that a number of papers that review this topic have been published, each of which provides a unique perspective [25–28]. The combs generated in Kerr-nonlinear ring resonators, excluding those generated in definitively ‘macro’ fiber loops, have generally been called microcombs, despite the fact that some of the resonators used to generate them have dimensions on the scale of several millimeters. Microcombs are an attractive technology because of their high repetition rates and small footprints, especially relative to modelocked-laser-based combs, which make them promising candidates for inclusion in integrated photonics systems. Microcomb generation has been reported in a variety of platforms, including the aforementioned silica microtoroids, silica wedge [29, 30] and rod [31] resonators, crystalline magnesium-fluoride [32] and calcium-fluoride [33] resonators, and silicon-nitride waveguide resonators [34, 35], which have the advantage of being immediately amenable to photonic integration.

For simplicity, and following the terminology of the field, we will refer to broadband optical spectra generated through frequency conversion in Kerr-nonlinear microring resonators as ‘Kerr combs,’ even when the output is not strictly a coherent frequency comb. Finally, we note that although researchers have so far focused on Kerr-comb generation with the ring geometry, is also

possible to generate Kerr combs in a Kerr-nonlinear Fabry-Perot (FP) cavity, as has been demonstrated in several experiments [36, 37]. Theoretical investigations of Kerr-comb generation with the FP geometry are presented in Chapter 5.

## 2.1 Optical microring resonators

An optical microring resonator guides light for many round trips around a closed path in a dielectric medium by total internal reflection. The principle is the same as the guiding of light in an optical fiber, and indeed a ‘macroring’ resonator can be constructed from a loop of fiber, using a fiber-optic coupler with a small coupling ratio as an input/output port. Microring resonators can be constructed by looping an optical waveguide back on itself, in which case the resonator provides index contrast and light confinement over a full  $360^\circ$  of the modal cross-section. Alternatively, resonators can be realized with geometries that lack an inner radius dimension and therefore provide less spatial confinement. In this case they can host ‘whispering-gallery modes,’<sup>1</sup> so-called due to their similarity with the acoustic ‘whispering-gallery’ waves that permit a listener on one side of St. Paul’s cathedral (for example) to hear whispers uttered by a speaker on the other side of the cathedral. A schematic depiction of the basic components of a typical microring-resonator experiment is shown in Fig. 2.1. Optical microring resonators have a host of characteristics that make them useful for photonics applications in general and for nonlinear optics in particular; these include the ease with which they can be integrated and the ability to tailor the spectral distribution of guided modes through careful resonator design, as well as the ultra-high quality factors that have been demonstrated ( $\geq$  several hundred million). The resonator quality factor  $Q$  is defined as  $Q = \omega_0\tau_{ph} = \nu_0/\Delta\nu$ , where  $\omega_0 = 2\pi\nu_0$  is the optical angular frequency,  $\tau_{ph}$  is the photon lifetime, and  $\Delta\nu$  is the resonance linewidth. The  $Q$  can be interpreted literally as the optical phase that is traversed by the carrier wave during the photon lifetime and is a useful figure of merit for nonlinear optics.

---

<sup>1</sup> In some sources the terminology ‘whispering-gallery mode resonator’ has been applied more generally, but the analogy to the acoustic case seems most appropriate for resonators in which index contrast is not provided over a full  $360^\circ$  of the modal cross-section. Otherwise it is unclear what makes a WGM resonator different from a fiber loop, which in the limit of large radius obviously does not host whispering-gallery modes. This issue of terminology is discussed in Ref. [38].

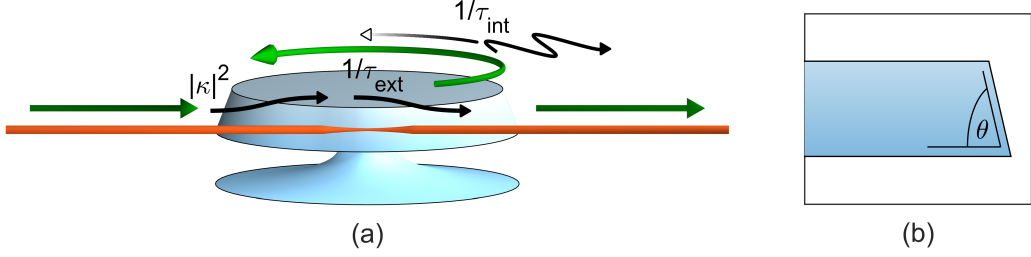


**Figure 2.1: Optical microdisk resonator.** (a) An optical microring resonator with the disk geometry as described in Ref. [29], operated in a through-coupled configuration. Light (green) is evanescently coupled into and out of the resonator through a tapered optical fiber, shown in orange, which contacts the resonator near the fiber’s point of smallest diameter. Light circulates in whispering-gallery modes concentric to the resonator’s circumference. The black labels indicate the coupling and loss rates discussed in Sec. 2.1.1:  $|\kappa|^2$  is the rate at which incoming photons are coupled into the resonator,  $1/\tau_{ext}$  is the rate at which circulating photons are coupling into the waveguide, and  $1/\tau_{int}$  is the intrinsic loss rate. Here contributions to  $1/\tau_{int}$  from absorption and radiative losses are depicted. (b) The wedge angle  $\theta$  can be adjusted to control the geometric dispersion of the propagating whispering-gallery modes as described in Ref. [39], as  $\theta$  dictates, for example, the extent to which larger (longer-wavelength) modes are confined further from the circumference of the wedge.

A microring resonator supports propagating guided modes of electromagnetic radiation with (vacuum) wavelengths that evenly divide the optical round-trip path length:  $\lambda_m = n_{eff}(\lambda_m)L/m$ , with associated resonance frequencies  $\nu_m = c/\lambda_m = mc/n_{eff}(\nu_m)L$ . This leads to constructive interference from round trip to round trip. Here  $m$  is the azimuthal mode number and the quantity  $Ln_{eff}(\lambda_m)$  is the optical round-trip path length of the mode, where  $n_{eff}(\lambda_m)$  defines an effective index of refraction related to the mode’s propagation constant  $k(\omega)$  via  $k(\omega) = n_{eff}(\omega)\omega/c$  (see e.g. Refs. [40, 41]; we use the symbol  $k$  here and reserve the standard symbol  $\beta$  for another quantity). The free-spectral range  $f_{FSR}$  of a resonator is the *local* frequency spacing between modes, calculated via:

$$f_{FSR} \approx \frac{\nu_{m+1} - \nu_{m-1}}{2} \quad (2.1)$$

$$= \frac{\partial \nu_m}{\partial m} \quad (2.2)$$

$$= \frac{c}{n_{eff}(\nu)L} - \frac{mc}{n_{eff}^2(\nu)L} \frac{\partial n_{eff}}{\partial \nu} \frac{\partial \nu}{\partial m}, \quad (2.3)$$

so that, rearranging, we obtain:

$$f_{FSR} = \frac{c/L}{\left(n_{eff} + \nu \frac{\partial n_{eff}}{\partial \nu}\right)} = \frac{c}{n_g L} = 1/T_{RT}, \quad (2.4)$$

where  $n_g = n_{eff} + \nu \frac{\partial n_{eff}}{\partial \nu}$  is the group velocity of the mode and  $T_{RT}$  is the mode's round-trip time. The effective index  $n_{eff}$  is frequency dependent due to both intrinsic material dispersion and geometric dispersion, where the latter results for example from different sampling of material properties for different wavelength-dependent mode areas. A frequency-dependent  $n_{eff}$  leads to a non-uniform spacing in the cavity modes in frequency despite the linearity of  $\nu_m$  in  $m$ ; equivalently this results in a frequency dependence of  $n_g$  and  $f_{FSR}$ .

Depending on the design, microring resonators can support many transverse mode profiles, or just one. The former is typical of whispering-gallery-mode resonators that lack an inner radius, such as the wedge resonator shown in Fig. 2.1 or free-standing silica microrod resonators [31]; the latter can be readily achieved using chip-integrated single-mode photonic waveguides. For a given resonator geometry, to calculate the frequency-dependent effective index  $n_{eff}(\nu)$ , thereby enabling calculation of the resonance frequencies and wavelengths, one must solve Maxwell's equations for the resonator geometry. Except in special cases of high symmetry (e.g. a dielectric sphere [42]), this is typically done numerically using finite-element modeling tools like COMSOL. The modes of an optical resonator, both within a mode family defined by a transverse mode profile (such that they differ only by azimuthal mode number  $m$ ) and between mode families, must be orthogonal [43], with no linear coupling between them.

### 2.1.1 Resonant enhancement in a microring resonator

The lifetime  $\tau_{ph}$  of circulating photons in a resonator is fundamental to its fitness for applications. Generally, two processes lead to the loss of circulating photons: intrinsic dissipation that occurs at a rate  $1/\tau_{int}$  and out-coupling to an external waveguide that occurs at a rate  $1/\tau_{ext}$ , leading to a total loss rate of  $\tau_{ph}^{-1} = \tau_{ext}^{-1} + \tau_{int}^{-1}$ . To understand the quantitative role of these parameters, we consider a cavity mode of frequency  $\omega_0$  and described by instantaneous amplitude  $a(t)$  (normalized

such that  $|a|^2 = N$ , the number of circulating photons) driven by a pump field with frequency  $\omega_p$  and rotating amplitude  $s \propto \exp(i\omega_p t)$  (normalized such that  $|s|^2 = S$ , the rate at which photons in the coupling waveguide pass the coupling port) that is in-coupled with strength  $\kappa$ . The equation of motion for such a system is [43]:

$$\frac{da}{dt} = i\omega_0 a - \left( \frac{1}{2\tau_{int}} + \frac{1}{2\tau_{ext}} \right) a + \kappa s, \quad (2.5)$$

and the rates that determine the evolution of  $a$  are shown schematically in Fig. 2.1. We can immediately solve this equation by assuming that  $a \propto \exp(i\omega_p t)$ , and we obtain:

$$a = \frac{\kappa s}{\left( \frac{1}{2\tau_{int}} + \frac{1}{2\tau_{ext}} \right) + i(\omega_p - \omega_0)}. \quad (2.6)$$

The coupling strength  $\kappa$  into the waveguide and the out-coupling rate  $1/\tau_{ext}$  are related by  $|\kappa|^2 = 1/\tau_{ext}$ ; one can arrive at this conclusion by considering the special case  $1/\tau_{int} = 0$  and exploiting the time-reversal symmetry of the system under this condition [43]. By squaring Eq. 2.6 and inserting this relationship between  $\kappa$  and  $\tau_{ext}$ , we find:

$$N = \frac{\Delta\omega_{ext}S}{\Delta\omega^2/4 + (\omega_p - \omega_0)^2}, \quad (2.7)$$

where we have defined the rates  $\Delta\omega_{ext} = 1/\tau_{ext}$ ,  $\Delta\omega_{int} = 1/\tau_{int}$ , and  $\Delta\omega = \Delta\omega_{ext} + \Delta\omega_{int}$ . Two important observations can be drawn from Eq. 2.7: First, the cavity response is Lorentzian with a full-width at half-maximum (FWHM) linewidth that is related to the photon lifetime via  $\tau_{ph} = 1/\Delta\omega$ , and second, on resonance the number of circulating photons is related to the input rate by the factor  $\Delta\omega_{ext}/\Delta\omega^2 \ll 1$ . This factor is not yet the resonant enhancement, which we now calculate by considering the circulating power  $P = N\hbar\omega_p/T_{RT}$  on resonance (when  $\omega_p = \omega_0$ ):

$$P = \frac{4\Delta\omega_{ext}P_{in}/T_{RT}}{\Delta\omega^2} \quad (2.8)$$

$$= \frac{2}{\pi} P_{in} \eta \mathcal{F}, \quad (2.9)$$

where  $\mathcal{F} = 2\pi\tau_{ph}/T_{RT} = f_{FSR}/\Delta\nu$  is the resonator finesse,  $\eta = \Delta\omega_{ext}/\Delta\omega$  is the coupling ratio, typically of order  $\sim \frac{1}{2}$ , and  $P_{in} = \hbar\omega_p S$  is the power in the waveguide. Thus, the circulating power is approximately a factor  $\mathcal{F}$  greater than the input power. The combination of this resonant

enhancement and a small cavity mode volume enables very large circulating optical intensities in high finesse resonators, which is important for the application of microresonators in nonlinear optics.

### 2.1.2 Thermal effects in microresonators

In a typical microresonator frequency-comb experiment, a frequency-tunable pump laser is coupled evanescently into and out of the resonator using a tapered optical fiber [44, 45] (for e.g. free-standing silica disc resonators) or a bus waveguide (for chip-integrated resonators, e.g. in silicon nitride rings). When spatial overlap and phase-matching ( $n_{eff,res} \sim n_{eff,coupler}$  [46]) between the evanescent mode of the coupler and a whispering-gallery mode of the resonator is achieved, with the frequency of the pump laser close to the resonant frequency of that mode, light will build up in the resonator and the transmission of the pump laser past the resonator will decrease.

In any experiment in which a significant amount of pump light is coupled into a resonator, one immediately observes that the cavity resonance lineshape in a scan of the pump-laser frequency is not Lorentzian as expected from Eq. 2.7; plots of measured resonance lineshapes are shown in Fig. 2.2a. This is because the resonator heats as it absorbs circulating optical power. Associated with this change in temperature are changes in the mode volume and the refractive index, described respectively by the coefficient of thermal expansion  $\partial V/\partial T$  and the thermo-optic coefficient  $\partial n/\partial T$ . For typical microresonator materials the thermo-optic effect dominates, and  $\partial n/\partial T > 0$  leads to a decrease in the resonance frequency with increased circulating power in thermal steady state. Thus, for an adiabatic scan across the cavity resonance with decreasing laser frequency, as the laser approaches the resonance in frequency space and power is coupled into the resonator, the resonance frequency will begin to shift with the laser frequency, and a sawtooth-shaped resonance emerges.

The thermal dynamics related to  $\partial n/\partial T$  and  $\partial V/\partial T$  dictate the signs and values of detuning  $\omega_0 - \omega_p$  that are readily accessible in experiment. Specifically, a calculation of the thermal dynamics of the system composed of the pump laser and the resonator reveals that when the pump laser with frequency  $\omega_p$  is near the ‘cold-cavity’ resonance frequency of a given cavity mode  $\omega_{0,cold}$  the resonance has three possible thermally-shifted resonance frequencies  $\omega_{0,shifted}$  at which thermal steady state

is achieved [47]. Generally, these points are:

- (1)  $\omega_p > \omega_{0,shifted}$ , blue detuning<sup>2</sup> with significant coupled power and thermal shift
- (2)  $\omega_p < \omega_{0,shifted}$ , red detuning with significant coupled power and thermal shift
- (3)  $\omega_p \ll \omega_0$ , red detuning with insignificant coupled power and insignificant thermal shift

These points are depicted schematically in Fig. 2.2b. Steady-state point (1) is experimentally important, because in the presence of pump-laser frequency and power fluctuations it leads to so-called thermal ‘self-locking.’ Specifically for steady-state point (1), this can be seen as follows:

- If the pump-laser power increases, the cavity heats, the resonance frequency decreases, the detuning increases, and the change in coupled power is minimized.
- If the pump-laser power decreases, the cavity cools, the resonance frequency increases, the detuning decreases, and the change in coupled power is minimized.
- If the pump-laser frequency increases, the cavity cools, the resonance frequency increases, and the change in coupled power is minimized.
- If the pump-laser frequency decreases, the cavity heats, the resonance frequency decreases, and the change in coupled power is minimized.

This is in contrast with steady-state point (2), where each of the four pump-laser fluctuations considered above generates a positive feedback loop, with the result that any fluctuation will push the system towards point (1) or point (3) and so point (2) is unstable. This preference of the system to occupy point (1) or point (3) over a range of pump-laser detuning is referred to as thermal bistability. As a result of this bistability, point (2) (i.e. red detuning with significant coupled power) cannot be observed in an experimental scan of the pump laser across the resonance in either direction. As explained above, when the pump-laser frequency is decreased the resonance takes on a broad sawtooth shape, while in an increasing-frequency scan the resonance takes on a narrow

---

<sup>2</sup> Here we use the convention that the ‘color’ of the detuning specifies the position of the laser with respect to the resonance—‘blue’ detuning means that the laser is more blue, or higher in frequency.

pseudo-Lorentzian profile whose exact shape depends on the scan parameters relative to the thermal timescale. A second consequence is that, in the absence of other stabilizing effects, operation at red detuning with significant coupled power in a microresonator experiment requires special efforts to mitigate the effects of thermal instability.

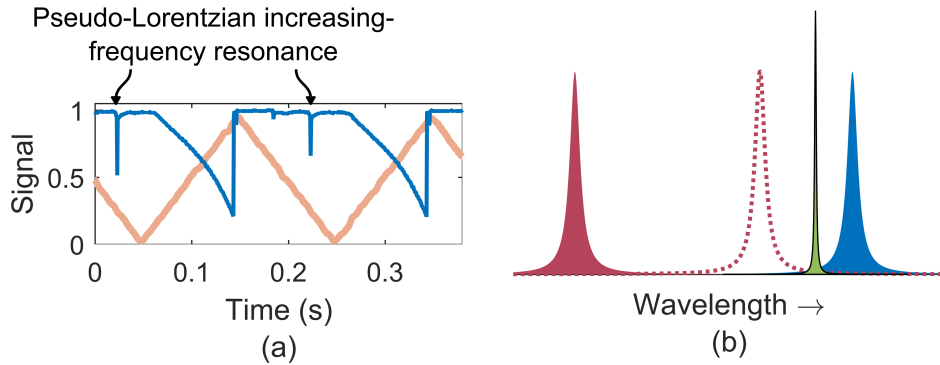


**Figure 2.2: Thermal bistability in microresonators.** (a) Measurement of power transmitted past the microresonator (blue) in an experiment using a  $\sim 16.5$  GHz-FSR microdisk resonator and a tapered fiber. The wavelength of the pump laser is controlled by a piezo-electric crystal that adjusts the length of the laser cavity. Here, larger control signal (orange) corresponds to longer laser wavelength. As the laser wavelength is increased, the resonator heats and a sawtooth-shaped resonance is observed. Ultimately the resonator reaches a maximum temperature that depends on the pump power, and the laser then becomes red-detuned as the wavelength continues to increase; then the resonator rapidly cools and the resonance is lost. Shortly thereafter, the direction of the scan is reversed. As the resonator wavelength is decreased, the system will ‘flip’ from steady-state point (3) to steady-state point (1), leading to observation of a narrow pseudo-Lorentzian resonance, with the exact shape depending on the thermal and scanning timescales. (b) Depiction of the three steady-state points for the laser detuning. For fixed laser wavelength (green), stable steady-state points exist with relatively small blue detuning and significant coupled power (solid blue), and relatively large red detuning and little coupled power (solid red). An unstable steady-state point also exists with red detuning and significant coupled power (dashed red). Note in this terminology that the color of the detuning (red or blue) refers to the position of the laser relative to the position of the resonance in wavelength space.

## 2.2 Microring resonator Kerr frequency combs

The high circulating optical intensities accessible in resonators with long photon lifetimes find immediate application in the use of microresonators for nonlinear optics. The experiments described in this thesis are conducted in silica microresonators. Silica falls into a broader class of materials that exhibit both centro-symmetry, which dictates that the second-order nonlinear susceptibility

$\chi^{(2)}$  must vanish, and a significant third-order susceptibility  $\chi^{(3)}$ . The  $n^{\text{th}}$ -order susceptibility is a term in the Taylor expansion describing the response of the medium's polarization to an external electric field [20]:  $P = P_0 + \epsilon_0 \chi^{(1)} E + \epsilon_0 \chi^{(2)} E^2 + \epsilon_0 \chi^{(3)} E^3 + \dots$ . The effect of  $\chi^{(3)}$  can be described in a straightforward way as a dependence of the refractive index on the local intensity [40],

$$n = n_0 + n_2 I \quad (2.10)$$

where  $n_2 = \frac{3\chi^{(3)}}{4n_0^2 \epsilon_0 c}$  is called the Kerr index [40, 48]. The intensity-dependence of the refractive index resulting from the third-order susceptibility  $\chi^{(3)}$  is referred to as the optical Kerr effect and enables the self-phase modulation (SPM), cross-phase modulation (XPM), and four-wave mixing (FWM) nonlinear processes [20]. Four-wave mixing is a general frequency-domain description of an energy-conserving interaction between fields of up to four different frequencies, as depicted in Figs. 2.3a and b; self-phase modulation and cross-phase modulation can be thought of as time-domain descriptions of particular cases of FWM. In SPM and XPM the nonlinear interaction leads to intensity-dependent phase shifts of the field. If the intensity varies in time, for example in the case of an optical pulse, then the resulting time-varying nonlinear phase shift applies a chirp to the pulse. This can lead to modification of the pulse's spectrum, including the generation of new frequency components.<sup>3</sup>

For FWM to efficiently lead to the generation of new frequencies in some medium or waveguide it must be effectively phasematched, meaning that the quantity [49]

$$\Delta k = k(\omega_1) + k(\omega_2) - k(\omega') - k(\omega''), \quad (2.11)$$

where  $k(\omega) = n_{\text{eff}}(\omega)\omega/c$  is the propagation constant, should be made as small as possible; in the above the four frequencies correspond to those depicted in Figs. 2.3a and b. In a ring resonator, FWM is intrinsically phasematched in interactions between fields propagating in modes with azimuthal mode numbers  $m_1$ ,  $m_2$ ,  $m'$ , and  $m''$  such that  $m_1 + m_2 = m' + m''$  [50]. Reports of few-mode parametric oscillation in microresonators based on FWM preceded the first observations of Kerr-comb generation [50–52].

---

<sup>3</sup> SPM doesn't *always* lead to the generation of new frequency components. For example, solitons can propagate without becoming chirped through a balance between SPM and dispersion, and SPM can even lead to narrowing of the bandwidth of a pulse when e.g. the chirp generated by SPM has sign opposite to an existing chirp on the pulse.

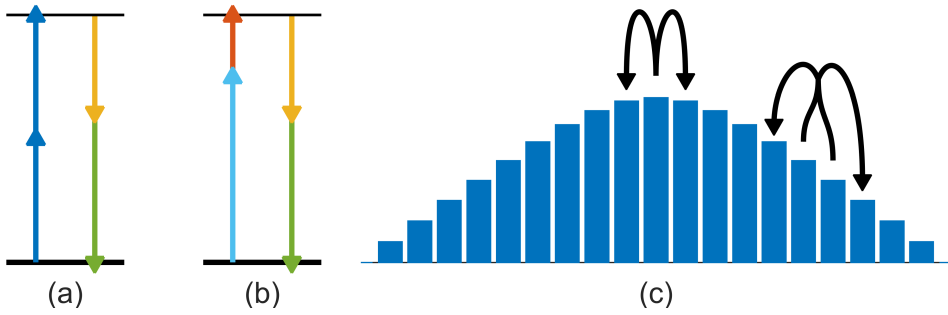


**Figure 2.3: An illustration of four-wave mixing and frequency-comb generation.** (a) Degenerate four-wave mixing, in which two fields of the same frequency  $\omega_1$  (blue) mix and generate fields at two new frequencies  $\omega'$  and  $\omega''$  (yellow and green). The schematic indicates the energy-conversation requirements of the process, which can be written as  $2\omega_1 = \omega' + \omega''$ . (b) Non-degenerate four-wave mixing, in which two fields of different frequencies  $\omega_2$  and  $\omega_3$  (light blue and orange) mix to generate fields at frequencies  $\omega'$  and  $\omega''$  (yellow and green). Energy conservation is now expressed as  $\omega_2 + \omega_3 = \omega' + \omega''$ . (c) Schematic depiction of one degenerate FWM step and one non-degenerate FWM step in a cascaded four-wave mixing process that generates a frequency comb. Figure after Ref. [25].

In 2007, the remarkable observation by Del’Haye et al. of *cascaded four-wave mixing* (CFWM, shown in Fig. 2.3c) in anomalously-dispersive ( $k'' = \frac{\partial^2}{\partial \omega^2} \frac{n_{eff}(\omega)\omega}{c} < 0$ ) toroidal silica microcavities on silicon chips brought about a new era for frequency comb research. They observed the generation many co-circulating optical fields that were uniformly spaced by  $f_{rep}$  ranging from 375 GHz to  $\sim$ 750 GHz (depending on the platform) [24]. This result showed that the non-uniform distribution of cavity resonance frequencies due to dispersion could be overcome to generate an output with many equidistant frequency modes. A second important development occurred in 2012, when Herr et al. reported the generation of frequency combs corresponding in the time domain to single circulating optical ‘soliton’ pulses [53, 54]. This observation followed the observation of solitons in formally-equivalent passive fiber-ring resonators in 2010 [55]. Due to unique properties that make them particularly well-suited for applications, as discussed in Sec. 2.3.3, the generation and manipulation of soliton combs has become a significant priority in microcomb research.

### 2.2.1 A model for Kerr-comb nonlinear optics: The Lugiato-Lefever equation

Kerr-comb generation can be motivated and partially understood through the CFWM picture [56], but the phase and amplitude degrees of freedom for each comb line mean that CFWM gives

rise to a rich space of comb phenomena—it is now known that Kerr combs can exhibit several fundamentally distinct outputs. A useful model for understanding this rich space is the Lugiato-Lefever equation (LLE), which was shown to describe microcomb dynamics by Chembo and Menyuk [57] through Fourier-transformation of a set of coupled-mode equations describing CFWM and by Coen, Randle, Sylvestre, and Erkintalo [58] through time-averaging of a more formally-accurate model for a low-loss resonator (as first performed by Haelterman, Trillo, and Wabnitz [59]). The LLE is a nonlinear partial-differential equation that describes evolution of the normalized cavity field envelope  $\psi$  over a slow time  $\tau = t/2\tau_{ph}$  in a frame parametrized by the ring's azimuthal angle  $\theta$  (running from  $-\pi$  to  $\pi$ ) co-moving at the group velocity.<sup>4</sup> A derivation of the LLE is provided in Appendix A. The equation in the notation of Chembo and Menyuk, as it will be used throughout this thesis, reads:

$$\frac{\partial \psi}{\partial \tau} = -(1 + i\alpha)\psi + i|\psi|^2\psi - i\frac{\beta_2}{2}\frac{\partial^2 \psi}{\partial \theta^2} + F. \quad (2.12)$$

This equation describes  $\psi$  over the domain  $-\pi \leq \theta \leq +\pi$  with periodic boundary conditions  $\psi(-\pi, \tau) = \psi(\pi, \tau)$ . Here  $F$  is the field strength of the pump laser, with  $F$  and  $\psi$  both normalized so that they take the value 1 at the absolute threshold for parametric oscillation:  $F = \sqrt{\frac{8g_0\Delta\omega_{ext}}{\Delta\omega^3}\frac{P_{in}}{\hbar\omega_p}}$ ,  $|\psi|^2 = \frac{2g_0T_{RT}}{\hbar\omega_p\Delta\omega}P_{circ}(\theta, \tau)$ , so that  $|\psi(\theta, \tau)|^2$  is the instantaneous normalized power at the co-moving azimuthal angle  $\theta$ . Here  $g_0 = n_2c\hbar\omega_p^2/n_g^2V_0$  is a parameter describing the four-wave mixing gain,  $\Delta\omega_{ext}$  is the rate of coupling at the input/output port,  $\Delta\omega = 1/\tau_{ph}$  is the FWHM resonance linewidth,  $P_{in}$  is the pump-laser power,  $P_{circ}(\theta, \tau)$  is the local circulating power in the cavity,  $\hbar$  is Planck's constant, and  $\omega_p$  is the pump-laser frequency. The parameters  $n_2$ ,  $n_g$ , and  $V_0$  describe the nonlinear (Kerr) index (see Eqn. 2.10), the group index of the mode, and the effective nonlinear mode volume at the pump frequency;  $L$  is the physical round-trip length of the ring cavity.

The parameters  $\alpha$  and  $\beta_2$  describe the frequency detuning of the pump laser and second-order dispersion of the resonator mode family into which the pump laser is coupled, both normalized to

---

<sup>4</sup> The co-moving azimuthal angle  $\theta$  is analogous to the ‘fast time’ variable that appears in, for example, the nonlinear Schrodinger equation for fiber-optic pulse propagation [40], and it can be transformed explicitly to a fast time  $t$  via  $t = T_{RT} \times \frac{\theta}{2\pi}$ .

half the cavity linewidth:

$$\alpha = -\frac{2(\omega_p - \omega_0)}{\Delta\omega}, \quad (2.13)$$

$$\beta_2 = -\frac{2D_2}{\Delta\omega}; \quad (2.14)$$

here  $D_2 = \left. \frac{\partial^2 \omega_\mu}{\partial \mu^2} \right|_{\mu=0}$  is the second-order modal dispersion parameter, where  $\mu$  is the pump-referenced mode number of Eq. 1.2. The parameters  $D_1 = \left. \frac{\partial \omega_\mu}{\partial \mu} \right|_{\mu=0} = 2\pi f_{FSR}$  and  $D_2$  are related to the derivatives of the propagation constant  $k(\omega) = \frac{n_{eff}(\omega)\omega}{c}$  via  $D_1 = 2\pi/Lk'$  and  $D_2 = -D_1^2 \frac{k''}{k'}$ . It is useful to note that  $k' = 1/v_g$ , where  $v_g$  is the group velocity in the medium, and  $k''$  is often referred to as the GVD parameter and denoted by  $\beta_2$ , which here is reserved for the dispersion parameter in the LLE. Expressions for higher-order modal dispersion parameters  $D_n$  in terms of the expansion of the propagation constant can be obtained by evaluating the equation  $D_{n>1} = (D_1 \frac{\partial}{\partial \omega})^{n-1} D_1$ , and may be incorporated into the LLE up to desired order  $N$  through the replacement:

$$-i \frac{\beta_2}{2} \frac{\partial^2 \psi}{\partial \theta^2} \rightarrow + \sum_{n=1}^N i^{n+1} \frac{\beta_n}{n!} \frac{\partial^n \psi}{\partial \theta^n}, \quad (2.15)$$

where  $\beta_n = -2D_n/\Delta\omega$ . This thesis describes frequency-comb generation in anomalously-dispersive resonators, and so  $\beta_2 < 0$  throughout.

The formulation of the LLE in terms of dimensionless normalized parameters helps to elucidate the fundamental properties of the system and facilitates comparison of results obtained in platforms with widely different experimental conditions. The LLE relates the time-evolution of the intracavity field (normalized to its threshold value for cascaded four-wave mixing) to the power of the pump laser (normalized to its value at the threshold for cascaded four-wave mixing), the pump-laser detuning (normalized to half the cavity linewidth), and the cavity second-order dispersion quantified by the change in the FSR per mode (normalized to half the cavity linewidth). One example of the utility of this formulation is that it makes apparent the significance of the cavity linewidth in determining the output comb, and underscores the fact that optimization of the dispersion, for example, without paying heed to the effect of this optimization on the cavity linewidth, may not yield the desired results. This adds an additional layer of complexity to dispersion engineering relative to straight waveguides.

The LLE is, of course, a simplified description of the dynamics occurring in the microresonator. It abstracts the nonlinear dynamics and generally successfully describes the various outputs that can be generated in a microresonator frequency comb experiment. The LLE is a good description of these nonlinear dynamics when the resonator photon lifetime, mode overlap, and nonlinear index  $n_2$  are roughly constant over the bandwidth of the generated comb, and when the dominant contribution to nonlinear dynamics is simply the self-phase modulation term  $i|\psi|^2\psi$  arising from the Kerr nonlinearity. The LLE neglects the polarization of the electric field ( $\psi$  is a scalar), as well as thermal effects and the Raman scattering and self-steepening nonlinearities, although in principle each of these can be included [40, 54, 60, 61]. It is also worth emphasizing that the LLE can be derived from a more formally-accurate Ikeda map (as explained by Coen et al. [58]), in which the effect of localized input- and output-coupling is included in the model. This derivation is accomplished by ‘delocalizing’ the pump field and the output-coupling over the round trip, including only their averaged effects. This is an approximation that is valid in the limit of high finesse due to the fact that the cavity field cannot change on the timescale of a single round trip, but as a result the LLE necessarily neglects all dynamics that might have some periodicity at the round-trip time; the fundamental timescale of LLE dynamics is the photon lifetime.

### 2.3 Description of Kerr-comb outputs using the Lugiato-Lefever equation

The LLE provides a useful framework for the prediction and interpretation of experimental results. Basically, it predicts the existence of two fundamentally distinct types of Kerr-combs: extended temporal patterns and localized soliton pulses. These predictions are born out by experiments, the interpretation of which is facilitated by insight gained from the LLE. In the remainder of this chapter I briefly present some analytical results that can be obtained from the LLE about the behavior of the continuous-wave (CW) field that exists in the resonator in the absence of Kerr-comb formation, and then discuss these two types of comb outputs. This discussion provides context for the results presented in the next two chapters. Fig. 2.4 summarizes the results that will be presented

in the remainder of this chapter, and in particular shows the values of the parameters  $\alpha$  and  $F^2$  at which solitons and extended patterns can be obtained.

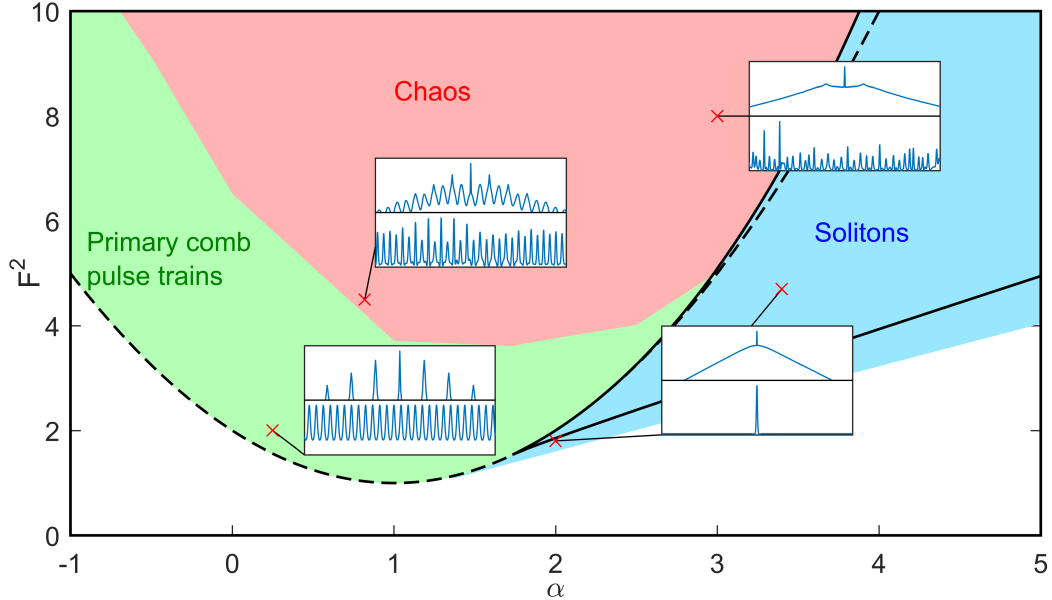


**Figure 2.4: Solution space for the Lugiato-Lefever equation.** Depiction of the various behaviors exhibited by  $\psi$  as a function of its position in the  $\alpha - F^2$  plane; this predicts the type of Kerr-comb output as a function of the pump-laser detuning and power, the parameters that are most readily adjusted in experiment. Curves plotted in black are obtained through analytical investigation of the LLE; these include the threshold curve for parametric oscillation (dashed black, Eq. 2.22) and the lines obtained via  $\rho(\alpha, F^2) = \rho_{\pm}(\alpha)$  (solid black, Eq. 2.19), which define the region where the LLE exhibits multiple flat solutions (i.e. solutions such that  $\partial\psi/\partial\theta = 0$ , Eq. 2.16). Extended patterns arise above the threshold curve through modulation instability. Solitons exist outside of the threshold curve at higher red detuning, up to an approximate maximum  $\alpha_{max} = \pi^2 F^2/8$ . The lines bounding the existence of chaos are not known precisely, and in fact chaos can be observed in simulation outside of the threshold curve at values  $\alpha > \alpha_{thresh,+}$  (Eq. 2.23). Insets show representative simulation results for the various types of comb outputs in the frequency (top) and time (bottom) domains. Fig. after Ref. [62].

### 2.3.1 Analytical investigation of the resonator's CW response

Some insight into comb dynamics can be obtained via analytical investigations of the LLE, Eq. 2.12. This section largely follows the analysis of Ref. [62], with similar analysis having been performed elsewhere, for example in Refs. [58] and [63]. When the derivative term  $\partial^2\psi/\partial\theta^2$  in the LLE is non-zero,  $\psi$  is necessarily broadband, and a Kerr comb has been formed. There are no known exact analytical solutions to the LLE to describe Kerr-comb outputs, which must instead be numerically simulated (see Appendix B). However, flat solutions  $\psi_{CW}$  to the LLE may be calculated

by setting all derivatives to zero—when these solutions can be realized physically (discussed below), they describe a CW field in the resonator. Upon setting the derivatives in the LLE to zero, one finds:

$$F = (1 + i\alpha)\psi_{CW} - i|\psi_{CW}|^2\psi_{CW}. \quad (2.16)$$

The circulating intensity  $\rho = |\psi_{CW}|^2$  is obtained by taking the modulus-square of Eq. 2.16 to obtain:

$$F^2 = (1 + (\alpha - \rho)^2) \rho, \quad (2.17)$$

$$= \rho^3 - 2\alpha\rho^2 + (\alpha^2 + 1)\rho, \quad (2.18)$$

whereupon this equation can be numerically solved for  $\rho$ . As a third-order polynomial in  $\rho$  this equation has three solutions, one or three of which may be real; the complex solutions are unphysical. The function  $F^2(\alpha, \rho)$  defined by this equation uniquely determines  $F^2$  given  $\alpha$  and  $\rho$ . We now consider plotting a graph of  $F^2(\alpha, \rho)$  with  $\alpha$  held constant; examples are given in Fig. 2.5. By noting that  $F^2(\alpha, \rho = 0) = 0$  and  $\partial F^2 / \partial \rho|_{\rho=0} > 0$ , we can conclude that a graph of  $F^2(\alpha, \rho)$  will cross the same value  $F^2$  three times if  $F^2$  is between the extremal values  $F_{\pm}^2(\alpha)$  at which  $\partial F^2 / \partial \rho = 0$ . This means that three real solutions  $\rho_1$ ,  $\rho_2$ , and  $\rho_3$  for the inverted function  $\rho(\alpha, F^2)$  exist for each value of  $F^2$  between  $F_-^2(\alpha)$  and  $F_+^2(\alpha)$ . The values  $F_{\pm}^2(\alpha)$  bounding this region of degeneracy in  $\rho$  are found by inserting the values  $\rho_{\pm}$  at which  $\partial F^2 / \partial \rho = 0$  into Eq. 2.17. That is,  $F_{\pm}^2(\alpha) = F^2(\alpha, \rho_{\mp})$ , where:

$$\rho_{\pm} = \frac{2\alpha \pm \sqrt{\alpha^2 - 3}}{3}. \quad (2.19)$$

For pump powers outside of the interval  $[F_-^2(\alpha), F_+^2(\alpha)]$ , which varies with  $\alpha$ , there is only one real solution  $\rho$ ; within this interval there are three. This is illustrated in Fig. 2.5. The smallest value of  $F^2$  at which the stationary curve  $\rho$  becomes multivalued is found to be  $F^2 = 8\sqrt{3}/9$  by solving for  $\rho_- = \rho_+$  and inserting the corresponding values into Eq. 2.17.

Physically, the coexistence of multiple flat solutions  $\rho$  at a given point  $(\alpha, F^2)$  corresponds to a ‘tilting’ of the Lorentzian transmission profile of the cavity and leads to bistability, even before taking into account thermal effects. This is illustrated in Fig. 2.5. For flat solutions  $\rho$ , an effective Kerr-shifted detuning can be defined as  $\alpha_{eff} = \alpha - \rho$ . The effective detuning simply incorporates

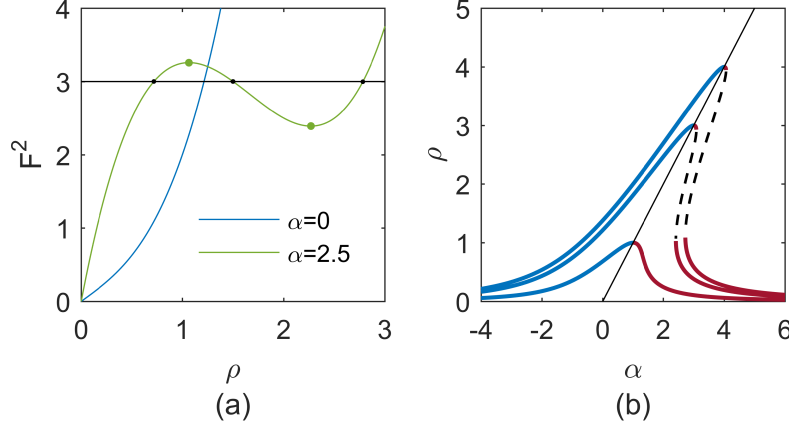


**Figure 2.5: Investigation of the circulating CW power in a Kerr resonator.** (a) Plots of  $F^2$  as a function of  $\rho$  for  $\alpha = 0$  (blue) and  $\alpha = 2.5$  (green), according to Eq. 2.17. When real values of  $\rho$  exist that extremize  $F^2$  according to this equation, multiple real solutions for the circulating power  $\rho$  exist between these extremal values of  $F^2$ . For  $\alpha = 2.5$  we indicate the extremal values of  $F^2$  as green dots. For an example value  $F^2 = 3$ , the corresponding allowed values  $\rho_1$ ,  $\rho_2$ , and  $\rho_3$  are the intersections of the green curve and the black line (black dots); such a line would have three intersections with the green curve for any value of  $F^2$  between  $F_\alpha^2(\rho_-)$  and  $F_\alpha^2(\rho_+)$ . (b) Kerr-tilted resonances curves  $\rho(\alpha)$  for  $F^2 = 1$  (smallest),  $F^2 = 3$ , and  $F^2 = 4$  (largest). The line  $\rho = \alpha = F^2$  (solid black) marks the highest circulating power for a given input power  $F^2$  and separates the effectively blue-detuned and effectively red-detuned branches. When  $F^2 > 8\sqrt{3}/9$  (obtained by solving for  $\rho_+ = \rho_-$ , Eq. 2.19), the resonance becomes tilted steeply enough that an unstable middle branch (dashed black) exists.

the Kerr nonlinearity into the round-trip phase shift that describes the constructive or destructive interference of the circulating field with the pump at the coupling port. By noting that  $\alpha = F^2 = \rho$  solves Eq. 2.17, we can conclude that the position of the effective Kerr-shifted resonance is on the line  $\alpha = F^2$ , where  $\alpha_{eff} = 0$ .

Once the circulating intensity  $\rho$  is known, the corresponding flat solution  $\psi_{CW}$  can be determined from Eq. 2.16 by inserting the known value of  $\rho$  and solving for  $\psi_{CW}$ , with the result:

$$\psi_{CW} = \frac{F}{1 + i(\alpha - \rho)}. \quad (2.20)$$

This expression reveals that the flat solution acquires a phase  $\phi_s = \tan^{-1}(\rho - \alpha)$  relative to the pump.

If the flat solution(s) at a point  $(\alpha, F^2)$  is (are) unstable, a Kerr comb will form spontaneously. Stability analysis of the flat solutions can be performed, and for the case of second-order dispersion

alone the results are [62]:

- In the region of multi-stability, if the flat solutions are ordered with increasing magnitude as  $\rho_1$ ,  $\rho_2$ , and  $\rho_3$ , the middle solution  $\rho_2$  is always unstable.
- When  $\alpha < 2$ , a flat solution  $\rho$  that is not the middle solution is stable if  $\rho < 1$ ; otherwise it is unstable. When the flat solution is unstable, the mode that experiences the greatest instability has mode number given by:

$$\mu_{max} = \sqrt{\frac{2}{\beta_2}(\alpha - 2\rho)} \quad (2.21)$$

Therefore, the pump-laser threshold curve for Kerr-comb generation can be determined in the region  $\alpha < 2$  of the  $\alpha - F^2$  plane by setting  $\rho = 1$  in Eq. 2.16:

$$F_{thresh}^2 = 1 + (\alpha - 1)^2, \quad (2.22)$$

$$\alpha_{thresh,\pm} = 1 \pm \sqrt{F^2 - 1}. \quad (2.23)$$

These equations explicitly describe the point at which comb is generated in an experiment in which the pump power or detuning is varied while the other is held fixed.

### 2.3.2 Kerr comb outputs: extended modulation-instability patterns

Extended temporal patterns arise spontaneously as a result of the instability of the flat solution to the LLE when the pump laser is tuned above the threshold curve. Two types of extended patterns are shown in Fig. 2.6. These patterns can be stationary, in which case they are typically referred to as ‘Turing patterns’ or ‘primary comb,’ or can evolve in time, in which case they are typically referred to as ‘noisy comb’ or ‘spatiotemporal chaos.’ In general, the former occurs for lower values of the detuning  $\alpha$  and smaller pump strengths  $F^2$ ; although some studies of the transition from Turing patterns to chaos have been conducted (e.g. Ref. [64]), a well-defined boundary between the two has not been established, and may not exist.

In the spatial domain parametrized by  $\theta$ , a Turing pattern consists of a pulse train with (typically)  $n \gg 1$  pulses in the domain  $-\pi \leq \theta \leq \pi$ —the pulse train’s repetition rate is a multiple of

the cavity FSR:  $f_{rep} = n \times f_{FSR}$ . Corresponding to the  $n$ -fold decreased period (relative to the round-trip time) of an  $n$ -pulse Turing pattern's modulated waveform in the time domain, the optical spectrum of a Turing pattern consists of modes spaced by  $n$  resonator FSR—it is this widely-spaced spectrum that is referred to as ‘primary comb.’ Analytical approximations for Turing patterns are possible near threshold [65, 66] and in the small damping limit [67]. The stability analysis results from the last section can be used to predict the spacing  $n$  of a primary comb (equivalently the number of Turing-pattern pulses) generated in a decreasing-frequency scan across the resonance with fixed normalized pump power  $F^2$ :

$$n = \mu_{max,thresh} = \sqrt{\Delta\omega_0(1 + \sqrt{F^2 - 1})/D_2}, \quad (2.24)$$

which is obtained by inserting  $\alpha_{thresh,-}$  from Eq. 2.23 and  $\rho = 1$  into the expression for  $\mu_{max}$  in Eq. 2.21 above and moving to the dimensionful dispersion parameter  $D_2$ . Fig. 2.6a shows measured and simulated primary comb spectra and Fig. 2.6b shows the corresponding simulated time-domain waveform.

Spatiotemporal chaos can be understood as a Turing pattern whose pulses oscillate in height, with adjacent pulses oscillating out of phase. From such an oscillating Turing pattern, if  $\alpha$  and/or  $F^2$  is increased, one moves deeper into the chaotic regime and pulses begin to exhibit lateral motion and collisions; the number of pulses present in the cavity is no longer constant in time. Depending on the severity of the chaos (greater for larger  $\alpha$  and  $F^2$ ), a chaotic comb may correspond to a primary-comb-type spectrum with each primary-comb mode exhibiting sidebands at the resonator FSR, so-called ‘subcombs,’ or it may correspond to a spectrum with light in each cavity mode. Fig. 2.6c shows measured and simulated time-averaged spectra of chaotic combs and Fig. 2.6d shows a corresponding simulated time-domain waveform.

Relative to generation of solitons, discussed below, experimental generation of an extended pattern is straightforward. These patterns are generated with blue effective pump-laser detuning  $\alpha_{eff} < 0$ , where thermal locking can occur. Because they arise spontaneously from noise, their generation is (comparatively) straightforward: simply decrease the pump-laser frequency until a

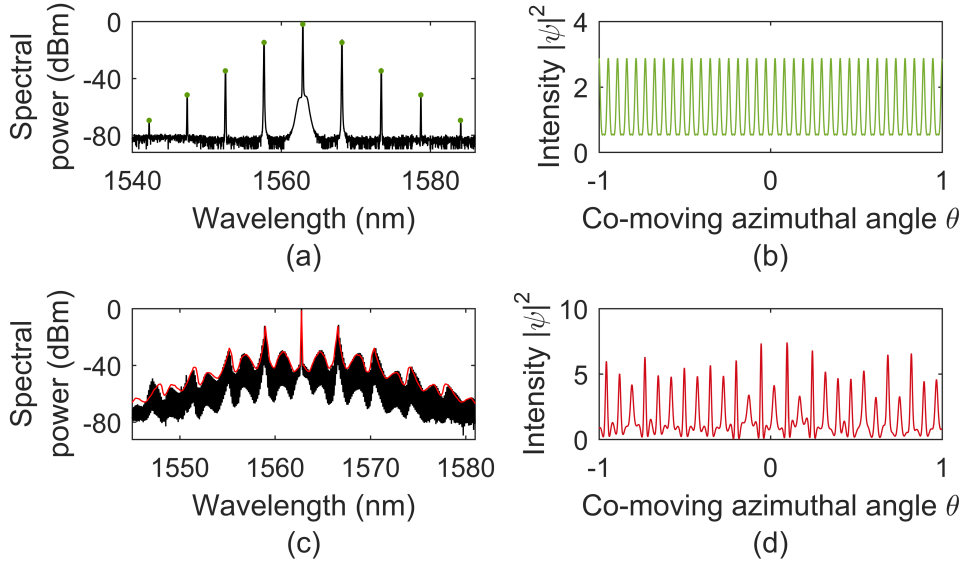


Figure 2.6: **Extended-pattern solutions to the LLE.** (a,b) Primary-comb pulse train in the frequency (a) and time (b) domains. The primary-comb spectrum corresponds to 39 time-domain pulses. The experimental optical spectrum (black) was obtained in a microdisk resonator with 17.32 GHz free-spectral range, and the simulation (green) is conducted with parameters near typical experimental values:  $F^2=6$ ,  $\alpha = -0.6$ , and  $\beta_2 = -0.0044$ . (c,d) Spatiotemporal chaos obtained in the same resonator. The experimental measurement (black) yields a time-averaged optical spectrum, with a simulation of qualitatively similar dynamics shown in red. Simulation parameters are  $F^2 = 4.2$ ,  $\alpha = 1.2$ , and  $\beta_2 = -0.0054$ . A snapshot of the evolving time-domain waveform is shown in (d).

pattern is generated. Unfortunately, operation of a Kerr-comb in the extended pattern regime is disadvantageous for applications: the  $n$ -FSR spacing of primary comb presents a challenge for measurement of the repetition rate of the frequency comb due to the bandwidth of measurement electronics and is also an inefficient use of physical space (i.e. for an  $n$ -pulse primary comb pulse train, an equivalent pulse train can always be obtained using the single-soliton output of a resonator with area that is smaller by a factor of  $1/n^2$ ), and the aperiodic time-evolution of chaotic comb corresponds to modulation sidebands on the comb modes within the linewidth of the cavity that preclude the use of the comb as a set of stable optical reference frequencies.

An important property of these extended patterns is that they fill the resonator—the characteristic size of temporal features scales roughly as  $1/\sqrt{-\beta_2}$ , but these features are distributed densely and uniformly throughout the resonator. This means that the total circulating power of an

extended pattern  $\int d\theta |\psi|^2$  is large relative to the localized pulses discussed in the next section, and therefore that extended patterns come with a comparatively large thermal shift of the resonance. As explained below, this contributes to the experimental challenges in soliton generation.

### 2.3.3 Kerr comb outputs: solitons

The term ‘soliton’ generally refers to a localized excitation that can propagate without changing its shape due to a delicate balance between dispersion (or diffraction) and nonlinearity; sometimes known as ‘solitary waves,’ solitons entered the scientific consciousness in the nineteenth century with their observation by John Scott Russell [68]. They are fundamental solutions to nonlinear partial-differential equations that describe a host of physical phenomena, and are found in several contexts within the field of nonlinear optics: spatial[65, 69] and spatiotemporal solitons (light bullets) [70] have been studied, and soliton modelocking [71, 72] is an important method of femtosecond pulse generation. Temporal Kerr-soliton pulses in optical fibers are particularly well known [40, 73], and have been considered as a candidate for fiber-optic communications protocols [74, 75]. Microresonators support so-called dissipative cavity solitons, which are localized pulses circulating the resonator that are out-coupled once per round trip. In the case of a single circulating soliton, this leads to a train of pulses propagating away from the resonator with repetition rate  $1/T_{RT}$ . Thus the mode spacing of the comb matches the FSR of the resonator, in contrast with widely-spaced primary comb spectra, and the soliton can, in principle, remain stable and propagate indefinitely as a stationary solution to the LLE. This makes Kerr combs based on solitons particularly attractive for applications.

#### 2.3.3.1 Mathematical description of solitons

Solitons in optical fibers are solutions of the nonlinear Schrodinger equation (NLSE) that describes pulse-propagation in optical fiber [40]:

$$\frac{\partial A}{\partial z} = i\gamma|A|^2 A - i\frac{k''}{2}\frac{\partial^2 A}{\partial T^2}. \quad (2.25)$$

This equation describes the evolution of the pulse envelope  $A$  in the ‘fast-time’ reference frame parametrized by  $T$  as it propagates down the length of the fiber, parametrized by the distance variable  $z$ . Here  $\gamma = \frac{2\pi}{\lambda} \frac{n_2}{A_{eff}}$  is the nonlinear coefficient of the fiber, where  $n_2$  is the Kerr index,  $A_{eff}$  is the effective nonlinear mode area and  $\lambda$  is the carrier wavelength, and  $k'' < 0$  is the GVD parameter. The LLE can be viewed as an NLSE with additional loss and detuning terms  $-(1+i\alpha)\psi$  and a driving term  $F$ .

The fundamental soliton solution to the NLSE is:

$$A_{sol} = \sqrt{P_0} \operatorname{sech}(T/\tau) e^{i\gamma P_0 z/2 + i\phi_0}, \quad (2.26)$$

where  $P_0$  is the peak power of the pulse and is related to the duration of the pulse  $\tau$  via  $\tau = \sqrt{-l''/\gamma P_0}$ , and  $\phi_0$  is an arbitrary phase. Thus, this equation admits a *continuum* of pulsed fundamental ‘soliton’ solutions, with one existing for each value of the peak power. Each of these solutions propagates down the fiber without changing shape; only the phase evolves with distance as  $\phi(z) = \gamma P_0 z/2 + \phi_0$ .

The introduction of the loss, detuning, and driving terms into the NLSE to obtain the LLE has several important consequences for solitons. First, exact analytical expressions for the soliton solution to the LLE in terms of elementary functions are not known, in contrast with the situation for the NLSE. However, the soliton solutions to the LLE, Eq. 2.12, can be approximated well as:

$$\psi_{sol} = \psi_{CW,min} + e^{i\phi_0} \sqrt{2\alpha} \operatorname{sech} \sqrt{\frac{2\alpha}{-\beta_2}} \theta. \quad (2.27)$$

Here  $\psi_{CW,min}$  is the flat solution to the LLE from Eq. 2.20 at the point where the soliton solution is desired; when multiple flat solutions exist,  $\psi_{CW,min}$  is the one corresponding to the smallest intensity  $\rho_1$ . The phase  $\phi_0 = \cos^{-1}(\sqrt{8\alpha}/\pi F)$  arises from the intensity-dependent phase shift in the cavity due to the Kerr effect, mathematically described by the term  $i|\psi|^2\psi$ . We depict this approximation, alongside numerical calculations of exact soliton solutions to the LLE, in Fig. 2.7.

This approximation  $\psi_{sol}$  from Eq. 2.27 for the soliton solution of the LLE illustrates a second important consequence of the differences between the NLSE and the LLE: while the NLSE admits a continuum of fundamental soliton solutions parametrized by their peak power  $P_0$  and arbitrary phase

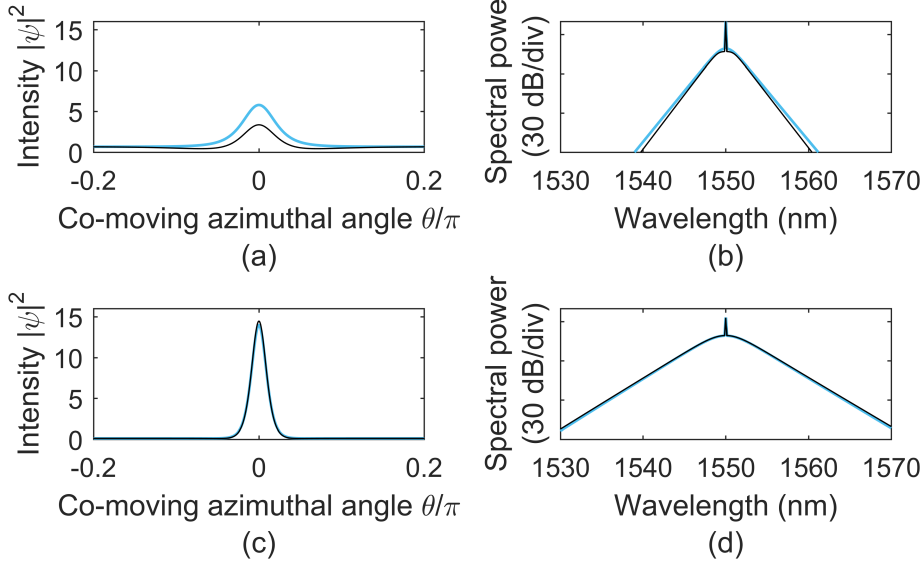


Figure 2.7: **Soliton solutions to the LLE.** Analytical approximations (color) and numerically-calculated exact solutions (black) to the LLE in the time (a,c) and frequency (b,d) domains. The solitons are calculated at  $\alpha = 0.95 \alpha_{max} = 0.95 \pi^2 F^2 / 8$  for  $F^2 = 8\sqrt{3}/9$  (a,b) and  $F^2 = 6$  (c,d) with  $\beta_2 = -0.02$  in both cases. The isolated spectral spike is at the pump frequency and corresponds to the CW background  $\psi_{CW,min}$ . Spectra are calculated using  $f_{rep} = 16.5$  GHz with pump wavelength of  $\lambda_p = 1550$  nm. For experimental measurements of solitons in microring resonators, see Chapters 3 and 4.

$\phi_0$ , the LLE supports only one shape for the envelope of a soliton for fixed experimental parameters. Intuitively, this can be understood as arising from the need for the round-trip phase shift for all points on the soliton to be zero in steady-state; the introduction of the detuning parameter  $\alpha$  breaks the degeneracy that exists for the NLSE within the continuum of soliton solutions.

The analytical approximation in Eq. 2.27 indicates the scaling of the amplitude and width of the LLE soliton with the experimental parameters: the amplitude of the LLE soliton, prior to its summation with the CW background, depends only on the detuning  $\alpha$ , and the width of the soliton increases with larger detuning  $\alpha$  and smaller dispersion  $\beta_2$ . Importantly, if one is concerned with maximizing the bandwidth of the soliton, it is important to minimize  $\beta_2$  and maximize  $\alpha$ , due to the inverse relationship between temporal duration and spectral bandwidth. The spectrum of a single-soliton Kerr comb has a  $\text{sech}^2((\omega - \omega_p)/\Delta\omega_{sol})$  envelope, where  $\omega$  is the optical angular frequency and  $\Delta\omega_{sol} \approx \sqrt{32\alpha/|\beta_2|T_{RT}^2}$  is the bandwidth of the pulse in angular frequency. Equivalently,

the bandwidth of the soliton in (linear) optical frequency is  $\sqrt{\frac{16\Delta\nu f_{rep}^2}{D_2}}\alpha$ , where  $\Delta\nu$  is the resonance linewidth in linear frequency; the spectral width in mode number is  $\Delta\mu_{sol} \approx 4\sqrt{\alpha\Delta\nu/D_2}$ . Consistent with the phase  $\phi_0$  in the approximation  $\psi_{sol}$  in Eq. 2.27, solitons can exist up to a maximum detuning of  $\alpha_{max} \sim \pi^2 F^2/8$  [54]. For a soliton at the maximum detuning for fixed normalized pump power  $F^2$ , the bandwidth is then  $\sqrt{\frac{\pi^2\Delta\nu f_{rep}^2}{2D_2}F^2}$ .

Solitons exist only where there is a stable flat solution  $\psi_{CW}$  that is effectively red detuned that can form the background for the pulse [63, 76]. This effectively red-detuned background is itself thermally unstable (see Sec. 2.1.2), but the existence of the soliton acts to stabilize the pump detuning. As explained by Herr et al., the soliton provides a local modulation of the refractive index through the Kerr effect, which changes the round-trip phase shift of pump light that arrives coincidentally with the soliton at the coupling port [54]. This leads to a *local* increase in the resonant wavelength for this pump light. Thus there are effectively two resonant wavelengths, a smaller one determined by the round-trip phase shift including the Kerr shift from the CW background, and a larger one determined by the round-trip phase shift including the Kerr shift from the soliton [77]. The pump laser can be effectively blue-detuned with respect to the latter resonance, which can lead to thermally stable operation in the soliton regime.

Solitons are strongly localized: as can be seen from Eq. 2.27, the deviation of the background intensity from  $\rho_1$  near a soliton at  $\theta_0$  is proportional to  $e^{-(\theta-\theta_0)/\delta\theta}$ , where  $\delta\theta = \sqrt{-\beta_2/2\alpha}$ . If  $\delta\theta$  is sufficiently small, multiple solitons can be supported in the resonator domain  $-\pi \leq \theta \leq \pi$  with very weak interactions between solitons. If the separation between solitons  $i$  and  $j$  at  $\theta_i$  and  $\theta_j$  is small relative to  $\delta\theta$ , the solitons will interact. The topic of soliton interactions is complicated in general, with different types of interactions in different systems (see e.g. Refs. [78–81]). Simulations reveal that if  $(\theta_i - \theta_j)/\delta\theta$  is too small, LLE solitons exhibit attractive interactions as a result of the monotonic (as opposed to oscillatory) decay of the localized pulse to  $\psi_{CW}$  [82], which precludes the existence of stable equilibrium separations. The result of this attraction can be pair-wise annihilation or merger, with the ultimate result being an ensemble with fewer solitons. The maximum number of solitons that can coexist in a resonator in the absence of higher-order stabilizing effects (see Chapter

4 and Refs. [82, 83]) can be approximated as  $N_{max} \approx \sqrt{-2/\beta_2}$  [54]. An approximation to the form of a soliton ensemble is possible as:

$$\psi_{ens} = \psi_{CW,min} + e^{i\phi_0} \sqrt{2\alpha} \sum_j \operatorname{sech} \left( \sqrt{\frac{2\alpha}{-\beta_2}} (\theta - \theta_j) \right), \quad (2.28)$$

where  $\{\theta_j\}$  define the positions of the solitons in the ensemble and  $\phi_0 = \cos^{-1}(\sqrt{8\alpha}/\pi F)$  as above.

Fig. 2.8 provides an example illustrating the degeneracy in soliton number of Kerr-combs operating in the soliton regime.

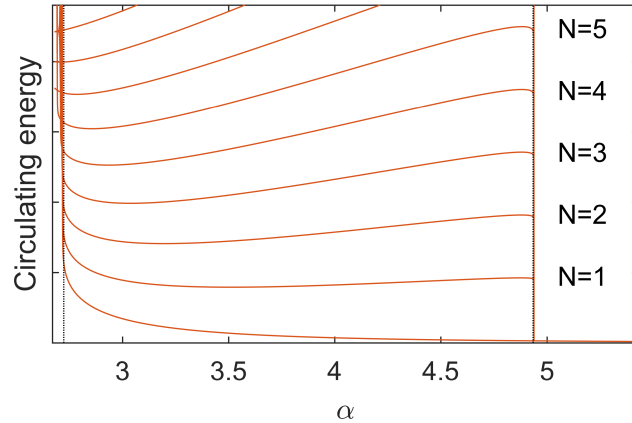


Figure 2.8: **Kerr-soliton energy-level diagram.** Some of the possible values of the circulating energy (proportional to  $\int d\theta |\psi|^2$ ) in the soliton regime as a function of the detuning parameter  $\alpha$ . Level curves correspond to the number of circulating solitons. This diagram is obtained from numerical solutions using  $F^2 = 4$ ,  $\beta_2 = -0.0187$ , and is quantitatively dependent on both of these parameters. Dotted vertical lines indicate approximations to the minimum and maximum detunings for solitons. The approximation for the minimum detuning is the value of  $\alpha$  at which the effectively red-detuned branch vanishes, obtained by inserting  $\rho_-$  (Eq. 2.19) into Eq. 2.17 for  $F^2 = 4$  and solving for  $\alpha$ , and the approximate maximum detuning is  $\alpha_{max} = \pi^2 F^2 / 8$ .

### 2.3.3.2 Microresonator solitons in experiments

Relative to the generation of extended modulation-instability patterns, experimental generation of solitons in microring resonators is challenging. Solitons are localized excitations below threshold, which means that their existence is degenerate with their absence—a resonator can host  $N = 0, 1, 2, \dots$  up to  $N_{max}$  solitons for a given set of parameters  $\alpha$  and  $F^2$ ; as discussed above and illustrated in Fig. 2.8. If  $\alpha$  and  $F^2$  are experimentally tuned to a point at which solitons may

exist,  $\psi$  will evolve to a form determined by the initial conditions of the field  $\psi_0$ . To provide initial conditions that evolve to  $N > 0$  solitons, most experimental demonstrations of soliton generation have involved first generating an extended pattern in the resonator, and then tuning to an appropriate point  $(\alpha, F^2)$  so that ‘condensation’ of solitons from the extended pattern occurs.

Condensation of solitons from an extended pattern presents additional challenges. First, it is difficult to control the number of solitons that emerge, due to the high degree of soliton-number degeneracy as shown in Fig. 2.8. This typically leads to a success rate somewhat lower than 100 % in the generation of single solitons. Second, the transition from a high duty-cycle extended pattern to a lower duty-cycle ensemble of one or several solitons comes with a dramatic drop in intracavity power that occurs on the timescale of the photon lifetime. If the resonator is in thermal steady-state before this drop occurs, the resonator will cool and the resonance frequency will increase. If this increase is large enough that the final detuning  $\alpha$  exceeds  $\alpha_{max} = \pi^2 F^2 / 8$ , the soliton is lost. This challenge can be addressed by preparing initial conditions for soliton generation and then tuning to an appropriate point  $(\alpha, F^2)$  faster than the cavity can come into thermal steady-state at the temperature determined by the larger power of the extended pattern; this is possible because the timescale over which an extended pattern can be generated is related to the photon lifetime, which is typically much faster than the thermal timescale.

The first report of soliton generation in microresonators came in 2012 in a paper by Herr et al. [54] (2012 pre-print [53]). These authors described optimizing the speed of a decreasing-frequency scan of the pump laser across the cavity resonance so that solitons could be condensed from an extended pattern and the scan could then be halted at a laser frequency where the solitons could be maintained with the system in thermal steady-state at the temperature determined by the circulating power of the solitons. Stochastic reduction in the number of solitons in the resonator after condensation from an extended pattern was identified in these experiments. This corresponds to transitions between levels in the diagram in Fig. 2.8, and is associated with discrete steps in a measurement of the ‘comb power,’ the output power of the resonator with the pump frequency  $\nu_p$  filtered out. The resulting staircase-like nature of a comb power measurement is a useful experimental

signature of soliton generation in microresonators, and is important for comparison with the results described in Chapter 3.

Other approaches for dealing with the challenges described above have been developed since this first demonstration; these include fast manipulation of the pump power [30, 84] or frequency [85], periodic modulation of the pump laser’s phase or power at  $f_{FSR}$  [37, 86], tuning of the cavity resonance frequency using chip-integrated heaters instead of tuning the pump-laser frequency [87, 88], and soliton-ensemble preparation and subsequent population reduction through manipulation of the pump laser [77]. These methods continue to make use of extended patterns to provide initial conditions for soliton generation. In formally-equivalent fiber-ring resonators, direct generation of solitons without condensation from an extended pattern has been demonstrated using transient phase and/or amplitude modulation of the pump laser [89–91].

### **2.3.3.3 Microresonator solitons in applications**

Because solitons have single-FSR spacing, have the output localized into a high peak-power pulse, and are stationary (in contrast with chaos, which has single-FSR spacing but is not stationary), they are promising for applications. Many of the proposals for and demonstrations of applications with Kerr-combs have used single-soliton operation. Some of the applications already demonstrated include an optical clock [92], dual-comb spectroscopy [93], coherent communications [94], and direct on-chip optical frequency synthesis [18]. Additionally, soliton combs have been self-referenced both with [95, 96] and without [19, 97] external spectral broadening. Nevertheless, there remains work to be done to bring microresonator-soliton technology to the level of maturity that will be required for deployment in the field. Chapters 3 and 4 describe two recent advancements: the development of a method for direct on-demand generation of single solitons by use of a phase-modulated pump laser, and the observation and explanation of a soliton-interaction mechanism that imparts rigid structure on the allowed configurations of multi-soliton ensembles.

## Chapter 3

### Generation and control of single microresonator solitons using a phase-modulated pump laser

This chapter discusses the direct generation and control of single solitons in optical microring resonators using a pump laser phase modulated at a frequency near the resonator's free spectral range. Based on a proposal by Taheri, Eftekhar, and Adibi in 2015 [98], these results present a promising new method for simple and deterministic generation of single solitons. We build on a body of work describing past applications of pump-laser modulation to facilitate the generation of microresonator solitons. Lobanov et al. demonstrated that phase and/or intensity modulation can enable deterministic condensation of either one or zero solitons from an extended modulation-instability pattern [86], and transient bursts of phase modulation [89] and amplitude modulation [91] have been used to directly excite solitons in fiber-ring resonators. Control of fiber-ring solitons by phase modulation has been demonstrated in similar experiments [90]. Generation of solitons using a train of pump pulses with repetition-rate matched to the resonator FSR has also been demonstrated [37]. The work we present here builds on these previous demonstrations by reducing the complexity of the scheme; all that is required is sinusoidal phase modulation of the pump with reasonably low modulation index, and no transient perturbation to the system parameters is necessary.

We begin by presenting theoretical investigations into the effect of phase modulation (PM) at the resonator free-spectral range on solitons in microresonators, and then we demonstrate deterministic generation and control of single solitons using pump-laser phase modulation.

### 3.1 Theoretical investigation of soliton generation with a phase-modulated pump laser

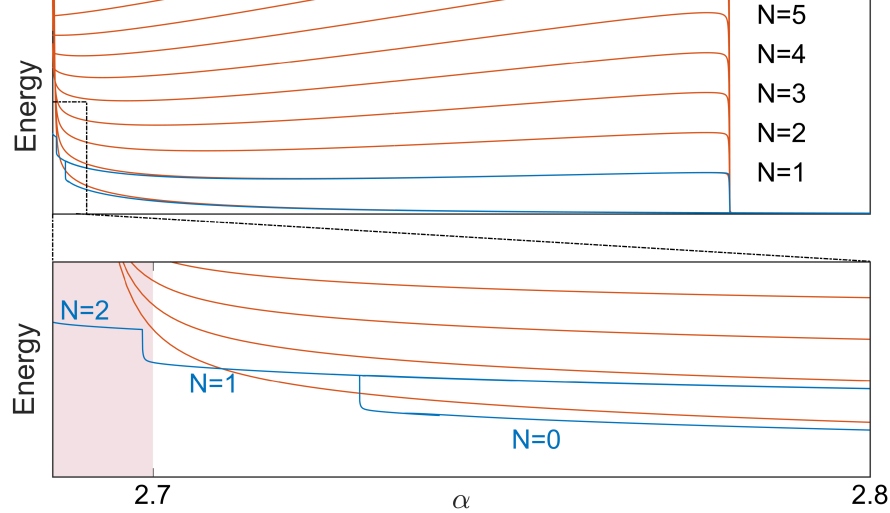


Figure 3.1: **Energy-level diagram with a phase-modulated pump laser.** An energy-level diagram with a phase-modulated pump laser (blue levels), on top of the diagram for a CW laser from Fig. 2.8. Phase modulation eliminates the degeneracy between the  $N = 1$  level and all other levels over a range of detunings near the minimum detuning for solitons, and also precludes the existence of stable multi-soliton ensembles over the majority of the range where solitons are supported. Although the interval over which  $N$  is restricted to 1 is fairly narrow, we find that it is readily accessible in experiment. Simulations indicate that non-stationary solutions are degenerate with the  $N = 2$  level for  $\alpha \leq 2.7$ ; this region is highlighted with the red shading. The level-diagram is created using an LLE simulation with  $F^2 = 4$ ,  $\beta_2 = -0.0187$  (chosen to match the dispersion of the resonator used for experiments), and  $\delta_{PM} = \pi$ .

To theoretically explore the physics of soliton generation with PM pumping<sup>1</sup>, we use the LLE with a modified driving term that incorporates the effect of phase modulation [98]:

$$\frac{\partial \psi}{\partial \tau} = -(1 + i\alpha)\psi + i|\psi|^2\psi - i\frac{\beta_2}{2}\frac{\partial^2 \psi}{\partial \theta^2} + Fe^{i\delta_{PM} \cos \theta}. \quad (3.1)$$

Here  $\delta_{PM}$  represents the phase-modulation index, which describes the phase-modulated input field according to  $E_{PM} = E_0 e^{i\delta_{PM} \cos(2\pi f_{PM} t)}$ ;  $f_{PM} \sim f_{FSR}$  is the frequency of the applied phase modulation.

Simulations of Eq. 3.1 reveal that PM transforms the resonator excitation spectrum from a series of  $N = 0, 1, 2, \dots$  up to  $N_{max}$  solitons to a single level  $N = 1$  near threshold, eliminating

<sup>1</sup> I gratefully acknowledge the contributions of Miro Erkintalo, who originated the approximation of the derivatives of  $\phi$  as zero and suggested the mechanism of locally-vanishing bistability for soliton generation.

degeneracy between these states as shown in Fig. 3.1. This occurs due to spatial variations of effective loss and detuning parameters that result from the phase modulation. We can obtain an approximation for these parameters by inserting the ansatz  $\psi(\theta, \tau) = \phi(\theta, \tau)e^{i\delta_{PM} \cos(\theta)}$  into the stationary ( $\partial\psi/\partial\tau = 0$ ) version of Eq. 3.1 [90]. By expanding the second-derivative term and setting derivatives of  $\phi$  to zero we arrive at an equation for the quasi-CW background in the PM-pumped resonator:

$$F = (\gamma(\theta) + i\eta(\theta))\phi - i|\phi|^2\phi, \quad (3.2)$$

where the spatially-varying effective loss and detuning terms have been defined as:

$$\gamma(\theta) = 1 + \frac{\beta_2}{2}\delta_{PM} \cos \theta, \quad (3.3)$$

$$\eta(\theta) = \alpha - \frac{\beta_2}{2}\delta_{PM}^2 \sin^2 \theta. \quad (3.4)$$

This equation immediately yields an approximation for the stationary solution  $\psi_s$ :

$$\psi_s(\theta) = \frac{Fe^{i\delta_{PM} \cos \theta}}{\gamma(\theta) + i(\eta(\theta) - \rho(\theta))}, \quad (3.5)$$

where  $\rho(\theta) = |\phi(\theta)|^2$  is the (smallest real) solution to the cubic polynomial that results from taking the modulus-square of Eq. 3.2:

$$F^2 = \left[ \gamma(\theta)^2 + (\eta(\theta) - \rho(\theta))^2 \right] \rho(\theta). \quad (3.6)$$

In neglecting spatial derivatives of  $\phi$  but retaining the derivatives of the phase term  $e^{i\delta_{PM} \cos \theta}$  we have made the approximation that the dominant effect of dispersion comes from its action on the existing broadband phase-modulation spectrum. This model reveals that amplitude variations in the quasi-CW background can be expected as a result of the spatially-varying effective loss and detuning terms that arise from pase modulation of the pump laser.

Fig. 3.2 shows the predictions of simulations of Eq. 3.1 (color) and the analytical model Eq. 3.6 (black). The two agree quantitatively for weak modulation ( $\delta_{PM} = \pi/2$ , blue) and qualitatively with larger depth ( $\delta_{PM} = 4\pi$ , green); both indicate that the field  $\psi$  exhibits amplitude variations due to the spatially-varying effective loss and detuning. This phenomenon suggests an explanation

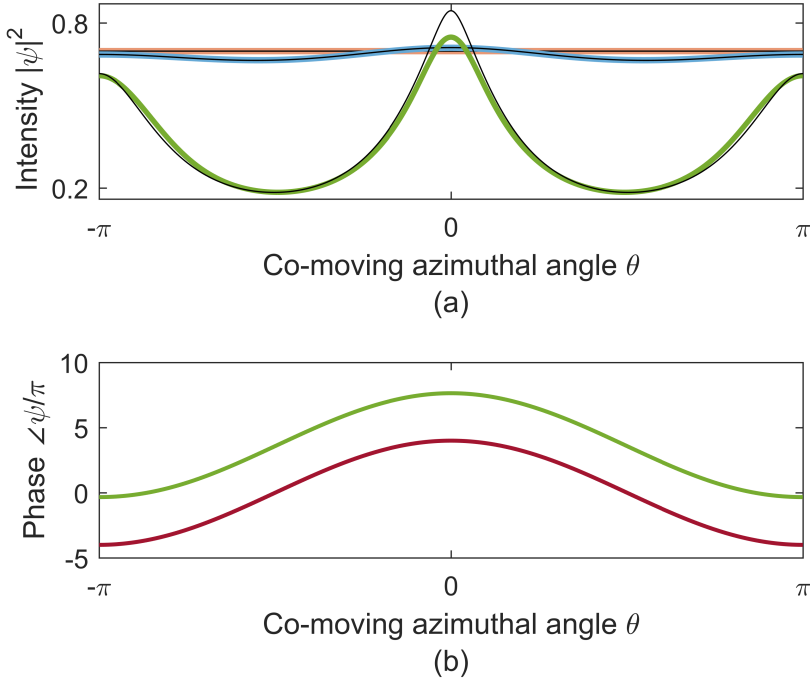


Figure 3.2: **Quasi-CW background in a PM-pumped resonator.** (a) Simulated intensity of the background in the resonator without (orange) and with PM of depth  $\delta_{PM} = \pi/2$  (blue) and  $\delta_{PM} = 4\pi$  (green), with analytical approximations in black. Here  $\alpha$  is slightly larger than the critical value for soliton formation. (b) Phase profile of the field  $\psi$  corresponding to the green trace in (a) with  $\delta_{PM} = 4\pi$ , and the phase profile of the driving term  $F e^{i\delta_{PM}\cos\theta}$  (red) with modulation depth  $4\pi$ . The phase of the field is very nearly the phase of the drive plus a constant offset.

for the spontaneous formation of a single soliton as the detuning  $\alpha$  is decreased in terms of the local disappearance of Kerr bistability.

As discussed in Sec. 2.3.1, for the LLE with a CW pump the background field  $\psi_s$  can take one of two stable values over a range of the parameters  $\alpha$  and  $F^2$ . This leads to the emergence of a tilted resonance lineshape like the one shown in Fig. 3.3a, with an effectively red-detuned branch lying at higher values of  $\alpha$ , an effectively blue-detuned branch lying at lower values of  $\alpha$ , and an interval in  $\alpha$  over which they both exist and the system is bistable (recall that the middle branch is unstable). With spatially-varying effective loss and detuning terms, the field  $\psi_s(\theta)$  described by Eq. 3.5 now takes a value at each point in the cavity that is determined by the local parameters  $\gamma(\theta)$  and  $\eta(\theta)$ , with the result that each point lies on its own effective resonance. The resulting resonance *surface* is

shown in Fig. 3.3b. It can be independently determined for each point in the cavity whether  $\psi_s(\theta)$  exhibits bistability. Applying the analysis presented in Sec. 2.3.1 to Eq. 3.6, we identify the value of  $\rho$  associated with the disappearance of the bistability in a decreasing- $\alpha$  scan as the smaller value  $\rho_-$  at which  $\partial F^2/\partial \rho = 0$ :

$$\rho_- = \left( 2\eta - \sqrt{\eta^2 - 3\gamma^2} \right) / 3, \quad (3.7)$$

For fixed  $F^2$  the function  $\alpha_{crit}(\theta)$  describing the critical value of  $\alpha$  at which the bistability ends is found by numerically solving the implicit equation for  $\alpha_{crit}$  obtained by inserting  $\rho_-$  into Eq. 3.2:

$$F^2 = \left[ \gamma^2(\theta) + (\eta(\theta) - \rho_-(\theta))^2 \right] \rho_-(\theta), \quad (3.8)$$

where  $\alpha_{crit}(\theta)$  is included via  $\eta(\theta) = \alpha_{crit}(\theta) - \frac{\beta_2}{2} \delta_{PM}^2 \sin^2 \theta$ . Fig. 3.3c shows a calculation of  $\alpha_{crit}(\theta)$  for  $F^2 = 4$  and  $\beta_2 = -0.0187$ , which is chosen to match the dispersion of the resonator used for the experiments presented below. For  $\theta = 0$  this calculation predicts disappearance of the bistability, and subsequent soliton generation, at  $\alpha = 2.741$ , which is a difference of 0.4 % from the value  $\alpha = 2.729$  observed in the simulation presented in Fig. 3.1. The same calculation predicts disappearance of the bistability for  $\theta = \pi$  at  $\alpha = 2.705$ , also in close agreement with the simulation.

### 3.2 Spontaneous generation of single solitons using a phase-modulated pump laser

We demonstrate deterministic generation of single solitons without condensation from an extended pattern in a 22-GHz FSR silica microdisk resonator. This resonator has  $\Delta\nu \sim 1.5$  MHz linewidth, and was fabricated using a chemical etching process at CalTech [29]. We generate a frequency-agile laser for pumping the resonator by passing a CW seed laser through a single-sideband modulator (SSB) that is driven by a voltage-controlled oscillator (VCO) [85]. The seed laser is extinguished in the modulator and the resulting sideband can be swept by adjusting the voltage applied to the VCO; sweeping rates up to 100 GHz/ $\mu$ s over a range over 4 GHz are possible. The pump laser is phase-modulated with index  $\delta_{PM} \sim \pi$  and amplified to normalized power  $F^2$  between 2 and 6. We are able to measure the pump-laser detuning in real time using an AOM-shifted probe beam

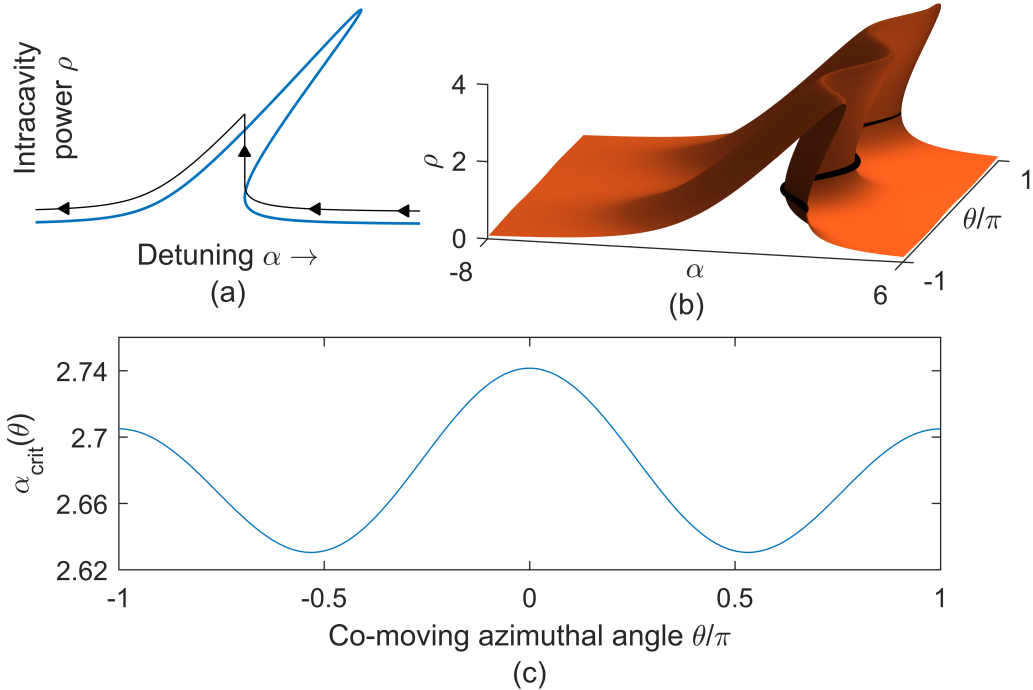


**Figure 3.3: Mechanism for soliton generation with a PM pump.** (a) Plot of a Kerr-shifted resonance, here with  $F^2=12$ . The CW background field  $\psi$  follows the black curve in an increasing-frequency scan of the pump laser. (b) For the case of a phase-modulated pump, the field  $\psi_s(\theta)$  at each point  $\theta$  lies on a qualitatively similar resonance that is defined locally by  $\gamma(\theta)$  and  $\eta(\theta)$ , with the result that a resonance surface emerges. The resonance surface is shown here for  $F^2 = 4$ ,  $\beta_2 = -0.0187$ , and  $d_{PM} = 4\pi$ , which is chosen to accentuate the  $\theta$ -dependence. The curve  $\alpha_{crit}(\theta)$  is shown in black. (c) A plot of the value  $\alpha_{crit}(\theta)$  at which the Kerr bistability locally vanishes and the field  $\psi_s(\theta)$  must jump to the effectively blue-detuned branch, associated with the vertical transition in (a), for  $F^2 = 4$ ,  $\beta_2 = -0.0187$ , and  $\delta_{PM} = \pi$ . The value  $\alpha_{crit}(\theta = 0)$  can be used to approximate the detuning at which a soliton is generated in an increasing-frequency scan of the pump laser; the input parameters here match the level diagram in Fig. 3.1.

as shown in Fig. 3.4, and the high-bandwidth feedback allowed by the VCO/SSB scheme allows thermal instabilities associated with the red detuning that is required for soliton generation to be overcome.

To generate single solitons, we begin with large red detuning  $\nu_0 - \nu_{pump} = 40$  MHz and decrease the detuning until a soliton is generated near  $\nu_0 - \nu_{pump} \sim 5$  MHz detuning; this value depends on the pump power and coupling condition. We measure the power converted by the Kerr nonlinearity to new frequencies by passing a portion of the resonator's output through an optical band-reject filter; this 'comb power' measurement reveals a step upon soliton formation, as shown in Fig. 3.5a, after

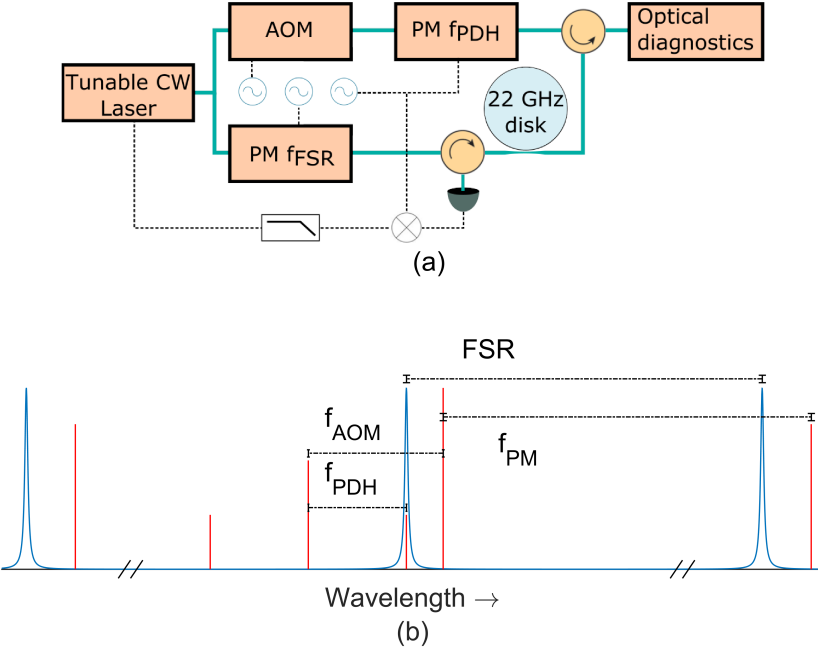


**Figure 3.4: Experimental setup for soliton generation with a phase-modulated pump laser.** (a) Schematic diagram of the experimental setup, including the pump laser phase-modulated at frequency  $f_{PM} \sim f_{FSR}$  and an AOM-shifted probe beam that is modulated at frequency  $f_{PDH}$  for implementation of a Pound-Drever-Hall sideband lock. The probe beam addresses the resonator in the counter-propagating direction. (b) Frequency-domain diagram of the scheme used to maintain stable red detuning of the pump laser. As  $f_{PDH}$  is increased, the detuning  $\alpha$  is decreased.

which we can measure the soliton spectrum with phase-modulation sidebands on the pump shown in Fig. 3.5b. After soliton generation, we observe that the soliton can be preserved while the detuning is increased again, consistent with Fig. 3.1. Additionally, we observe that it is possible to turn off the phase modulation without loss of the soliton, in agreement with the simulations presented in Ref. [98].

Automating soliton generation by repeatedly scanning the laser into resonance ( $\nu_0 - \nu_{pump} \sim 5$  MHz) and back out again ( $\nu_0 - \nu_{pump} \sim 20$  MHz, far enough that the soliton is lost) has enabled reversible generation of 1000 solitons in 1000 trials over 100 seconds, with a measured 100 % success rate. Our probe beam allows measurement of the detuning at which soliton generation occurs, which changes little from run to run. We present a histogram of detuning measurements for the generation of 160 solitons in Fig. 3.5c.

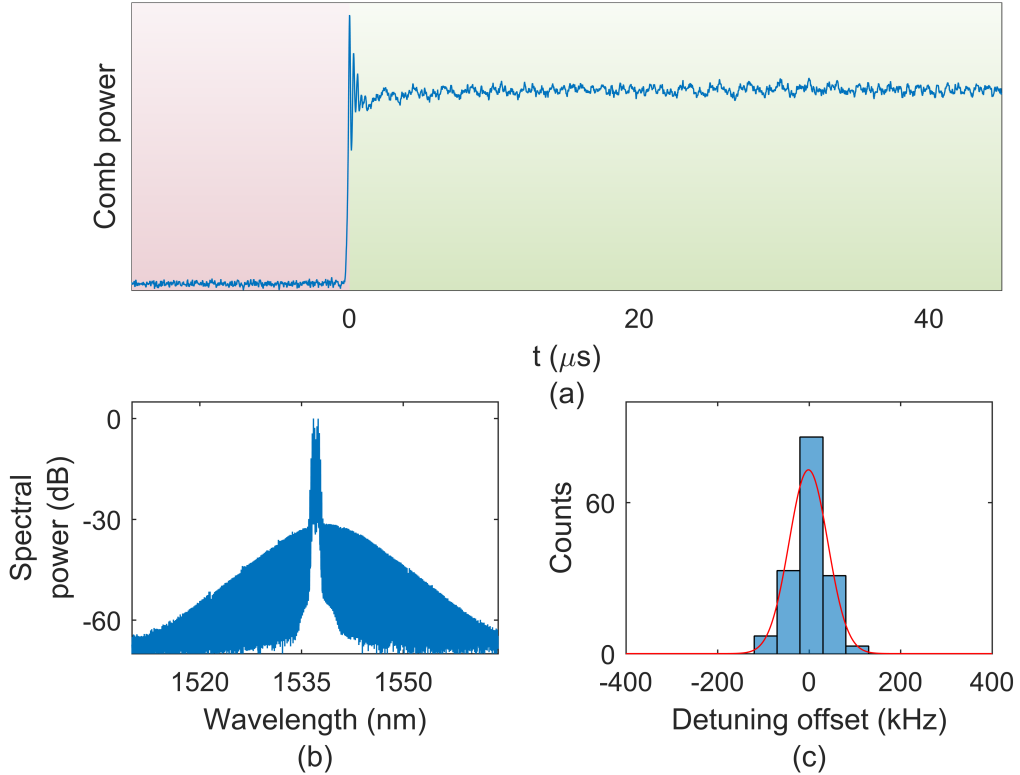


**Figure 3.5: Spontaneous generation of solitons using a phase-modulated pump laser.** (a) ‘Comb power’ trace obtained by filtering the pump laser out of the spectrum of light transmitted past the resonator, indicating a discrete step in the amount of frequency-converted light upon direct generation of a soliton. (b) Optical spectrum of a spontaneously generated soliton. The spectrum of the phase-modulated pump laser is visible as the set of higher-amplitude lines in the center. (c) Histogram of measured detuning values at which a soliton is generated relative to a reference (mean) value over 160 trials.

### 3.3 Soliton control using a phase-modulated pump laser

In addition to enabling deterministic generation of single solitons, phase modulation of the pump laser also facilitates timing and repetition-rate control of the resulting pulse train. We characterize this control by measuring the repetition rate of the soliton pulse train as the phase-modulation frequency is varied. This measurement is conducted as follows: First, we photodetect the pulse train after removing the central spectral lines corresponding to the phase-modulated pump laser using an optical band-reject filter. Then, in order to obtain a measurement trace of the repetition rate as a function of time, the photodetected signal is mixed with a local oscillator to reduce the

signal frequency to  $\sim 1$  MHz, after which a spectrogram of the resulting waveform is calculated.

Fig. 3.6 shows the measured repetition rate  $f_{rep}$  as  $f_{PM}$  is swept sinusoidally through a range of  $\pm 50$  kHz around the soliton's natural repetition rate; the repetition rate follows the PM except for glitches near the peaks of the sweep when  $f_{PM} - f_{rep}$  exceeds a locking bandwidth of about  $\pm 40$  kHz. This observation is consistent with an estimate of the locking range  $\delta_{PM} \times D_2/2\pi \sim 44$  kHz that is presented in Ref. [90], where we have used the approximate value  $D_2 = 14$  kHz/mode ( $\beta_2 = -2D_2/\Delta\omega_{tot} = -0.0187$ , via  $\Delta\nu \sim 1.5$  MHz). In the inset of Fig. 3.6 we overlay the results of LLE simulations that qualitatively match the observed behavior. These simulations are conducted by introducing the term  $+\beta_1 \frac{\partial\psi}{\partial\theta}$  to the right-hand side of Eq. 3.1, where  $\beta_1 = -2(f_{FSR} - f_{PM})/\Delta\nu$  incorporates a difference between the modulation frequency and the FSR of the resonator into the model;  $\beta_1$  may be varied in time to simulate the sweep of  $f_{PM}$ . These simulations indicate that the periodic nature of the glitches is due to the residual pulling of the phase modulation on the soliton when the latter periodically cycles through the pump's phase maximum.

To evaluate the utility of phase modulation for fast control of the soliton's properties, we measure the repetition rate of the pulse train as  $f_{PM}$  is rapidly switched by  $\pm 40$  kHz, which is within the soliton's locking range. To measure these fast dynamics, we split the photodetected repetition-rate signal and send one path through a reactive circuit element (a set of low-pass filters) that induces a frequency-dependent phase shift. By comparing the phase between the two paths as a function of time, the time-dependent repetition rate can be determined. We construct eye-diagrams out of the resulting data; these are shown in Fig. 3.7. In Fig. 3.7a,  $f_{PM}$  is switched with  $200\ \mu s$  period and  $10\ \mu s$  transition time; in Fig. 3.7b it is switched with  $100\ \mu s$  period and  $60\ ns$  transition time. These eye diagrams show that the PM enables exquisite control of the soliton pulse train.

We overlay a simulated eye diagram on the data in Fig. 3.7b. This simulation is conducted for parameters  $\Delta\nu = 1.5$  MHz,  $\delta_{PM} = 0.9\pi$  that are near the experimental values, and the agreement between measurement and simulation indicates that the measurements are consistent with fundamental LLE dynamics. Fig. 3.7c presents the results of additional LLE simulations; the basic result is that the switching speed of  $f_{rep}$  is limited by the resonator linewidth, and can be only modestly

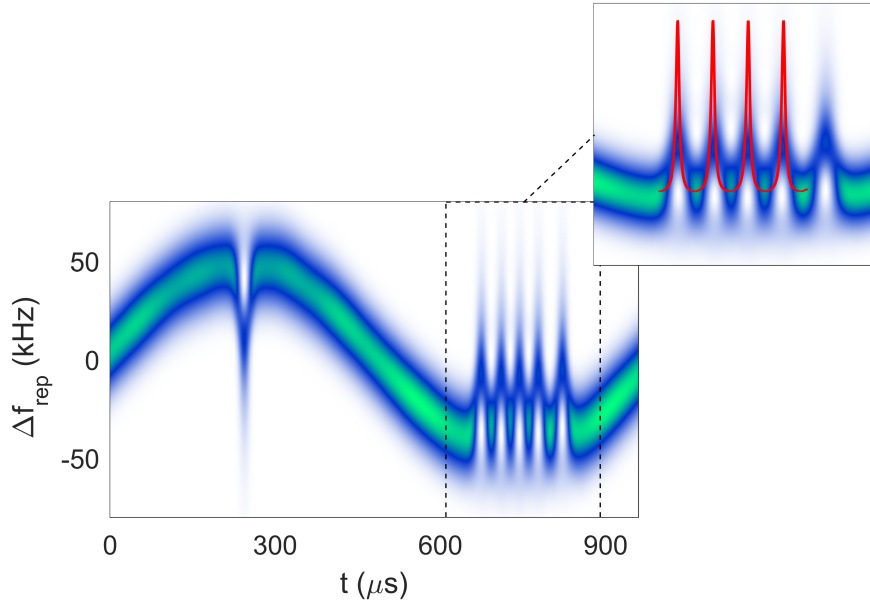


**Figure 3.6: Repetition-rate control using a phase-modulated pump laser.** Spectrogram of the measured repetition rate of the soliton pulse train generated by a phase-modulated pump laser as the frequency of phase modulation is swept through  $\pm 50$  kHz over 1 ms. Glitches in the spectrogram indicate that the range over which  $f_{rep}$  can be locked to  $f_{PM}$  has been exceeded. Inset: Qualitative agreement with simulations when  $f_{PM}$  is outside of the locking bandwidth, shown in red. As the soliton and the pump phase evolve at different frequencies  $f_{rep}$  and  $f_{PM}$ , the soliton periodically approaches the maximum of the phase profile. The soliton's group velocity changes, nearly locking to the phase modulation, before becoming clearly unlocked again.

improved by increasing  $\delta_{PM}$ .

### 3.4 Subharmonic phase modulation for high repetition-rate systems

One apparent barrier to the use of a phase-modulated pump laser for single-soliton generation and manipulation is the electronically-inaccessible FSRs of some typical microcomb resonators. However, it is possible to overcome this challenge by phase modulating at a subharmonic of the FSR. Simulations indicate that PM can directly excite single solitons with small modulation depth, e.g.  $\delta_{PM} = 0.15\pi$ . In this limit, only the first-order PM sidebands are relevant, and their amplitude and phase relative to the carrier control the dynamics. For a small desired modulation depth defined by the relationship between the first-order sidebands and the carrier, it is possible to modulate at a frequency  $f_{PM} \sim f_{FSR}/N$  so that the  $N^{\text{th}}$ -order PM sidebands and the carrier address resonator

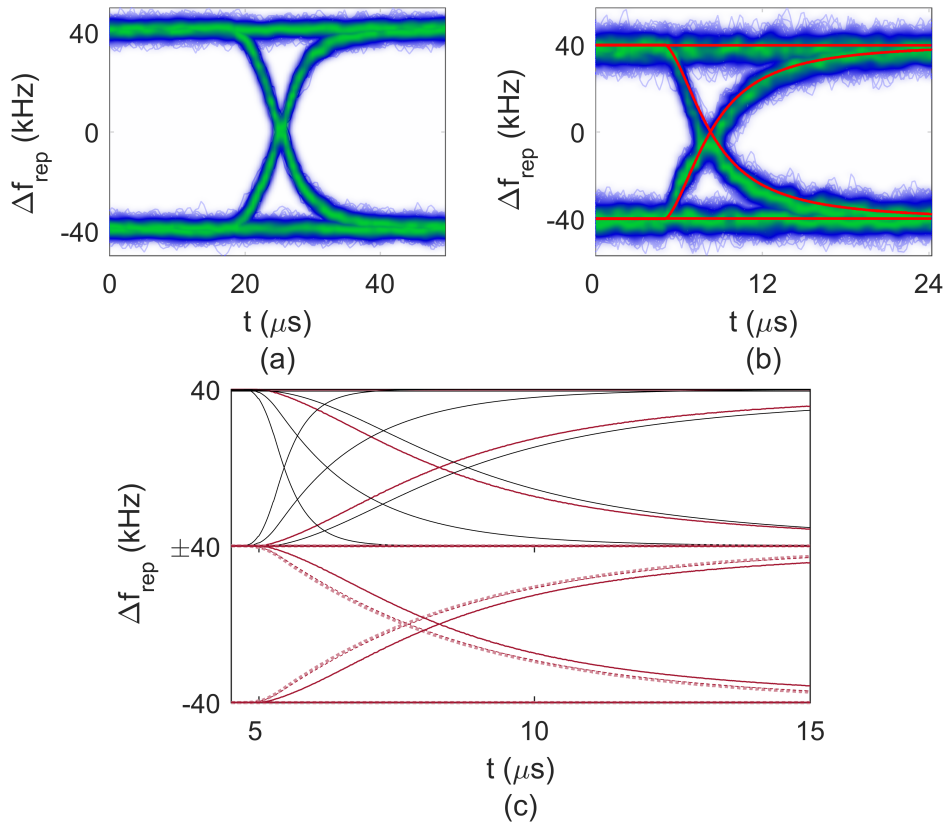


**Figure 3.7: Repetition-rate switching driven by a phase-modulated pump laser.** (a) Measured eye-diagram showing the switching capability of the soliton pulse train's repetition rate as  $f_{PM}$  is switched over  $\pm 40$  kHz with  $10 \mu\text{s}$  transition time. (b) The same with  $60$  ns transition time, with an LLE simulation of the dynamics (red) overlaid. The simulation parameters are  $\delta_{PM} = 0.9\pi$ ,  $\Delta\nu = 1.5$  MHz. (c) Simulated switching dynamics for various linewidths and modulation depths. Top:  $\Delta\nu=10$  MHz (fastest, left), 3 MHz, and 1.4 MHz (traces shown in solid black). Bottom: depths of  $2\pi$  and  $6\pi$  (dashed red, curves nearly overlap). In each, the other parameter matches the simulation in (c), which is shown again in solid red.

modes with relative mode numbers -1, 0, and 1. The depth of modulation at the frequency  $f_{PM}$  can be chosen to fix the amplitudes of the  $N^{\text{th}}$ -order PM sidebands relative to the carrier and target a desired effective modulation depth. It is worth noting that when  $N$  is odd, phase modulation is recovered when the sidebands of order  $-N$ , 0, and  $N$  address resonator modes -1, 0, and 1. When  $N$  is even the result is pure amplitude modulation, such that the driving term takes the form  $F(1 + A \cos \theta)$ . Simulations indicate that this AM profile also enables spontaneous single-soliton generation under some circumstances, but we note that this modulation profile cannot be obtained from a standard Mach-Zehnder modulator, which provides a drive like  $F \cos(\eta + \delta \cos \theta)$ ; AM in gen-

eral may be less useful than PM because schemes of comparable complexity do not always provide robust trapping of solitons to the same point in the co-moving frame at which they are generated.

Fig. 3.8 presents an example of this technique. We simulate spontaneous soliton generation with PM at  $f_{PM} = f_{rep}/N = f_{rep}/21$ . The effective modulation depth is  $0.15\pi$ , which requires real modulation depth at the frequency  $f_{PM}$  with depth  $\delta_{PM} \sim 8.3\pi$ . Because the phase modulation spreads the optical power into the PM sidebands, use of this technique requires higher optical power for the same effective pumping strength; in this example the optical power must be increased by  $\sim 15.6$  dB. A smaller real modulation depth could have been chosen to recover effective depth of  $\delta_{eff} = 0.15\pi$ , but our chosen depth of  $\sim 8.3\pi$  gives better efficiency due to the higher ratio of the power in modes  $0, \pm 21$  to the total power in the spectrum. While the required modulation depth and pump power are higher with subharmonic phase modulation, neither is impractical. This technique could be used for spontaneous single-soliton generation in high-repetition rate systems; the example above indicates that it could be immediately applied in a 630 GHz-FSR resonator with 30 GHz phase modulation.

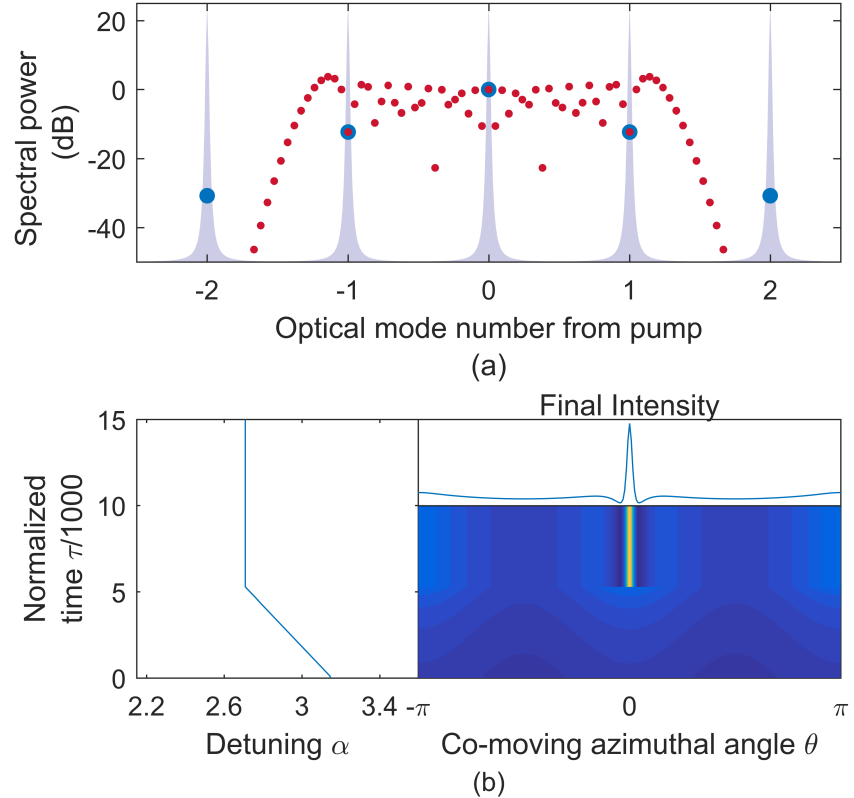


**Figure 3.8: Subharmonic phase modulation for high-repetition-rate soliton generation.** (a) Spectra of PM at  $f_{FSR}$  with depth  $0.15\pi$  (blue) and at  $f_{FSR}/21$  with depth  $\sim 8.3\pi$  (red). The relationships between the fields that address resonator mode numbers  $-1$ ,  $0$ , and  $1$  (as indicated by the gray Lorentzian curves) are the same in both cases. (b) LLE simulation of single-soliton generation using the subharmonic phase-modulation spectrum shown in red in panel (a). Only modes  $n = 0, \pm 21, \pm 42, \dots$  of the phase-modulated driving field are coupled into the resonator and affect the LLE dynamics, with modes  $|n| > 21$  having negligible power. As  $\alpha$  is increased from a large initial value, a soliton is spontaneously generated, exactly as in the case of phase modulation near the FSR.

## Chapter 4

### Soliton crystals in microresonators

This chapter describes work that was reported in:

- Daniel C. Cole, Erin S. Lamb, Pascal Del'Haye, Scott A. Diddams, and Scott B. Papp. Soliton crystals in Kerr resonators. *Nature Photonics* **11** (2017), 671–676.

This chapter presents results on the self-organization of ensembles of solitons in optical microring resonators. These results involve physics beyond the basic LLE model for Kerr-comb formation, as is described in Sec. 4.3. These experiments are performed using laser-machined silica microrod resonators [31] and chemically-etched microdisk [29] resonators with  $\sim$ 25 GHz and  $\sim$ 16.5 GHz FSR, respectively; but the physical mechanism for the self-organization that we describe applies to any resonator that supports multiple transverse modes. We refer to these self-organized soliton ensembles as ‘soliton crystals,’ which extends an analogy to condensed-matter physics that has been made in other nonlinear-optical systems, including single-pass nonlinear fiber systems [100] and harmonically mode-locked fiber lasers [101, 102], where a different mechanism for soliton crystallization that is based on two distinct timescales of the laser medium was identified [103]. It is interesting to note that the spatiotemporal chaos exhibited by Kerr combs was referred to as a ‘soliton gas’ in early studies of nonlinear dynamics in passive fiber-loop resonators [104–106]. This work represents an important step towards building a complete understanding of the nonlinear dynamics involved in generation of Kerr combs, and in particular represents a deepening of our understanding of some previously-published and heretofore unexplained experimental results [107, 108].

## 4.1 Spectral and temporal characteristics of soliton crystals

Soliton crystals in Kerr resonators are soliton ensembles in which each soliton lies on a lattice site  $\theta_n = 2\pi n/N$  in the azimuthal co-moving frame, where  $N$  is a lattice parameter that arises from the fundamental physics of the system as described below and  $n$  indexes over the lattice sites. In the soliton crystals presented below there are many more available lattice sites than solitons, so that a fraction of the lattice sites are occupied. In the frequency domain, the temporal ordering of pulses in a soliton crystal corresponds to a highly modulated optical spectrum that exhibits distinctive features.

We present plots illustrating the spectral and temporal characteristics of an example soliton crystal in Fig. 4.1. Fig. 4.1a shows an experimental measurement of a soliton crystal spectrum. This spectrum exhibits prominent comb modes similar to primary-comb lines, and underlying these primary-comb lines are single-FSR-spaced spectral lobes. We can understand this spectrum through the basic superposition principle of the electric field: The primary comb spectrum with spacing  $N \times f_{FSR}$  corresponds to a train of  $N$  uniformly spaced pulses in the resonator; here  $N = 24$ . To this pulse train we add an *out-of-phase* pulse  $S_-$  that coincides in time with one of the existing pulses—in the time domain this corresponds to the introduction of a vacancy into the pulse train, while in the frequency domain this corresponds to the addition (in the phase-sensitive field quantity) of the primary-comb spectrum and the spectrum of the single, out-of-phase soliton. We then add a second soliton  $S_+$  to the pulse train, this one *in phase* with the existing pulses and slightly temporally shifted from the vacancy. The time-domain result is a pulse train with one pulse displaced from its expected position based on uniform spacing. In the frequency domain, the positions of the pulses  $S_+$  and  $S_-$  correspond to different linear spectral phase shifts on each of their individual spectra; when these spectra are added together the result is spectral interference that is periodic in frequency. This gives rise to the lobes beneath the primary-comb lines; the frequency period of the interference is inversely proportional to the separation between the pulses  $S_+$  and  $S_-$  in time.

We illustrate this principle by plotting pulse trains exhibiting a shifted pulse in Fig. 4.1b, and

show their calculated spectra in Fig. 4.1a. These pulse trains are constructed using the analytical approximation to soliton ensembles provided by Eq. 2.28. The pulse train shown in orange is composed of solitons pinned to sites on a lattice, and the pulse train shown in blue is obtained from this first pulse train by introducing a small random displacement to the position of each pulse. The effect of this small position jitter is apparent in the calculated spectra in Fig. 4.1a—the highly-distinctive spectral characteristics of the soliton crystal are eroded. In fact, it is a general property of the soliton-crystal spectra that we present in this chapter that the contrast and definition of the distinctive spectral characteristics depends on the high precision with which the pulses fall on the lattice sites.

## 4.2 Soliton crystal generation

Soliton crystals are characterized by stable, dense occupation of the resonator by soliton pulses, and this dense occupation comes with high circulating power relative to single solitons or few-soliton ensembles. This important fact allows soliton crystals to be generated with decreasing pump-laser frequency scans across the resonance that are adiabatic—slow enough that both the resonator temperature and the state of the comb  $\psi$  are maintained at values<sup>1</sup> that correspond to the instantaneous  $\alpha$  and  $F^2$  parameters throughout the scan. We demonstrate generation of a soliton crystal in a slow scan in Fig. 4.2; it is interesting to contrast the continuity of the taper-transmission trace with the staircase-like nature of the same measurement exhibited in the generation of a few-soliton ensemble (see e.g. Ref. [54] and the discussion in Chap. 2). Slower scans than the one presented in Fig. 4.2 are possible, and in fact we have generated soliton crystals by tuning the pump-laser frequency arbitrarily slowly by hand.

## 4.3 Mechanism of soliton crystallization

The time-domain waveforms we have considered so far are not stable in evolution under the LLE. For each, the observed width of the spectrum fixes the ratio between  $\alpha$  and  $\beta$ , as seen from

---

<sup>1</sup> This terminology is a bit imprecise when applied to chaotic Kerr-combs that evolve with time; in this case the chaos exhibits the same behavior at each point in the scan that would be expected if  $\alpha$  and  $F^2$  were held fixed.

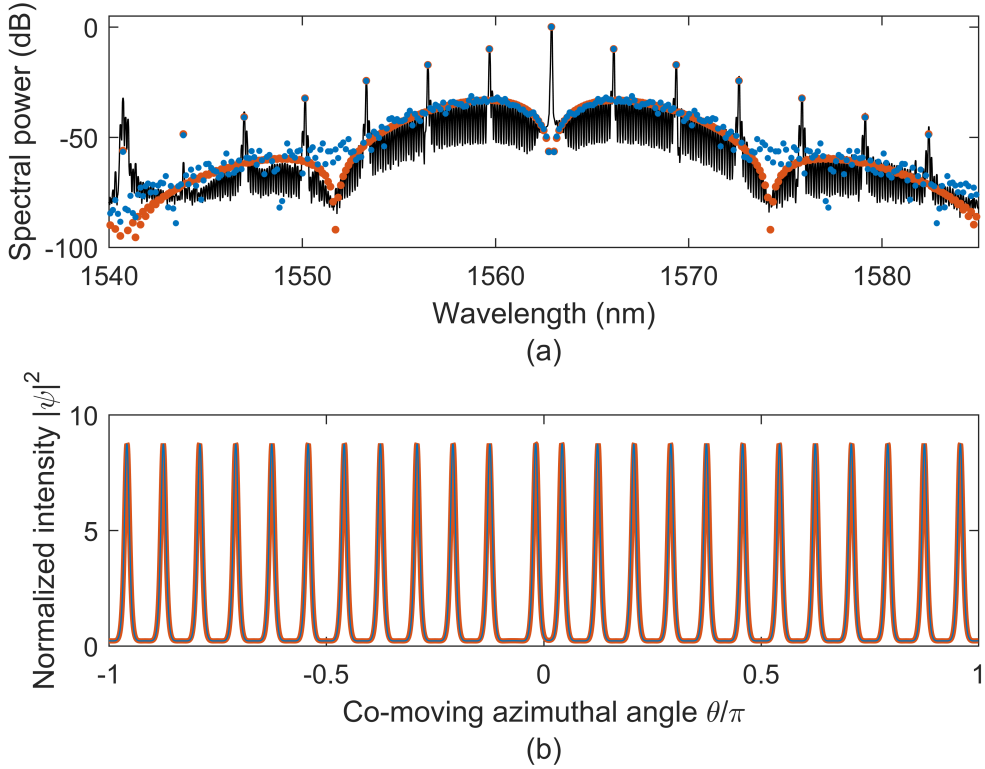


**Figure 4.1: Spectral contrast of a soliton crystal.** (a) Experimental measurement of a soliton-crystal spectrum (black), along with two approximations to the crystal's time-domain waveform as a soliton ensemble, according to Eq. 2.28. Shown in orange is the spectrum of an ensemble of solitons pinned to sites on a lattice with spacing  $2\pi/(7 \times 24)$ ; here the majority of the pulses are separated from their neighbors by seven lattice sites, but one pulse is displaced by two lattice sites from its expected position. Shown in blue is a calculation of the spectrum that results when random (uniformly distributed) jitter is imposed on the same pulse positions; the range of the jitter is  $\pm 3\%$  of the typical inter-soliton spacing  $2\pi/24$ . (b) Time-domain traces corresponding to the spectra shown in (a). There is no readily apparent difference between the positions of the pulses in two pulse trains because the magnitude of the imposed jitter is small; nevertheless the definition of the distinctive spectral features is eroded by the jitter.

Eq. 2.27. This ratio then fixes the temporal duration of the solitons, in turn determining the characteristic length of their interactions. When an attempt to simulate the crystal according to the LLE is made with parameters that give agreement with the measured width of the optical spectrum (e.g.  $F^2=3.7$ ,  $\alpha = 3.77$ , and  $\beta = -0.0054$  for the crystal in Fig. 4.2c and d), it is found that pair-wise attractive interactions between solitons lead to collapse of the crystal, as shown below in Fig. 4.3.

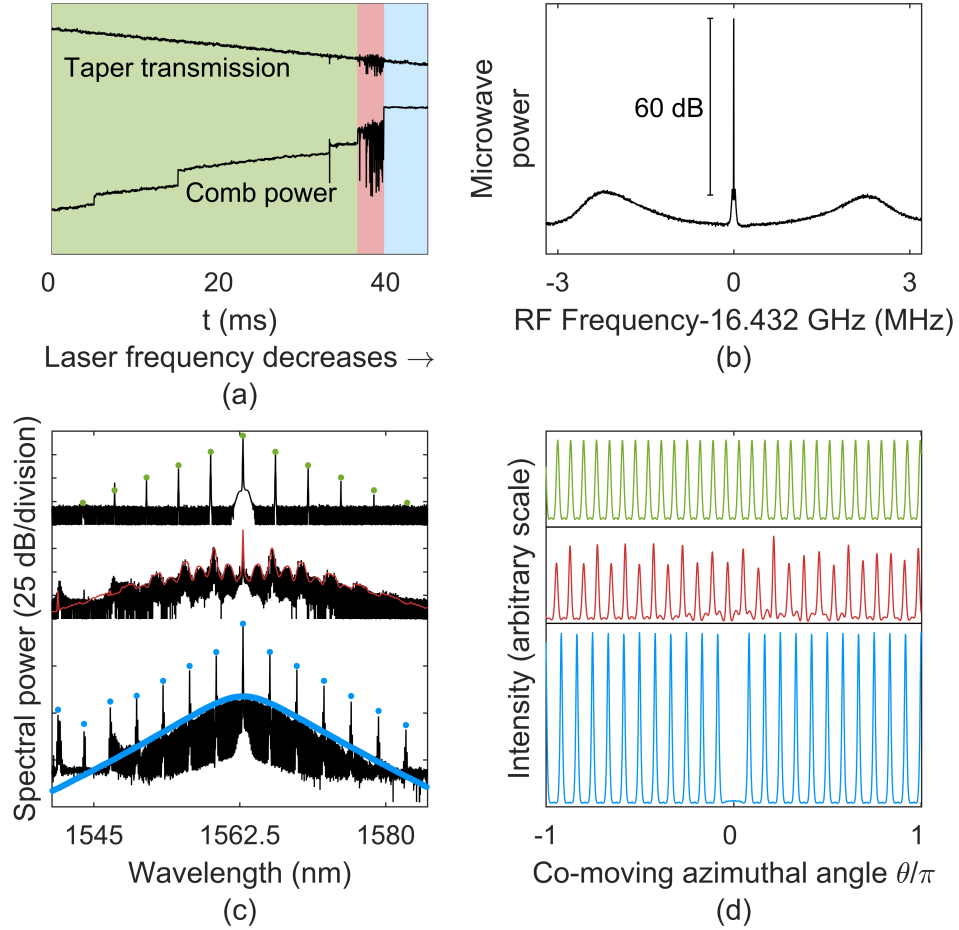


**Figure 4.2: Generation and characterization of a soliton crystal.** (a) Measurements of the power transmitted past the resonator ('Taper transmission') and this power with the pump frequency filtered out ('Comb power') during crystal generation with a scan that proceeds through primary-comb (green), chaotic (red), and soliton crystal (blue) regimes. The resonator's thermal response leads to the non-Lorentzian taper transmission profile, and the continuity of the taper transmission trace upon soliton crystal condensation indicates that the intracavity power of the soliton crystal is matched to the chaos that precedes it. (b) Narrow measured RF beat for the repetition rate of the soliton crystal is indicative of a coherent comb, in contrast with the chaotic state. (c) Progression of the optical spectrum through the scan, with experimental data (black) obtained by halting the scan at the appropriate point, and LLE simulations (with a perturbation as described in Sec. 4.3) in color. The simulated spectrum for the chaotic state shown in red is a time average. (d) Simulated time-domain traces corresponding to the simulated spectra in (c). The simulated intensity for the chaotic state is a snapshot. The soliton crystal shown in blue is a uniform pulse train with a single vacancy (see text).

A stabilization mechanism that goes beyond the physics of the LLE is responsible for the stability of soliton crystals. The stabilization mechanism for the crystals we present here arises from avoided mode crossings in the resonator spectrum. As discussed in Sec. 2.1, the resonators used in

these experiments support multiple families of circulating modes, each with its own transverse spatial intensity profile and free spectral range. Although the modes in different families are in principle orthogonal, coupling between them can be provided by perturbations, for example by the coupling waveguide or tapered fiber used to drive the resonator, or anomalies in the resonator fabrication that break the resonator symmetry. When a coupling exists between modes that are sufficiently close in frequency, the modes become hybridized and their frequencies become displaced [109]. The effect of this coupling and the associated perturbation to the resonator mode spectrum on Kerr-comb generation has been investigated [110], and it has been found that avoided mode crossings can inhibit soliton generation in anomalous-dispersion resonators [30, 111], while they can facilitate the formation of Kerr-combs in normal-dispersion resonators [112–114].

Here we are interested specifically in the impact of an avoided mode crossing on the temporal waveform of a soliton. For simplicity, we make the approximation that a single mode of the Kerr comb with number  $\mu_x$  is affected by the mode crossing. This approximation neglects the fact that avoided mode crossings between two families typically span a range of modes as the mode frequencies traverse each other in frequency space due to a small fractional difference between the free-spectral ranges of the two mode families; this can be observed in many of the experimental spectra presented in this chapter. However, we find that the single-mode assumption is generally sufficient for modeling the stability of the soliton crystals that we observe.

The perturbation of the frequency of a resonator mode  $\mu_x$  that is far from the pumped mode  $\mu = 0$  affects the local detuning of the comb from the resonator. When this local comb-resonator detuning is decreased, the efficiency of nonlinear frequency conversion to mode  $\mu_x$  can be increased. This increases the amplitude of mode  $\mu_x$  in the soliton's spectrum, and the resulting change to the time-domain waveform can be understood by considering this increase as the addition of extra CW light at the frequency of mode  $\mu_x$ . This extra CW light leads to the introduction of periodic intensity oscillations in the background on which the soliton rides as it beats against the existing background at the pump frequency. The new background wave in the cavity has a period of  $2\pi/\mu_x$  in the angular coordinate  $\theta$ .

When several of these perturbed solitons co-propagate in a resonator, they interact through their extended waves and arrange themselves such that the waves constructively interfere [83]. Each soliton then lies at the peak of a single extended background wave in the resonator, similar to predictions for bichromatically pumped Kerr combs [115]. Importantly, temporal separations between solitons are therefore required to be multiples of this wave's period, and the wave stabilizes the crystal against the attractive interactions discussed above. Furthermore, the wave's amplitude, and thus the strength of the crystal against perturbations, increases with the number of co-propagating perturbed solitons. Within the assumption of single-mode perturbation of the comb's spectrum, this interaction has infinite range.

We note that the mechanism observed here builds on previous reports of related phenomena. It has been shown that local interactions between cavity solitons can arise through decaying oscillatory tails [116], leading to the formation of small, locally ordered soliton molecules; this effect appears to be significant in Kerr ring resonators only at small detunings [82]. Additionally, it has been shown that the injection of a second CW laser into a passive fiber-ring resonator can result in the generation of uniform distributions of solitons [117]. The mechanism we report here can be viewed as a variant of this CW-soliton interaction in which the ‘injected’ CW laser is provided by the solitons themselves through the affect of the mode crossing on the solitons' spectra.

We connect this discussion to the soliton-crystal spectrum presented in the bottom trace of Fig. 4.2c—this spectrum exhibits excess power near pump-referenced modes numbers  $\mu_{\times,1} = 5 \times 24 = 120$  (1547 nm) and  $\mu_{\times,2} = 7 \times 24 = 168$  (1541 nm), where 24 FSR is the spacing of the prominent primary-comb lines. Also visible is suppressed comb generation where the comb-resonator detuning has been increased.

#### 4.3.1 Simulation of soliton crystals

To incorporate the stabilization mechanism described above into numerical simulations, we insert into the LLE a reduced comb-resonator detuning on a single mode  $\mu_{\times}$ . The mode-dependent

comb-resonator detuning can be calculated as:

$$\alpha_\mu = -2(\omega_p + \omega_\mu - D_1)/\Delta\omega_{tot}, \quad (4.1)$$

$$= \alpha - \beta\mu^2/2. \quad (4.2)$$

Here  $\omega_p$  is the frequency of the pump laser,  $\omega_\mu$  is the set of cavity resonance frequencies referenced to the pumped mode, and  $D_1 = \partial\omega_\mu/\partial\mu|_{\mu=0}$  is the resonator's FSR at the pumped mode and is also assumed to be the comb's repetition rate. The dispersion operator is applied in the frequency domain in numerical simulations of the LLE (see B), which facilitates inclusion of  $\delta$ -function perturbations to the comb-resonator detuning as:

$$\alpha_\mu = \alpha - \beta\mu^2/2 + \Delta\alpha_\mu, \quad (4.3)$$

where

$$\Delta\alpha_\mu = 2(\omega_\mu - \omega_{\mu,0})/\Delta\omega_{tot} \quad (4.4)$$

is the normalized change in the frequency of mode  $\mu$  from the expected frequency  $\omega_{\mu,0}$ .

We demonstrate the stabilization mechanism and the simulation method by presenting a simulation of the crystal in Fig. 4.2c. The simulation is shown in Fig. 4.3. This figure illustrates both the rapid timescale over which the stabilization mechanism acts and the instability of the crystal in the absence of the stabilization mechanism. To explain the stability of this 23-soliton crystal and the apparently exact circumferential spacing of the pulses by  $2\pi/24$  radians, it is sufficient to incorporate into the LLE a reduced comb-resonator detuning on only mode 120 or on mode 168, where the excess power is largest. The crystal is then a steady-state solution of the resulting perturbed LLE.

#### 4.4 Case study: pair distribution function for a superstructured crystal

We consider a third specific example of a soliton crystal. The measured and simulated optical spectra for this crystal are shown in Fig. 4.4a. This crystal exhibits superstructure—the soliton pulse train is nearly periodic in a small unit cell but is modulated with a larger periodicity. This

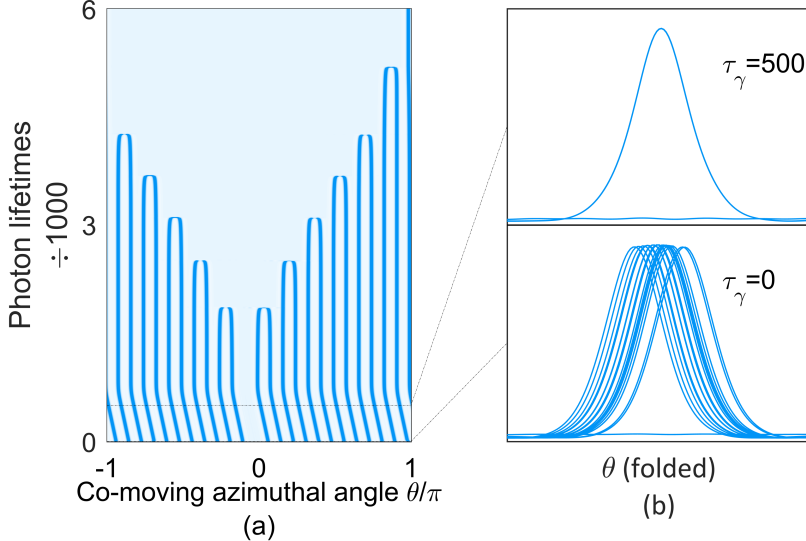


**Figure 4.3: Stabilization and collapse of a soliton crystal.** (a) Simulated evolution of the pulse train corresponding to the experimental crystal spectrum shown in Fig. 4.2c, starting from irregular pulse positions. For the first 500 photon lifetimes of the simulation, the propagation is governed by a perturbed LLE including reduced comb-resonator detuning on modes  $\mu_{\times,1} = 120$  and  $\mu_{\times,2} = 168$ . The soliton ensemble crystallizes within 10 seconds of initialization of the simulation, and then drifts within the co-rotating frame because the additional CW light on modes  $\mu_{\times,1}$  and  $\mu_{\times,2}$  corresponds to traveling waves. The reduced comb-resonator detuning is removed smoothly from 500 to 1000 photon lifetimes, resulting in the destabilization of the crystal and pair-wise annihilation of the solitons. (b) Intracavity power with the azimuthal coordinate folded modulo  $2\pi/24$ , demonstrating the initial irregularity of the pulse positions and the crystallized pulse train after 500 photon lifetimes.

results from the frustrated uniform distribution of 16 solitons with allowed inter-soliton separations of  $2\pi n/49$  radians; one pair is spaced by  $4 \times 2\pi/49$  instead of  $3 \times 2\pi/49$  radians. Excess power is apparent in the spectrum at mode  $\mu_{\times} = 49$  (highlighted by the red circle in the plot), and we simulate this crystal phenomenologically by reducing the comb-resonator detuning on mode 49 so that the observed and simulated amplitudes of this mode agree. The total background wave that emerges as the sum of the waves from each constituent soliton, is visible in the plots of the simulated intensity in Fig. 4.4b and c.

To gain insight into crystal generation, we simulate laser frequency scans across the resonance that generate this crystal in the presence of the mode crossing on mode 49. Example scans are shown for the case without the mode crossing (green) and with it (blue) in Fig. 4.5. In both scans, solitons emerge from chaos as the frequency of the laser is decreased. In the presence of the mode crossing,

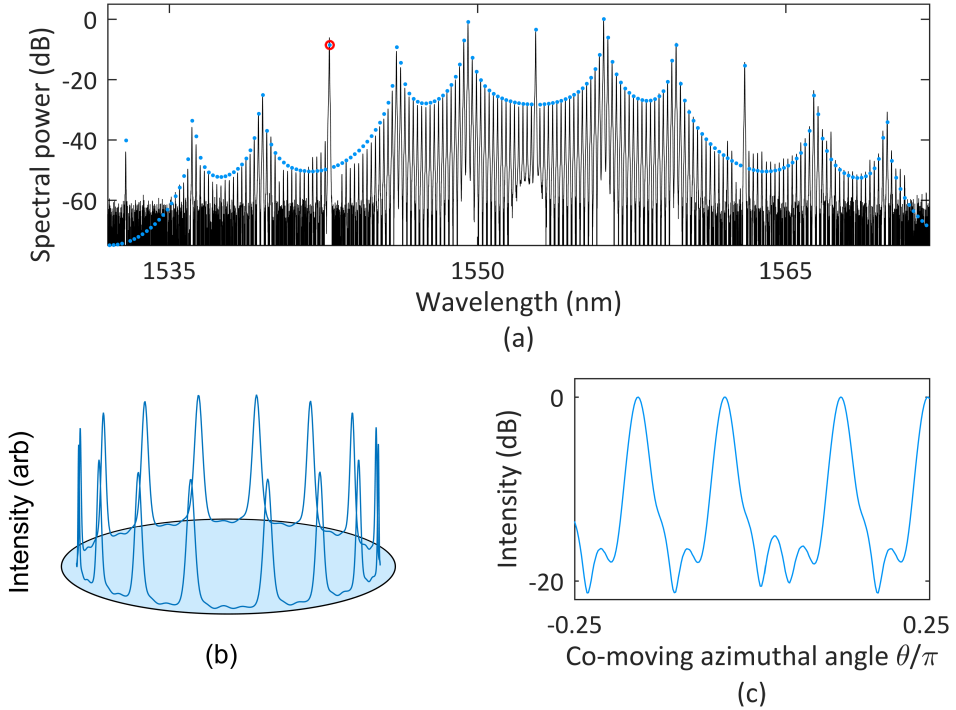


**Figure 4.4: Spectrum and waveform of a superstructured soliton crystal.** (a) Experimental (black) and simulated (blue) optical spectra of a superstructured crystal, with the red dot indicating the mode affected by a mode crossing as described in the text. (b) Simulated time-domain intensity of frustrated-uniform distribution of 16 solitons over 49 lattice points. (c) Zoomed-in logarithm-scale plot of the same that clearly shows unoccupied lattice sites and the anomalous  $4 \times 2\pi/49$  spacing between a pair of pulses.

they are generated with inter-soliton separations of  $2\pi n/49$  radians. A greater number of solitons emerge from chaos in the presence of the mode crossing, and this is consistent with the observed thermal stability of crystal generation in the experiment. Upon continuation of the simulation, some of the solitons in the scan without the mode crossing interact attractively and pair-annihilate, while the crystallized ensemble resulting from the scan with the mode crossing remains stable indefinitely.

We investigate the pair distribution function (PDF) for the soliton ensembles generated by these scans. The PDF is the probability that a soliton exists at position  $\theta_0 + \Delta\theta$  given that a different soliton exists at position  $\theta_0$ , normalized to the density. This is a useful metric to classify particle interactions that we borrow from condensed matter physics (see e.g. Ref. [118], especially Fig. 2, and Ref. [119], especially Fig. 1.1 and Chapter 3). We note that for numerically calculated discrete

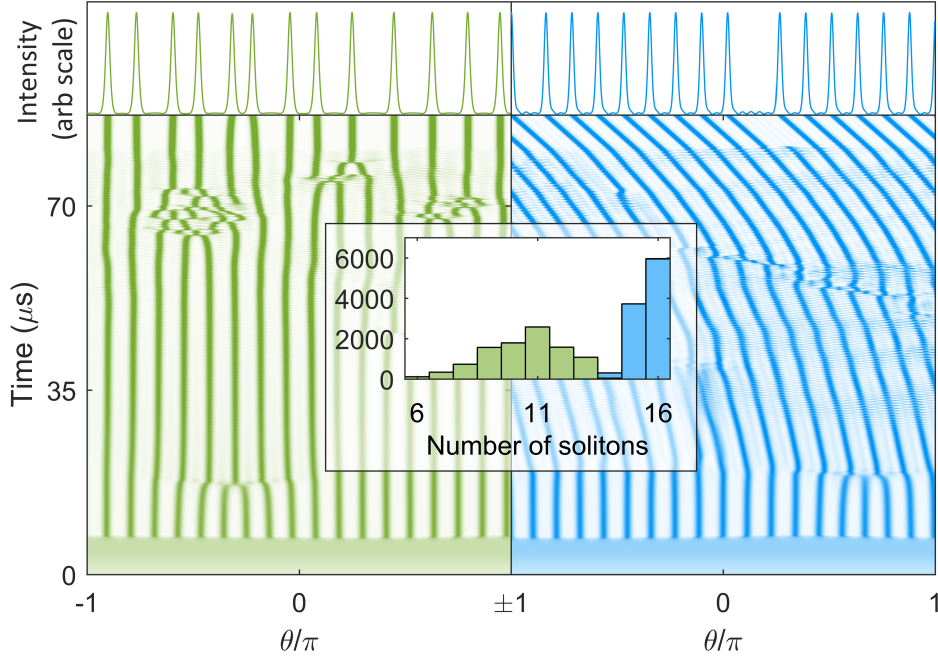
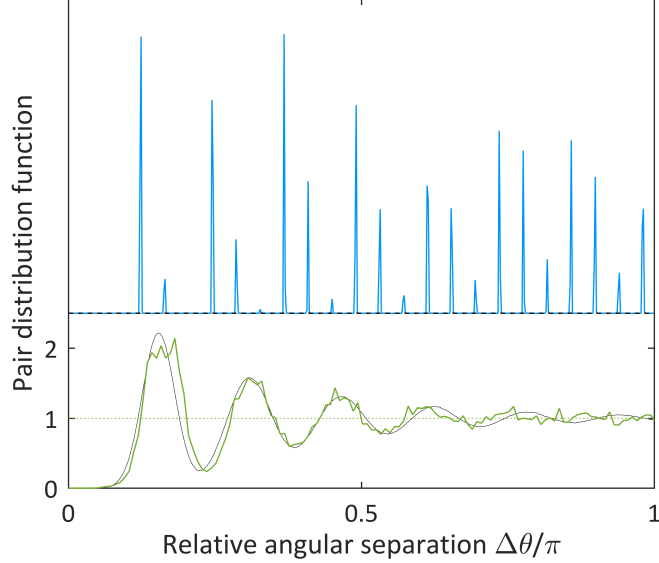


Figure 4.5: **Simulated generation of a superstructured soliton crystal.** Bottom: plots of the intracavity power during a simulated scan across the resonance, without (green) and with (blue) a mode crossing on mode 49 that reduces the comb-resonator detuning and increases the efficiency of frequency conversion on that mode. Top: final waveforms. Inset: histogram of the number of solitons generated in 10,000 simulated scans.

PDFs the absolute scaling of the PDF is not important, as it depends on the density of numerical sampling. In Fig. 4.6, we plot the average PDFs for 10000 simulated scans with and without the mode crossing. The result for the case with a mode crossing is sharply peaked, indicating that the allowed inter-soliton separations take on discrete values. The result for the case without the mode crossing is continuous, with a peak near the most likely nearest-neighbour separation and periodic revivals at its multiples, falling to the value of the PDF for uncorrelated soliton positions (the density) at large separations. This is exactly the expected form of the PDF for a liquid [118, 119]. For comparison, we plot a PDF (black) generated by simulation of a simple particle ensemble with mean inter-particle separation of  $\Delta\theta = 0.155\pi$  and normally distributed noise on this value with standard deviation of  $\sigma_{\delta\theta} = 0.18\Delta\theta$ . Thus, with a particle labeled by  $n = 0$  fixed at  $\theta = 0$ , the position of particle  $n$  is  $\theta_0 = n\Delta\theta + \sum_n \delta\theta_i$ , with  $\delta\theta_i$  the instantiations of the random variable

representing the noise on the pulse spacings. This simple model qualitatively matches the observed PDF for the simulations without the mode crossing.



**Figure 4.6: Pair distribution function for soliton crystal generation.** Average pair distribution functions calculated over 10,000 simulated scans across the resonance with (blue) and without (green) a mode crossing on mode 49. The width of the peaks in the discrete PDF is a single  $\Delta\theta$  bin. The expected PDF of a simple one-dimensional soliton liquid (see main text) is plotted for comparison in black.

## 4.5 Soliton crystal configuration space

We observe a rich variety of soliton crystals explained by ordering in accordance with an extended background wave as described above. Operationally, we adjust the pump laser power to provide repeatable conditions for creating particular crystals; crystals exhibiting a greater number and variety of defects occur with increased laser power, which intensifies the fluctuations in the chaos that precedes crystal generation and provides less well-ordered initial conditions. Once a crystal is generated, it is stable to small adjustments in the pump power and detuning in accordance with the range of soliton existence shown in Fig. 2.4, as the crystal structure is determined by the initial conditions for soliton formation rather than by an explicit dependence on pump power or detuning.

Our interpretation of experimental data is based first on the fact that the LLE restricts the

behavior of the field  $\psi$  to either an extended pattern (primary comb pulse train or chaos) or an ensemble of solitons. Simultaneous experimental measurement of 1. A quiet repetition-rate tone when the spectrum of the photodetected power is analyzed, and 2. Single-FSR spacing in the power spectrum indicate that a Kerr-comb is a soliton crystal<sup>2</sup>. To determine the temporal structure of a soliton crystal, we begin with the assumption that the spectrum corresponds to a soliton ensemble. Using the properties of the Fourier transform (e.g. linear superposition and the fact that a shift in time corresponds to a linear spectral phase shift), it is usually possible to deduce the configuration of pulses that must lead to the observed spectrum. Once the pulse train corresponding to the general structure of the spectrum has been deduced, the experimental spectrum can be compared to the spectrum of this pulse train calculated as an ensemble of solitons according to Eq. 2.28. This comparison reveals localized excess power in the experimental spectrum, which is evidence of a mode crossing. The strength of the mode crossing, controlled in the experiment by e.g. the taper-induced coupling between modes, is determined phenomenologically from the magnitude of the excess power and reduced comb-resonator detuning on a single mode is incorporated into a perturbed LLE as described in Sec. 4.3. It is then verified that the pulse train whose spectrum matches the experimental data is a steady-state solution to this perturbed LLE, which requires the inter-soliton separations to be multiples of the period of the beat between the excess power and the pump laser. This period is  $2\pi/\mu_x$ , where  $\mu_x$  is the mode number of the affected mode. Because this process connects the presence of excess power on a single optical mode of the Kerr-comb spectrum to the general shape of the spectrum, two observations that are not related a priori, it provides strong evidence that the time-domain waveform of the crystal has been determined correctly.

The crystals we observe exhibit vacancies (Schottky defects), dislocations (Frenkel defects), disorder, or superstructure, or some combination thereof [120]. In a disordered crystal, the solitons still occupy lattice sites whose positions are determined by an avoided mode crossing in the resonator spectrum, but their distribution over these lattice sites varies without any apparent regular order

---

<sup>2</sup> These requirements are probably sufficient, but not necessary—for example, a defect-free crystal will exhibit multi-FSR spacing. Experimentally, the difference between such a crystal and a primary-comb pulse train lies in the parameters  $\alpha$  and  $F^2$  that place the pump laser *either* in the regime for solitons or the regime for primary comb. However, these parameters are not necessarily straightforward to determine.

or favored period. In this case, it is less straightforward to determine the pulse configuration from the shape of the spectrum. Instead, to determine the pulse configuration for a disordered crystal, we first identify excess power due to a mode crossing through observation of an asymmetry in the spectrum about the pump. The location of the excess power then fixes the allowed inter-soliton separations in the resonator, after which an exhaustive search is performed until a pulse train is found that yields the experimental spectrum.

Optical spectra for various observed and hypothetical soliton crystals are plotted in Fig. 4.7. We have simulated 13 of the experimental spectra as steady-state solutions to a perturbed LLE (this excludes crystal o); for 10 of these, the stabilizing mode crossing is visible in the data but not necessarily shown in the figure. For the other three the position of the mode crossing is inferred from the distribution of solitons and other crystal states observed in the same resonator.

We highlight the crystal plotted in Fig. 4.7n. This crystal exhibits both superstructure, with a superlattice period of  $2\pi/3$  radians, and a Frenkel defect. Three identical supercells per resonator round-trip yield a spectrum which has light in optical modes spaced by three resonator FSR, because the waveform's period has been reduced threefold. The Frenkel defect, occurring once per round-trip, transfers a pulse from one supercell to another and contributes the single-FSR lobes to the spectrum. The result is three bursts of pulses containing 8, 9, and 10 solitons respectively.

Fig. 4.7o shows a soliton crystal with inter-soliton separations that are slightly irregular and that we have not simulated as a steady-state solution of any perturbed LLE. We expect that the formation of the crystal and the distribution of solitons are dictated by mode interactions, but that in this case our simple approximation of a perturbation to the LLE by a reduced comb-resonator detuning on a single comb mode is not appropriate.

Finally, we highlight the series of crystals plotted in Figs. 4.7p-4.7t. This series of crystals was generated by moving the pump laser closer to a mode-crossing in steps of integer multiples of the resonator FSR. This data demonstrates the influence of the background beating between the pump laser and the mode crossing in determining the configuration of solitons in the resonator.

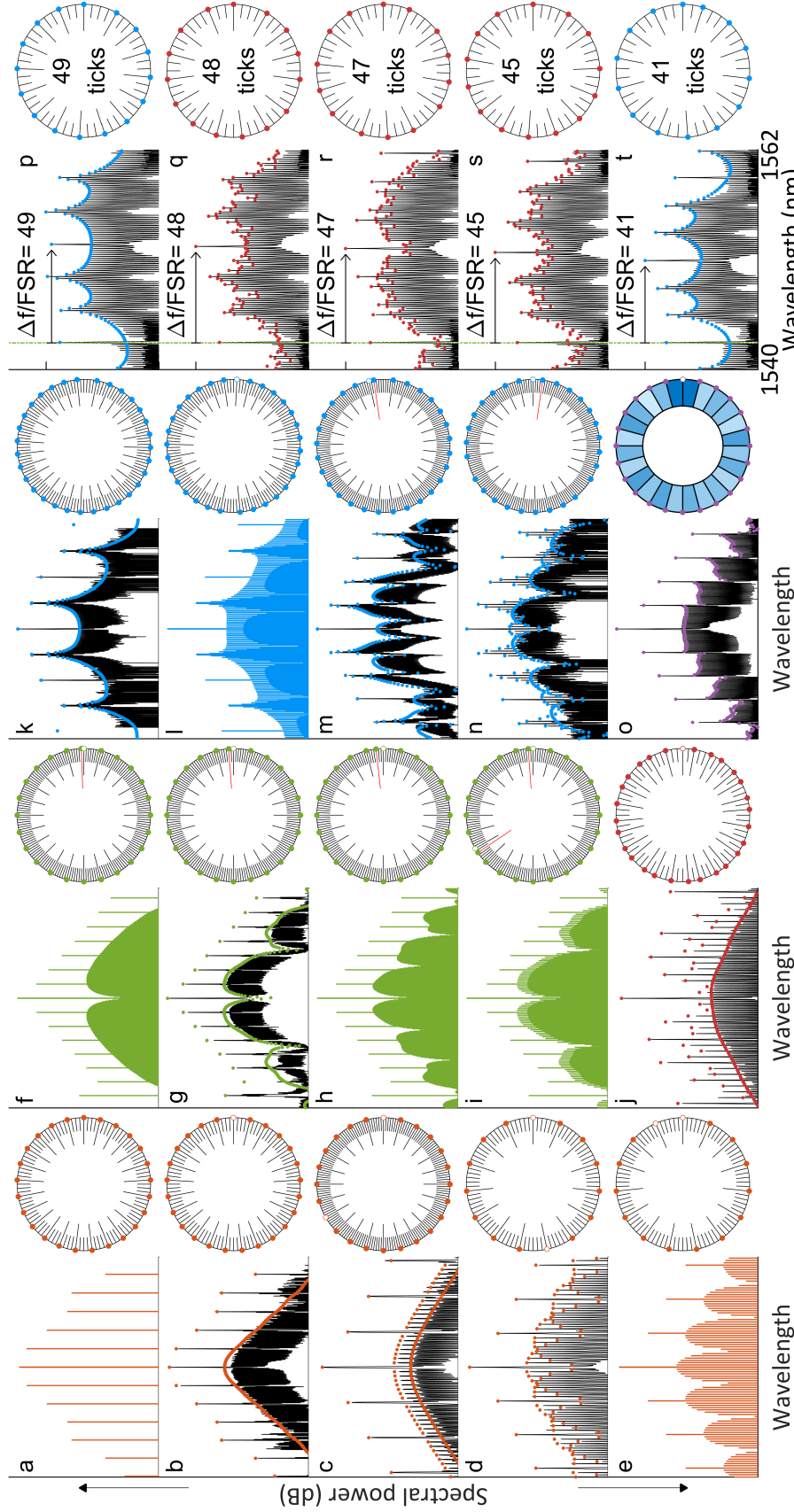


**Figure 4.7: Taxonomy of soliton crystals.** Measured optical spectra are shown in black, with simulations in color. Schematic depictions of the soliton distribution in the resonator co-moving frame are shown to the right of each spectrum. Major ticks in the schematic diagrams indicate the location or expected location of a soliton. Minor ticks indicate lattice sites, corresponding to peaks of the extended background wave due to a mode crossing. (a) A perfect soliton crystal, consisting of 25 uniformly-distributed solitons. (b-e) Soliton crystals exhibiting vacancies. (f-i) Soliton crystals exhibiting Frenkel defects. Shifted solitons still occupy a lattice site. (j) A disordered crystal. (k-n) Crystals exhibiting superstructure. (o) A crystal with irregular inter-soliton spacings. Darker shading indicates a smaller inter-soliton spacing. The range in inter-soliton spacings is 3 % of the mean. (p-t) A series of crystals generated as the pump laser is moved progressively closer to the stabilizing mode crossing.

## 4.6 Time-domain measurements of soliton crystals

It is recognized in ultrafast optics that it is not generally possible to infer the time-domain waveform of an optical signal from its optical power spectrum without additional information [121], because the spectrum contains no phase information. The LLE imposes restrictions on the possible time-domain field behaviors that can be exhibited, which can allow educated guesses to be made about the time-domain field based on the recorded optical spectrum, and we have been successful in modeling the observed spectra presented above as soliton ensembles. However, it is useful to confirm the LLE-assisted interpretation of experimental data both to strengthen the case for the LLE as a useful model for the system and to stay alert to the possibility of extra-LLE phenomena.

To verify our time-domain interpretation of the spectra we record in experiment, we characterize the temporal intensity of soliton crystals using an optical cross-correlation measurement. A depiction of the approach and the results for measurement of the time-domain intensity of the crystal shown in Fig. 4.7j is shown in Fig. 4.8. We send the Kerr-comb output and an optical reference pulse train through a LiIO<sub>3</sub> crystal with a relative angle of 90° between the beams. When the beams overlap in the crystal an amount of light proportional to the product of their intensities, at the sum of their frequencies, is emitted in a third direction. By measuring the average power of this emitted light while scanning the relative delay between the two beams, we measure the intensity cross-correlation between the crystal and the reference pulse.

In the limit of a  $\delta$ -function reference pulse, optical cross-correlation directly measures the time-domain waveform of an unknown signal. To approximate this limit, we perform cross-correlation measurements with a train of reference pulses that have duration comparable to that of the solitons, which allows us to precisely characterize soliton crystals. The reference pulse train is derived through electro-optic modulation (see Chapter 7) from the same laser that pumps the resonator, and the repetition rate of the reference pulse train is locked to the repetition rate of the Kerr-comb output.

We generate crystals in a through-coupled configuration, which results in interference between the out-coupled solitons and the through-coupled pump that depends on the coupling condition and

that effects the time-domain waveform that propagates away from the resonator. In this particular experiment the out-coupled solitons destructively interfere with the through-coupled pump, with the result that the solitons manifest as dips in the through-coupled intensity. To correct this, before cross-correlation we use a spatial light modulator to rotate the phase of the pump laser by  $\pi$  so that it constructively interferes with the solitons, yielding solitons riding on top of a CW background.

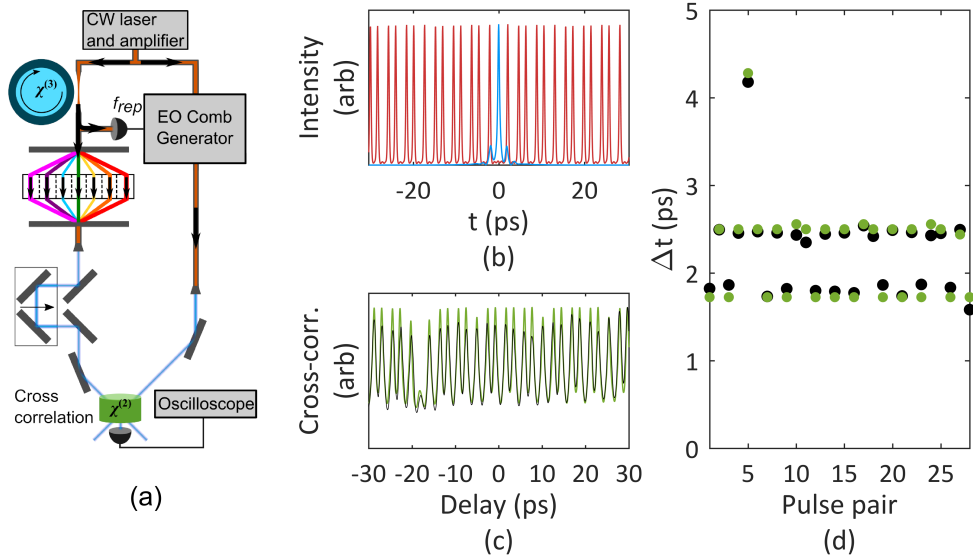


**Figure 4.8: Cross-correlation characterization of a soliton crystal.** Schematic depiction of the setup for using an electro-optic (EO) modulator comb as a reference pulse to measure the time-domain waveform of a soliton crystal. The  $\chi^{(3)}$  (Kerr) and  $\chi^{(2)}$  nonlinearities are indicated on the resonator and nonlinear crystal (LiIO<sub>3</sub>). A spatial light modulator is used to rotate the phase of the pump laser by  $\pi$  after crystal generation to compensate for interference between the out-coupled soliton crystal and the through-coupled pump light. The soliton crystal and the EO modulator comb share a pump laser, and the repetition frequency  $f_{rep}$  of the EOM comb is locked to that of the crystal. Varying the relative delay in one arm of this interferometer enables measurement of the intensity cross-correlation between the soliton crystal and the reference pulse. (b) Simulated crystal (red) and reference (blue) intensity profiles. (c) Measured (black) and simulated (green) cross-correlation signals. The contrast between peaks of the cross-correlation signal, for both theory and experiment, is limited by the duration and shape of the reference pulse and increases between soliton pairs with larger temporal separations. (d) Temporal separations between adjacent peaks for the measured (black) and simulated (green) cross-correlation signals. Mean fractional error is 3.5 %.

The cross-correlation of the disordered crystal shown in Fig. 4.7j with the reference pulse train confirms our interpretation of the spectral data for this crystal. Fig. 4.8b shows the simulated time-domain waveforms of the reference pulse and the crystal, and Fig. 4.8c shows measured and

simulated cross-correlation signals. The temporal spacing between the peaks of the cross-correlation signals is shown in Fig. 4.8d, where a high degree of agreement between the data and the simulation is observed.

The simulated cross-correlation signal is sensitive to the intensity profile of the reference pulse. We can measure only its intensity autocorrelation, which we combine with our knowledge of its production to estimate the intensity profile. To demonstrate that the validity of the results we present here is not sensitive to the exact assumptions we make about the intensity profile, we have also simulated the intensity cross-correlation resulting from an assumed Gaussian reference pulse with the same autocorrelation width as is measured for the reference pulse. The resulting simulated cross-correlation does not qualitatively agree as well with the experimental data in the depths of the wells between peaks because it does not contain satellite pulses which contribute to the variations in this depth, but the quantitative comparison of the temporal spacing between peaks is similar: the mean (maximum) normalized error between experiment and theory is 3.5 % (9.1 %) for the assumed electro-optic comb pulse and 4.8 % (10.6 %) for the Gaussian pulse.

## Chapter 5

### Theory of Kerr frequency combs in Fabry-Perot resonators

This chapter describes work that was reported in:

- Daniel C. Cole, Alessandra Gatti, Scott B. Papp, Franco Prati, and Luigi Lugiato. Theory of Kerr frequency combs in Fabry-Perot resonators. *Physical Review A* (2018), accepted, arXiv 1805.00427.

Generation of Kerr frequency combs in the ring-resonator geometry appears quite promising for applications. However, a second possibility is to use the same processes for comb generation, but with a Fabry-Perot (FP) resonator geometry. The FP geometry offers a new degree of freedom relative to the ring resonator, which is the possibility to employ chirped mirrors, mirror coatings, or distributed Bragg reflectors, and therefore exert greater control over the total cavity dispersion. Other differences with the ring geometry may ultimately prove important; for example, the smaller footprint possible in a cavity of total length  $L$  with the FP geometry versus the ring geometry could allow for denser and more flexible integration of Kerr combs in photonics systems. Kerr-comb generation in an FP cavity was reported in 2009 in Ref. 36 and soliton generation using a pulsed pump laser was recently described in Ref. 37.

In this chapter we present a brief theoretical investigation of the difference in the nonlinear dynamics that occur in a Kerr-nonlinear FP resonator versus a Kerr-nonlinear ring resonator. Our starting point is the Fabry-Perot Lugiato-Lefever equation (FP-LLE), which is derived in detail in Ref. 122, beginning from a set of coupled equations that describe the interaction of the envelopes for the forward- and backward-propagating fields in the cavity with the Kerr medium. A derivation of equivalent coupled mode equations is provided in Ref. 37. We do not reproduce the derivation of the equation here; our goal is to understand its description of Kerr-comb dynamics. The equation

is:

$$\frac{\partial\psi}{\partial\tau} = -(1 + i\alpha)\psi + i|\psi|^2\psi - i\frac{\beta_2}{2}\frac{\partial^2\psi}{\partial\theta^2} + 2i\psi\langle|\psi|^2\rangle + F. \quad (5.1)$$

Here,  $\langle g \rangle$  denotes the spatial average over the domain:  $\langle g \rangle = \frac{1}{2\pi} \int_{-\pi}^{\pi} d\theta g(\theta)$ . This equation is identical to the LLE for the ring cavity except for the term  $2i\psi\langle|\psi|^2\rangle$  describing modulation by twice the average of the intracavity power. The coordinate  $\theta$  is defined as  $\theta = \pi z/L$ , where  $z$  is a co-moving longitudinal coordinate (so that, for example, solitons are stationary functions of  $\theta$ ) on a domain  $-L \leq z \leq L$ ;  $L$  is the single-pass length of the Fabry-Perot cavity. The time  $\tau$  is once again normalized to twice the photon lifetime  $\tau_\gamma$ :  $\tau = t/2\tau_\gamma$ . The normalized experimental parameters in the FP-LLE are the same as in the LLE for the ring cavity, with  $\alpha$  the detuning,  $\beta_2$  the dispersion, and  $F^2$  the pump power:

$$\alpha = -\frac{2(\omega_o - \omega_c)}{\Delta\omega_o}, \quad (5.2)$$

$$\beta_2 = -\frac{2D_2}{\Delta\omega_{tot}} = -\frac{2}{\Delta\omega_o} \frac{\partial^2\omega_\mu}{\partial\mu^2} \Big|_{\mu=0}, \quad (5.3)$$

$$F^2 = \frac{8g_o\Delta\omega_{ext}}{\Delta\omega_{tot}^3} \frac{A_{eff}}{A_{in}} \frac{n_o}{n_{ext}} \frac{P}{\hbar\omega_o}. \quad (5.4)$$

In the above,  $\omega_\mu$  represents the set of resonance frequencies of the cavity including the effects of dispersion, with  $\mu = 0$  indexing the pumped mode. The cavity loss and coupling rates  $\Delta\omega$  and  $\Delta\omega_{ext}$  are related to the mirror reflectivity  $R$  and transmission  $T$  via  $\Delta\omega = (1 - R)c/n_g L$  (where two identical mirrors are assumed) and  $\Delta\omega_{ext} = cT/2n_g L$ , with  $n_g = c/v_g$  the group index. The quantities  $A_{in}$  and  $A_{eff}$  represent the mode's effective area  $\pi w_{in}^2$  (for a Gaussian mode of radius  $w$ ) at the input mirror and the same averaged over the cavity of length  $L$ ,  $\frac{\pi}{L} \int dz w(z)^2$ , respectively. Further,  $g_0 = n_2\hbar\omega_o^2 D_1 / (2\pi n_g A_{eff})$  is the nonlinear gain parameter, where  $D_1 = \frac{\partial\omega_\mu}{\partial\mu} \Big|_{\mu=0}$  is the cavity free-spectral range in angular frequency (here and in Eq. (5.3)  $\mu$  is treated as a continuous variable). The nonlinear index  $n_2$  is related to the third-order susceptibility via  $\chi^{(3)} = (4/3)n_0^2\epsilon_0 c n_2$ , where  $n_0$  is the refractive index of the nonlinear medium. The power  $P = \eta P_{inc}$  denotes the mode-matched power, with mode-matching factor  $\eta$  and power  $P_{inc}$  incident on the input mirror, and  $n_{ext}$  is the refractive index of the medium external to the cavity.

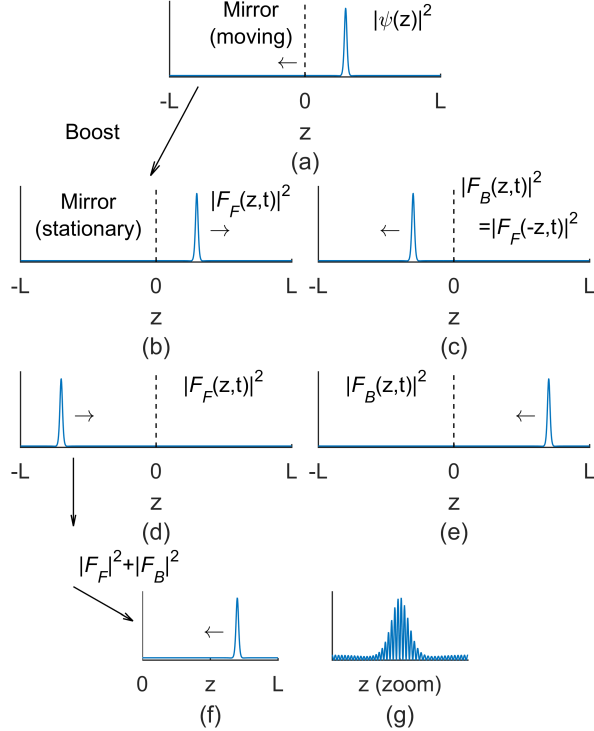


Figure 5.1: **Relationship between the physical field in the Fabry-Perot cavity and the co-moving field  $\psi$ .** (a) A soliton stationary solution to the FP-LLE in the co-moving domain of length  $2L$ , in which the physical components of the cavity (e.g. mirror) move. (b) Intensity of the field  $F_F$  in the lab frame, in which the cavity is stationary. (c) Intensity of  $F_B$  in the lab frame, related to  $F_F$  by reflection about the origin. (d,e) Depictions of the same after propagation for half of the cavity round-trip time. (f) Total intensity of the field on the physical domain  $0 \leq z \leq L$ . (g) The intensity of the field including the background standing wave that results multiplication of  $F_F$  and  $F_B$  by the appropriate traveling waves.

The formulation of the FP-LLE in terms of the field  $\psi$  defined in the co-moving domain of length  $2L$  facilitates numerical simulation of the nonlinear dynamics. To obtain the physical, propagating field in the Fabry-Perot cavity, the arguments of the field  $\psi$  are transformed back to dimensionful parameters so that we have  $\psi(z, t)$ , and then this field is boosted to group velocity  $v_g$  in the domain of length  $2L$  to obtain  $\psi_v$ , which propagates with periodic boundary conditions  $\psi_v(-L, t) = \psi_v(L, t)$ . From  $\psi_v(z, t)$  we define functions  $F_F$  and  $F_B$  that are proportional to the forward-propagating and backward-propagating envelopes of the electric field as  $F_F(z, t) \propto \psi_v(z, t)$  and  $F_B(z, t) \propto \psi_v(-z, t)$ , so that they are related by reflection about  $z = 0$ . The quantity  $|F_B(z, t)|^2 + |F_F(z, t)|^2$  on the physical domain  $0 \leq z \leq L$  is then proportional to the intensity in the FP cavity as a function of

time, averaged over fast spatial and temporal oscillations associated with the optical frequency. If desired, these can be included by multiplying  $F_B$  and  $F_F$  by the appropriate traveling waves before summation. This process is depicted schematically in Fig. 5.1.

In the remainder of this chapter we provide an investigation of the nonlinear dynamics in a Fabry-Perot cavity as they relate to the generation of frequency combs.

### 5.1 General relationship between the ring LLE and the FP-LLE

As can be seen from Eq. 5.1 for the Fabry-Perot cavity and Eq. 2.12 for the ring cavity, the difference between the two geometries lies in the term in the FP-LLE  $2i\psi \langle |\psi|^2 \rangle$ . This term represents the cross-phase modulation of the field  $\psi(\theta, \tau)$  at each co-moving point  $\theta$  by the field  $\psi(\theta', \tau)$  at each other co-moving point  $\theta'$  as  $\theta$  and  $\theta'$  propagate through each other during a round trip of the Fabry Perot cavity. The incorporation of this effect into the FP-LLE as a spatial average is consistent with the inclusion of the drive  $F$  and out-coupling  $\Delta\omega_{ext}$  (which is included in the damping term  $\partial\psi/\partial\tau = -\psi\dots$ ) into the LLE as delocalized, constant operators; this approximation is valid for high-finesse cavities, in which the field  $\psi$  changes little on the timescale of a round trip.

We can investigate the stationary solutions to the FP-LLE by setting the time derivative to zero, and we find:

$$0 = -(1 + i\alpha)\psi + i|\psi|^2\psi + 2i\psi \langle |\psi|^2 \rangle - i\frac{\beta_2}{2} \frac{\partial^2\psi}{\partial\theta^2} + F \quad (5.5)$$

$$= -(1 + i(\alpha - 2\psi \langle |\psi|^2 \rangle))\psi + i|\psi|^2\psi - i\frac{\beta_2}{2} \frac{\partial^2\psi}{\partial\theta^2} + F \quad (5.6)$$

$$= -(1 + i\alpha')\psi + i|\psi|^2\psi - i\frac{\beta_2}{2} \frac{\partial^2\psi}{\partial\theta^2} + F, \quad (5.7)$$

where we have defined  $\alpha' = \alpha - 2 \langle |\psi|^2 \rangle$ . We can immediately see from Eq. 5.7 that the stationary solutions to the FP-LLE at a point  $(\alpha, F^2)$  are the same as the stationary solutions to the ring LLE at the point  $(\alpha', F^2)$ . Physically, this arises from the need for increased detuning to maintain the round-trip phase shift at zero for each point  $\theta$  in the co-moving frame as the nonlinear phase shift is increased by the cross-phase modulation. As a consequence of this relationship, we expect that the FP-LLE exhibits the same stationary solutions as the ring LLE but with a shift in the detuning

parameter between the two geometries. In the remainder of this chapter we briefly discuss extended patterns (Turing patterns and chaos) in the FP-LLE, and then provide a longer discussion of solitons in the FP-LLE and how they differ from solitons in the ring geometry.

## 5.2 Extended patterns in the FP-LLE

We confirm the existence of Turing patterns and spatiotemporal chaos under the FP-LLE with numerical simulations of Eq. 5.1. A Turing pattern simulated at the point ( $\alpha = 2.5, F^2 = 6$ ) is plotted in the  $\theta$  domain in Fig. 5.2. An interesting contrast between the ring and FP geometries lies in the nature of stationary solutions to Eq. 5.1. For a stationary solution to the ring LLE, the intensity profile remains constant up to simple circulation about the ring at the group velocity. This is not the case for the FP-LLE, where a stationary solution to 5.1 such that  $\partial\psi/\partial\tau = 0$  does not correspond to a time-invariant intensity pattern, due to the intensity interference between counter-propagating components of  $\psi$ . We demonstrate this by plotting in Fig. 5.2b the physical intensity pattern (averaged over fast spatial and temporal oscillations) in the FP cavity corresponding to the Turing pattern shown in Fig. 5.2a at two different times. As the fields  $F_F$  and  $F_B$  circulate in the cavity, the number and positions of intensity maxima change.

The FP-LLE also exhibits chaos. In Fig. 5.2c we plot a snapshot of a chaotic waveform simulated at the point ( $\alpha = 5.3, F^2 = 8$ ). It is interesting to note that as  $\psi$  varies in time so does the average intensity  $\langle |\psi|^2 \rangle$ . This leads to a time-varying effective detuning value  $\alpha' = \alpha - 2 \langle |\psi|^2 \rangle$ . A natural question, then, is whether this time-varying  $\alpha'$  affects the dynamics of chaos. We investigate this by conducting a simulation of chaos with a duration of 10,000 photon lifetimes under the FP-LLE at the point ( $\alpha = 5.3, F^2 = 8$ ). We then calculate the time-averaged  $\alpha'$  value:  $\overline{\alpha'} = \alpha - 2\overline{\langle |\psi|^2 \rangle} = 1.1$ , where  $\bar{g}$  is the time average of  $g(t)$ , and conduct a ring-LLE simulation at the corresponding point. To compare the dynamics of chaos in each case, we record the amplitudes of local maxima in  $|\psi|^2$  throughout the simulation. This data is displayed in histograms in Fig. 5.2d, from which it is apparent that this calculation does not reveal a significant difference between the chaotic dynamics in ring resonator and FP cavities. Nevertheless, this could be an interesting

subject to investigate further.

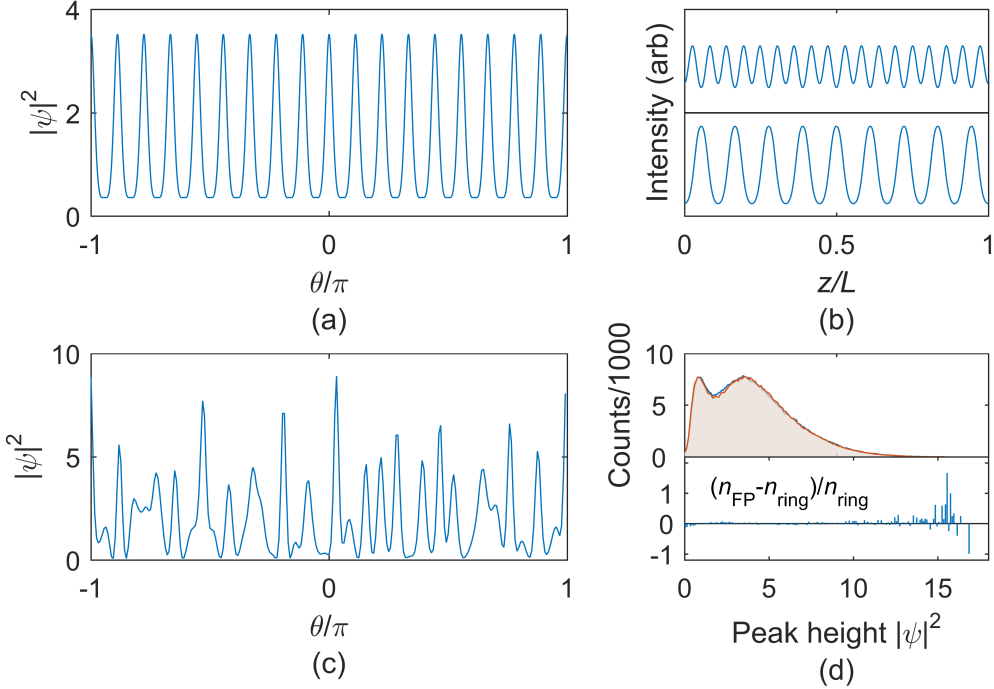


**Figure 5.2: Extended patterns in the FP-LLE.** (a) A Turing pattern simulated at the point ( $\alpha = 2.5, F^2 = 6$ ) with  $-\beta = 0.02$ . (b) Physical intensity pattern in the cavity corresponding to the Turing pattern shown in (a) at two different times. As  $F_F$  and  $F_B$  evolve, the number and positions of the local maxima change. (c) Snapshot of chaos simulated at the point ( $\alpha = 5.3, F^2 = 8$ ) with  $\beta = -0.02$ . (d) Top: Histogram of the local maxima values in  $\psi$  over a simulation of chaos at the point ( $\alpha = 5.3, F^2 = 8$ ) with  $\beta = -0.02$  for ten thousand photon lifetimes (blue) and at the corresponding point for the ring LLE (orange). Bottom: Fractional difference between the two histograms.

### 5.3 Solitons in the FP-LLE

#### 5.3.1 Analytical approximation for solitons in the FP-LLE

Equipped with the definition  $\alpha' = \alpha - 2 < |\psi|^2 >$  and the relation given in Eq. 5.7, we can investigate the soliton solutions to the FP-LLE. We can immediately adapt the analytical approximation to the soliton solution for the ring LLE, which we recall here for convenience, indicating parameters defined by the detuning for the ring LLE with the ‘prime’ superscript as in  $\alpha'$ :

$$\psi_{sol} = \psi'_{CW,min} + e^{i\phi'_0} \sqrt{2\alpha'} \operatorname{sech} \sqrt{\frac{2\alpha'}{-\beta_2}} \theta. \quad (5.8)$$

Here  $\psi'_{CW,min}$  is the flat solution to the ring LLE from Eq. 2.20 at the point where the soliton solution is desired; when multiple flat solutions exist,  $\psi'_{CW,min}$  is the one corresponding to the smallest intensity  $\rho'_1$  found by solving  $F^2 = (1 + (\alpha' - \rho')^2)\rho'$ . The phase  $\phi'_0$  is again defined as  $\phi'_0 = \cos^{-1}(\sqrt{8\alpha'}/\pi F)$ . Thus, an approximate soliton solution to the ring LLE according to Eq. 5.8 is also an approximate soliton solution to the FP-LLE at the detuning  $\alpha$ , where:

$$\alpha = \alpha' + \frac{1}{\pi} \int d\theta |\psi_{sol}|^2 \quad (5.9)$$

$$\begin{aligned} &= \alpha' + 2\rho'_1 + \frac{2}{\pi} \sqrt{-2\alpha'\beta_2} \tanh \left( \pi \sqrt{\frac{2\alpha'}{-\beta_2}} \right) \\ &\quad + \frac{8}{\pi} \sqrt{-\beta_2\rho'_1} \cos(\phi' - \phi'_0) \tan^{-1} \tanh \left( \pi \sqrt{\frac{\alpha'}{-2\beta_2}} \right) \end{aligned} \quad (5.10)$$

and  $\phi' = \tan^{-1}(\rho'_1 - \alpha')$ . To find the approximate soliton solution to the FP-LLE at a point  $(\alpha, F^2)$ , Eq. 5.10 must be numerically inverted to find  $\alpha'$ , after which  $\psi_{sol}$  can be obtained. As is the case for the ring LLE, an approximation to multi-soliton ensembles is possible as:

$$\psi_{ens} = \psi'_{CW,min} + \sqrt{2\alpha'} e^{i\phi'_0} \sum_j \operatorname{sech} \left( \sqrt{\frac{2\alpha'}{-\beta_2}} (\theta - \theta_j) \right). \quad (5.11)$$

Such an ensemble may or may not be stable, depending on the separation between the locations of the solitons  $\{\theta_j\}$  and the temporal width of the solitons determined by  $\alpha'$  and  $\beta_2$ . Each soliton in the ensemble contributes to the average intensity  $\langle |\psi|^2 \rangle$ , so Eq. 5.10 no longer holds; instead, Eq. 5.11 must be integrated to determine a new value for  $\alpha'$ .

### 5.3.2 Existence range of single solitons

An important consequence of the additional nonlinear term  $2i\psi \langle |\psi|^2 \rangle$  in the FP-LLE is that the range of parameters over which single solitons exist acquires a dependence on the dispersion parameter  $\beta_2$ , through the effect of dispersion on pulse energy. This is in contrast to the situation for the ring LLE, where the existence range is independent of  $\beta_2$ . For the FP-LLE the existence range also depends on the number of co-propagating pulses and can be greatly extended in the case of many co-propagating solitons; this is not our focus here.

The minimum value of detuning  $\alpha$  at which solitons exist as a function of  $F^2$  is determined by

the existence of a stable flat solution to the LLE that can form the CW background for the soliton. The maximum value of detuning for which solitons can exist is determined by  $\alpha' = \alpha - 2\langle|\psi|^2\rangle$  according to  $\alpha'_{max}(F^2) = \pi^2 F^2 / 8$ , which approximately gives the maximum detuning for solitons in the ring LLE [54].

For the FP-LLE, a stable flat solution exists to the right of the line  $F_+^2(\alpha)$  in the  $\alpha - F^2$  plane that bounds the region of multiple flat solutions from above. As we did for the ring LLE, we calculate this line by beginning from the equation describing intensity of the flat stationary solutions  $\rho$  to the FP-LLE:

$$F^2 = (1 + (\alpha - 3\rho)^2)\rho. \quad (5.12)$$

There are multiple flat solutions between the values  $\rho_{\pm}$  at which  $\partial F^2 / \partial \rho = 0$ ; the upper boundary of this region  $F_+^2(\alpha)$  is obtained by inserting  $\rho_- = (2\alpha - \sqrt{\alpha^2 - 3})/9$  into Eq. 5.12:

$$F_+^2(\alpha) = \left[ 1 + \left( \frac{\alpha + \sqrt{\alpha^2 - 3}}{3} \right)^2 \right] \frac{2\alpha - \sqrt{\alpha^2 - 3}}{9} \quad (5.13)$$

This curve bounds the region of soliton existence on the left (lower  $\alpha$ ) in the limit  $\beta_2 \rightarrow 0^-$  ( $\beta_2$  goes to zero from below), which corresponds to the limit of zero soliton energy. In the same limit, the right boundary of soliton existence (higher  $\alpha$ ) is the line  $\alpha_{max}(F^2) = \alpha'_{max}(F^2) + 2\rho'_1(\alpha'_{max}(F^2), F^2)$ , where  $\rho'_1(\alpha', F^2)$  is the intensity of the smallest flat solution to the ring LLE at  $(\alpha', F^2)$ .

We can obtain approximations to the bounds of soliton existence for finite  $\beta_2$  by first finding the amplitudes  $\rho_L(F^2)$  and  $\rho_R(F^2)$  of the soliton background for the left and right boundaries of soliton existence in the zero-dispersion limit and then using Eq. 5.10 to calculate the value of  $\alpha$  at which a soliton exists on a background of that amplitude for finite  $\beta_2$ . This process amounts to taking the amplitude of the background as an indication of the effective detuning under which the soliton evolves. These results are summarized in Fig. 5.3. Fig. 5.3a shows the curves corresponding to the  $\beta_2 \rightarrow 0^-$  limit and for finite  $\beta_2$  values of -0.001, -0.02, and -0.3, and Fig. 5.3b shows a comparison between the approximate curves for finite  $\beta_2$  and the soliton existence boundaries as revealed by full simulations of the FP-LLE. The analytical approximation is accurate for low  $F^2$  and small dispersion, but becomes less accurate as these quantities increase. This is because breather

solitons whose amplitudes oscillate periodically are found near  $\alpha_{min}$  for larger values of  $F^2$ . Breather solitons are accompanied by traveling waves that propagate away from the soliton and diminish in amplitude as they do so, and their range increases with the dispersion. For larger values of dispersion these waves fill the cavity, and in this case the flat background whose stability forms the basis for approximating the dispersion-dependent boundary curves is actually not present.

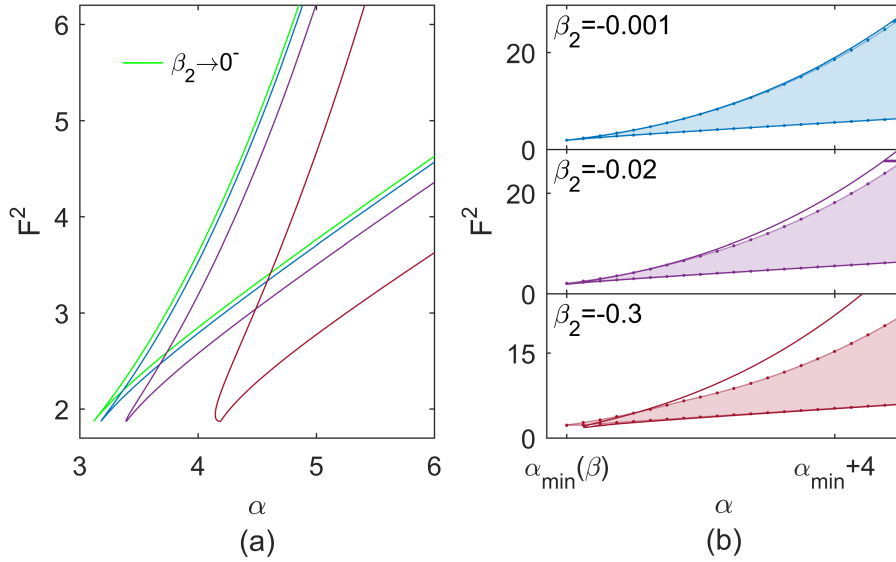


**Figure 5.3: Boundaries of soliton existence in the FP-LLE.** (a) Exact boundary of soliton existence for the limit  $\beta_2 \rightarrow 0^-$  and analytical approximations to the boundaries for three finite values of dispersion:  $\beta_2 = -0.001$  (blue),  $\beta_2 = -0.02$  (purple), and  $\beta_2 = -0.3$  (red). (b) Comparison between the finite-dispersion approximations from (a) and soliton existence boundaries as revealed by full simulations of the FP-LLE.

The lines  $\alpha_{min}(F^2)$  and  $\alpha_{max}(F^2)$  intersect at  $F^2 = F_I^2 \approx 1.87$ . Below this value of the pump power solitons do not exist for the FP-LLE, and this can be seen as follows: The value of  $\rho'_{min}$  describing the amplitude of the soliton background along the line of maximum detuning  $\alpha'_{max}$  for the ring LLE is in general also a flat solution  $\rho$  of the FP-LLE at the corresponding point  $\alpha_{max} = \alpha'_{max} + 2\rho'_{min}(\alpha'_{max}, F^2)$ . However, when  $F^2 < F_I^2 \approx 1.87$ , the flat solution  $\rho'_{min}$  to the ring LLE is not the smallest flat solution to the FP-LLE; instead, it is the middle of three, and is therefore unstable. Therefore, when  $F^2 < F_I^2$  the line  $\alpha_{max}(F^2)$  as defined above does not represent the right boundary of soliton existence for the FP-LLE. In fact, below this point, for all values of  $\alpha$

where a stable flat solution to the FP-LLE  $\rho_{min}$  exists,  $\alpha - 2\rho_{min}(\alpha, F^2) > \alpha'_{max}$ , preventing the existence of solitons. This is an interesting contrast with the ring LLE, where the corresponding lines bounding soliton existence intersect at  $F^2 = 1.175$  and where we can verify in simulations that solitons exist for e.g.  $F^2 = 1.5$ .

### 5.3.3 Generation of single solitons through laser frequency scans

A second important consequence of the additional nonlinear term in the FP-LLE relative to the ring LLE is an increase in the range of  $\alpha$  values, for a given value of  $F^2$ , at which the state of  $\psi$  can be either an extended pattern (spatiotemporal chaos or Turing pattern) or a soliton/soliton ensemble. This is because the extended patterns fill the domain and, because of their higher average intensity, experience a greater nonlinear shift than lower duty-cycle single solitons or soliton ensembles due to the additional nonlinear term. Here we discuss the implications of this fact for the experimental generation of single solitons through decreasing-frequency scans of the pump laser, as discussed in Chapter 2, Sec. 2.3.3. We summarize the results in Fig. 5.4. In Fig. 5.4a we show example simulations of spatiotemporal chaos and a single soliton to illustrate this degeneracy. Both of these simulations are conducted at the point  $(\alpha = 8, F^2 = 8)$ , and the soliton and chaos are also degenerate with a stable flat solution, with the nature of  $\psi$  dependent upon the initial conditions.

It has been established that condensation of solitons from an extended pattern in a sweep in which  $\alpha$  increases is a useful way of obtaining single solitons in experiments. Because this method relies on the excitation of an extended pattern (chaos or Turing pattern) to provide initial conditions out of which solitons condense as  $\alpha$  is increased, it is important that the maximum detuning (the value of  $\alpha$  where  $\alpha' = \alpha'_{max} = \pi^2 F^2 / 8$ ) for single solitons is larger than the  $\alpha$  value at which an extended pattern will transition to a soliton ensemble. Otherwise, the generation of single solitons using this method will be difficult or impossible. To investigate this, we numerically perform slow scans across the resonance to identify where the transition from extended patterns to independent solitons occurs. These scans are conducted slowly to approximate adiabaticity:  $d\alpha/d\tau = 2.5 \times 10^{-4}$ . We perform 10 scans across the resonance at each integer value of  $F^2$  from 3 to 12 with  $\beta = -0.02$ ,

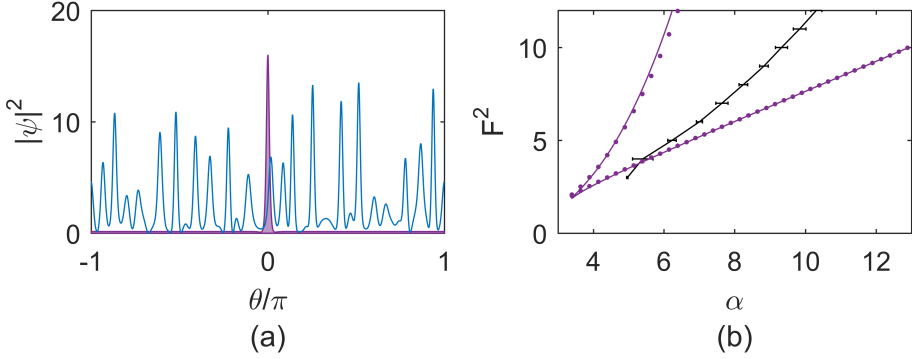


**Figure 5.4: Transition from extended patterns to single solitons in the FP-LLE.** (a) Simulated spatiotemporal chaos (blue) and single soliton solution (purple), either of which can exist at the point ( $\alpha = 8, F^2 = 8$ ). The amplitude of the soliton is larger than the characteristic amplitude of the features in the chaos because the effective detuning  $\alpha'$  is larger for the soliton. (b) Analytical (lines) and numerical (dots) soliton existence limits (purple) for  $\beta = -0.02$  from panel (a) and the upper bound in  $\alpha$  for the existence of spatiotemporal chaos/Turing patterns (black with error bars), estimated as described in the text.

and we identify the transition from extended pattern to independent solitons by inspection of several quantities as  $\alpha$  is varied: the set of local maxima and minima of  $|\psi|^2$  (see Ref. 64), the distance between local maxima, and the number of local maxima above  $|\psi|^2 = 1$ . In Fig. 5.4b we plot the line representing the upper boundary in  $\alpha$  of extended patterns obtained in the scans across the resonance. Error bars represent the standard deviation of the values  $\alpha$  at which the transition is observed, with this spread in the values arising due to the chaotic fluctuations in the total intracavity power and therefore also in the size of the nonlinear integral term. These results indicate that the region over which single solitons exist and extended patterns do not is narrow for small pump powers  $F^2$ , and widens as  $F^2$  is increased. Without performing experiments, it is impossible to precisely quantify the limitations imposed by this observation, but we expect this finding to be useful in refining schemes for single-soliton generation in Fabry-Perot resonators. It is important to note that challenges associated with the necessary transition from high duty-cycle extended patterns to low duty-cycle solitons are alleviated by pulsed pumping, which was the technique used by Obrzud, Lecomte, and Herr in their recent report of soliton generation in FP resonators.

## Chapter 6

### Microresonator-based frequency combs: Summary and outlook

Chapters 2-5 discussed generation of frequency combs from a continuous-wave laser by parametric frequency conversion in Kerr-nonlinear resonators. I described three results: 1. The investigation and implementation of a technique for spontaneous soliton generation in Kerr resonators using a phase-modulated pump laser, 2. The observation and explanation of soliton crystals in Kerr resonators, and 3. A theoretical investigation of Kerr-comb generation in Fabry-Perot cavities, with an emphasis on the properties of solitons and soliton generation. These results all help to more clearly define what is possible with these systems, and suggest avenues for further research.

Soliton generation with a phase-modulated pump laser is a promising candidate for inclusion in chip-integrated Kerr-comb systems as the mechanism by which single-soliton operation is initiated. Two directions for continued work are additional analytical investigations into the full LLE with a phase-modulated pump, which could provide insight into the dynamics beyond what is possible using the approximations described in Chapter 3; and implementation of the technique with resonators that have electronically-inaccessible free-spectral ranges, using the subharmonic-modulation approach that was proposed. Incorporation of the technique into a chip-integrated Kerr-soliton comb may also require modification and further development of the technique that was used to overcome thermal instabilities associated with the increasing-frequency pump-laser scan.

The investigation of soliton crystals presented here serves several important purposes. First, it represented an important step towards full explanation of observed Kerr-comb phenomena in terms of the LLE model. Second, soliton crystals have the attractive properties of single-soliton Kerr

combs, with the additional property that a soliton crystal of  $N$  pulses has conversion efficiency of pump-laser power into the comb that is roughly  $N$  times higher than a comparable single-soliton comb. With careful preparation of a particular crystal state, this could make them attractive for applications like optical arbitrary waveform generation and nonlinear spectroscopy. Additionally, soliton crystals present a hugely degenerate configuration space that could be useful, for example, in implementations of an on-chip optical buffer or in communications applications [55]. Finally, experimental generation of soliton crystals is significantly simpler than generation of single solitons, where the change in the duty cycle of the optical waveform from extended pattern to single soliton leads to thermal instabilities that must be addressed through precise control of the pump-laser power and frequency. It is possible to propose a scheme for deterministic on-chip soliton crystal generation that makes use of two resonators, each constructed of looped single-mode optical waveguides. One resonator is pumped by a laser and hosts the soliton crystal. The second resonator need not be pumped, and exists to provide a specific perturbation to the mode structure of the first resonator to enable soliton crystallization; this could be achieved through careful engineering of the coupling between the resonators. If the free-spectral range of the second resonator is considerably higher than the free-spectral range of the first, and not near one of its harmonics, then realization of single-mode perturbation to the mode structure of the first resonator that was assumed in Chapter 4 could be achieved. Implementing deterministic soliton crystal generation on a chip in this way could greatly simplify the requirements on the other components in a system for full-integration of Kerr solitons, as soliton generation could be achieved through slow tuning of the pump laser.

The theoretical investigation of Kerr-comb generation in the Fabry-Perot geometry will provide useful guidance for future experimental work. An obvious direction for continued work is the generation of solitons in Fabry-Perot cavities that make use of the additional degree of freedom provided by the dispersion applied by reflection at the ends of the cavity. This would build on previous experiments [36, 37]. In fact, soliton generation in Fabry-Perot cavities constructed of potted fiber ferrules with high-reflectivity end-coatings has already been realized at NIST Boulder [123], but there remains work to be done to achieve control of the total cavity dispersion with chirped

mirror-coatings. Unresolved questions include the effect of uncontrolled expansion of the mode in the coating on both the mirror reflectivity and its group-velocity dispersion. Looking to the chip scale, integrated Fabry-Perot cavities constructed of single-mode waveguides with photonic-crystal mirrors is a promising route for development that would further reduce the footprint of Kerr-comb systems. This work is ongoing at NIST Boulder, and primary comb has been observed in such a cavity [124]. Finally, I note that the proposal for deterministic chip-scale generation of soliton crystals presented above could be realized with two co-linear on-chip Fabry-Perot cavities, where the first cavity hosts the crystal, which is out-coupled in reflection, and the second cavity provides a perturbation to the first cavity's mode structure.

## Chapter 7

### A frequency comb generated through active modulation of a continuous-wave laser

This chapter describes work that was reported in:

- Daniel C. Cole, Katja M. Beha, Scott A. Diddams, and Scott B. Papp. Octave-spanning supercontinuum generation via microwave frequency multiplication. *Proceedings of the 8th Sympson on Frequency Standards and Metrology 2015, Journal of Physics: Conference Series* **723** (2016), 012035.
- Katja Beha, Daniel C. Cole, Pascal Del'Haye, Aurélien Coillet, Scott A. Diddams, and Scott B. Papp. Electronic synthesis of light. *Optica* **4** (2017), 406–411.

In this chapter, I discuss the generation of high-repetition-rate frequency combs through electro-optic modulation of a continuous-wave laser—so-called EOM combs [127–136]. This scheme represents an alternative to parametric generation of high-repetition-rate combs in Kerr resonators, and as the technology matures it will likely find a niche in the application space that leverages its long-term stability, lack of moving parts, and possibility for robust turn-key operation. First I present the operational principle, followed by experimental results that represent the first  $f - 2f$  self-referencing of a comb of this kind. Then I provide a discussion of the noise processes specific to the EOM comb, the investigation and mitigation of which is a significant contribution of the work described here. I conclude with a brief outlook for the technology.

#### 7.1 Principle of operation

At its simplest, an EOM comb is a set of lines generated by passing a CW ‘seed’ laser through cascaded phase and intensity modulators to generate a train of chirped pulses. After this initial step, the pulse train may be propagated through a dispersive medium to temporally compress the pulses,

and they can be subsequently spectrally broadened. A generic expression for the electric field before temporal compression results from the product of carrier field  $E_o e^{i\omega_c t}$  with operators

$$\frac{e^{i\Phi(t)} + e^{-i\Phi(t)}}{2} = \cos \Phi(t), \quad (7.1)$$

where

$$\Phi(t) = \phi_{DC} + \phi_{RF} \sin(\omega_{rep}t + \phi_{IMPM}) \quad (7.2)$$

representing the intensity modulation and

$$\exp[i\delta_{PM} \sin \omega_{rep}t] \quad (7.3)$$

representing the phase modulation. Here  $E_o$  and  $\omega_c$  are the complex amplitude and the carrier frequency of the seed laser. The phases  $\phi_{DC}$  and  $\phi_{RF}$  represent the DC bias and depth of the intensity modulation, respectively, which experimentally are sourced from a DC power supply and an RF synthesizer. Writing the intensity-modulation operator as the sum of exponentials reveals the physical origin of intensity modulation as phase modulation in two paths with opposite sign. The phase-modulation index, which sets the initial bandwidth of the EOM comb, is  $\delta_{PM}$ . The comb's repetition rate is  $f_{rep} = \omega_{rep}/2\pi$ , with  $\omega_{rep}$  the angular frequency of the phase and intensity modulation. In practice it is useful to derive these signals from the same synthesizer. The phase  $\phi_{IMPM}$  represents a phase difference between the IM and PM operators arising from path-length differences, which can be controlled via the insertion of a phase shifter in one electrical path.

For convenient temporal pulse compression and subsequent spectral broadening of the comb it is desirable to configure the IM and PM to yield a train of 50 % duty-cycle pulses with normal chirp (temporally increasing carrier frequency). To achieve this, both  $\phi_{DC}$  and  $\phi_{RF}$  are set to  $\pi/4$  and  $\phi_{IMPM}$  is set to zero. Experimentally, one can determine the appropriate RF drive power and bias by adjusting the ratios  $\eta_1 = P_1/P_0$  and  $\eta_2 = P_2/P_0$  between the first- and second-order sidebands and the carrier to  $\eta_1 = -7.4$  dB and  $\eta_2 = -21.3$  dB with only intensity modulation applied to the seed laser.<sup>1</sup> Setting  $\phi_{IMPM}$  to either zero or  $\pi$  is achieved by examining the optical spectrum of the EOM

---

<sup>1</sup> This assumes that the modulation is applied to both paths in the intensity modulator with opposite sign; the correct ratios for a Mach-Zehnder intensity modulator with modulation in only one path are  $\eta_1 = -5.8$  dB and

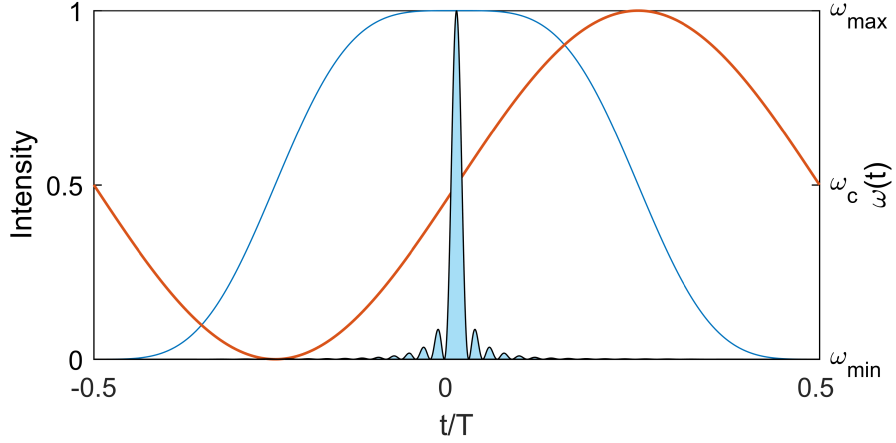


Figure 7.1: **Operating principle of an electro-optic modulation comb.** A train of chirped pulses is generated by combined electro-optic phase and intensity modulation, and the pulses can then be conveniently temporally compressed in a dispersive medium. Light blue line (plotted with respect to the left axis): Initial intensity profile of a single EOM comb pulse as described by Eq. 7.4. Orange (right axis): Instantaneous carrier frequency, which varies about  $\omega_c$  by  $\pm\delta_{PM}\omega_{rep}$  and increases approximately linearly in time while the pulse amplitude is high. Solid blue (left axis): Pulse resulting from compression of the initial pulse to its transform limit. The temporal duration of this pulse decreases as  $\delta_{PM}$  increases as a result of the increased bandwidth of the comb; here the phase-modulation depth  $\delta_{PM} = 31\pi/4$  is used. The compressed pulse has higher peak power (in this case by a factor of 26.5); for convenient depiction of both pulses the compressed pulse has been rescaled.

comb with both IM and PM applied. The spectrum is asymmetric if  $\phi_{IMPM}$  is not zero or  $\pi$  due to stronger transmission of either the high- or low-frequency components of the phase-modulated seed laser through the intensity modulators. The optical spectrum of the comb, which does not include phase information, is the same for  $\phi_{IMPM} = 0$  or  $\pi$ ; the difference between the two corresponds to reversal of the field in time or, equivalently, the difference between normal and anomalous chirp. Setting  $\phi_{IMPM}$  to zero is accomplished by verifying that the pulses are compressed by propagation in an appropriate length of an anomalously dispersive medium;  $\phi_{IMPM} = \pi$  corresponds to anomalous chirp on the initial pulse train, in which case the pulses will not be compressed.

A simplified and illuminating expression for the electric field of a normally-chirped 50 % duty-

---

$\eta_2 = -12.9$  dB. This difference arises from residual phase modulation on the output field in the latter case. To determine the internal configuration of the modulator, one can examine the action of the bias: if the modulation is applied to both paths with opposite signs, the bias will adjust only the ratios between the odd- and even-order sidebands while leaving the ratios within each group fixed. However, if the modulation is applied to only one path, the bias will change the ratio of each sideband to the carrier. These conclusions are reached by application of various forms of the Jacobi-Anger expansion.

cycle pulse train (up to a constant overall phase shift relative to the expressions above) is:

$$E = E_o \cos\left(\frac{\pi}{2} \sin^2 \frac{\omega_{rep} t}{2}\right) e^{i\omega_c t - i\delta_{PM} \cos \omega_{rep} t}. \quad (7.4)$$

This can be understood as the product of a time-varying real amplitude  $a(t) = E_o \cos\left(\frac{\pi}{2} \sin^2 \frac{\omega_{rep} t}{2}\right)$  and a phase factor from which the instantaneous carrier frequency  $\omega(t) = \omega_c + \omega_{rep} \delta_{PM} \sin \omega_{rep} t$  can be calculated. The carrier frequency  $\omega(t)$  is increasing when the amplitude  $a(t)$  is at its maximum, corresponding to normal chirp on the pulses. Fig. 7.1 depicts the intensity  $|E|^2$  and instantaneous carrier frequency of the field given by Eq. 7.4, as well as the intensity profile corresponding to compression of the same spectrum to its transform limit.

## 7.2 Generation of an EOM comb and detection of its carrier-envelope offset frequency

Here I describe the generation of an EOM comb with 10 GHz repetition rate and subsequent measurement of its carrier-envelope offset frequency. One advantage of the EOM comb scheme is that the generation and spectral broadening of the comb is well understood, and can be modeled accurately. To demonstrate this, I compare the results of simulations of the comb to the experimental output at each stage in the generation process.

The experimental setup is depicted in Fig. 7.2. The basic experimental scheme consists of the following steps: 1. Initial generation and temporal compression of the EOM comb pulse train; 2. Modest spectral broadening and temporal re-compression, along with propagation through a Fabry-Perot filter cavity for noise reduction (see Sec. 7.3); and 3. Octave-spanning supercontinuum generation and detection of the carrier-envelope offset frequency. The results described below represent the first time a frequency comb of this kind has been self-referenced. Key to the success of this approach is the implementation of nonlinear spectral broadening in two stages, which allows the second stage to be seeded with  $\sim 130$  fs pulses for coherent supercontinuum generation. Noise reduction with the Fabry-Perot filter cavity is also critical for coherent spectral broadening; I describe a characterization of this step below.

To generate the initial train of chirped pulses, a telecommunications-band CW laser is passed through cascaded phase and intensity modulators driven with a 10 GHz microwave signal. The intensity modulator is biased at the 50 % transmission point and driven with an RF amplitude appropriate for generation of a 50 % duty-cycle pulse train, as described above; the phase modulator is driven with modulation depth of  $\sim 31\pi/4 \sim 24.3$  rad. The relative phase between the modulators is set such that the phase applied by the phase modulator is at a minimum when the transmission of the intensity modulator is highest; this yields a train of normally-chirped (up-chirped) pulses. Fig. 7.2, Panel (i) presents a comparison between the simulated and measured spectra for the initial pulse train.

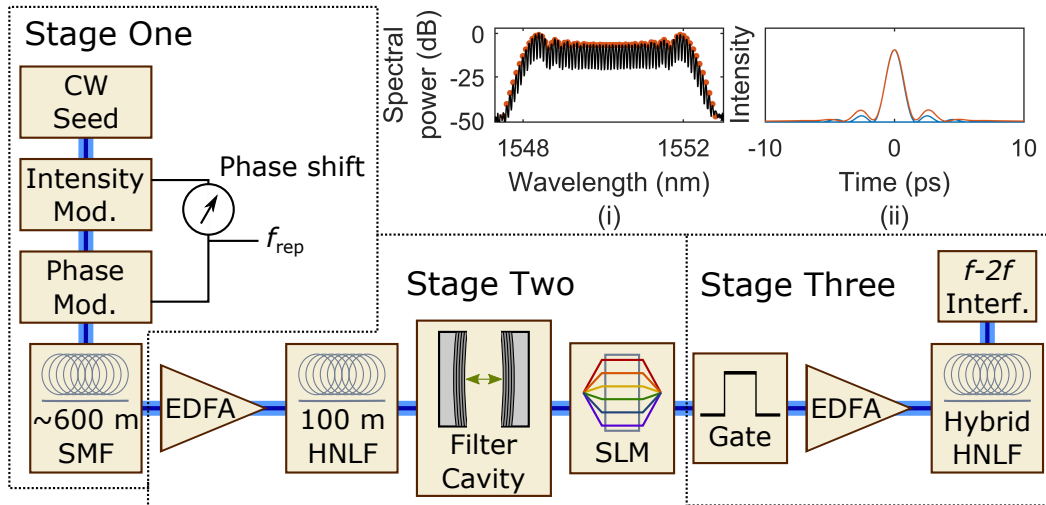


**Figure 7.2: Experimental setup for detection of the carrier-envelope offset frequency of an EOM comb after generation of a coherent supercontinuum.** Detection of  $f_0$  is performed with a three stage experiment. In Stage 1 a train of  $\sim 1.5$  ps pulses is generated. In Stage 2 these pulses are spectrally broadened and temporally compressed to  $\sim 130$  fs duration. In Stage 3 an octave-spanning supercontinuum is generated and  $f_0$  is detected in an  $f - 2f$  interferometer. Panel (i) shows the measured spectrum of the comb output by Stage 1 (black), along with a simulation of the same (orange). Panel (ii) shows simulation of the temporal compression of the pulses by propagation in 570 m of single-mode fiber (orange) and to the transform limit (blue).

Next, the chirped pulse train is propagated through 600 m of anomalously-dispersive SMF. The length of SMF that is appropriate for pulse compression depends on the bandwidth of the optical pulses to be compressed; equivalently, it depends on both the phase-modulation depth and the repetition rate of the pulse train. This temporal compression reduces the duration of the optical

pulses from  $\sim 50$  ps to  $\sim 1.5$  ps. A simulation of the resulting intensity profile and a comparison to the spectrum's transform-limited pulse profile is presented in Fig. 7.2, Panel (ii).

The compressed pulses are amplified to 400 mW average power in an erbium-doped fiber amplifier and launched into 100 m of HNLF. This section of HNLF has chromatic dispersion that is small and normal; this is carefully chosen to chirp the pulses via self-phase modulation while avoiding soliton-fission dynamics [137]. The result is a train of chirped  $\sim 1.5$  ps pulses exiting the fiber. In Fig. 7.3a we present the measured optical spectrum of this pulse train, as well as results of a numerical simulation of the spectral broadening in the 100 m of normally-dispersive HNLF. These simulations are conducted using the nonlinear Schrodinger equation (NLSE) including third order dispersion [40], taking as initial conditions the calculated SMF-compressed intensity profile of the EOM comb pulses shown in Fig. 7.2(ii). The dispersion values for the HNLF used in the simulation are  $D = -0.04$  ps/nm·km and  $D' = 0.003$  ps/nm $^2$ ·km, close to the values specified by the manufacturer. The simulation method is described in detail in Appendix B.

After propagation through the first section of HNLF, the pulses are passed through a high-finesse Fabry-Perot cavity for suppression of optical frequency fluctuations as discussed below. Then the pulses are temporally compressed again, this time using a commercial spatial light modulator (SLM) [138]; the SLM separates narrow spectral regions using a grating and passes them through individually controlled delaying elements before recombination. The SLM applies 2<sup>nd</sup>, 3<sup>rd</sup>, and 4<sup>th</sup> order chromatic dispersion, which simulations indicate is sufficient to compress the chirped pulses to  $\sim 130$  fs, near their transform limit. This is shown in Fig. 7.3b. While it is convenient, the SLM is not strictly necessary; it would also be possible to compress the pulses via propagation in an appropriate length of SMF. Figs. 7.3b and c present the compressed intensity profile and the evolution of the intensity profile, respectively, in simulated compression in SMF. Because the pulses are broadband, temporally short, and reasonably high energy, these simulations include the full dispersion profile of SMF and the Kerr nonlinearity.

The temporally compressed  $\sim 130$  fs pulses are then passed through an intensity modulator functioning as an electro-optic gate for repetition-rate downsampling (see Chapter 8). The gate

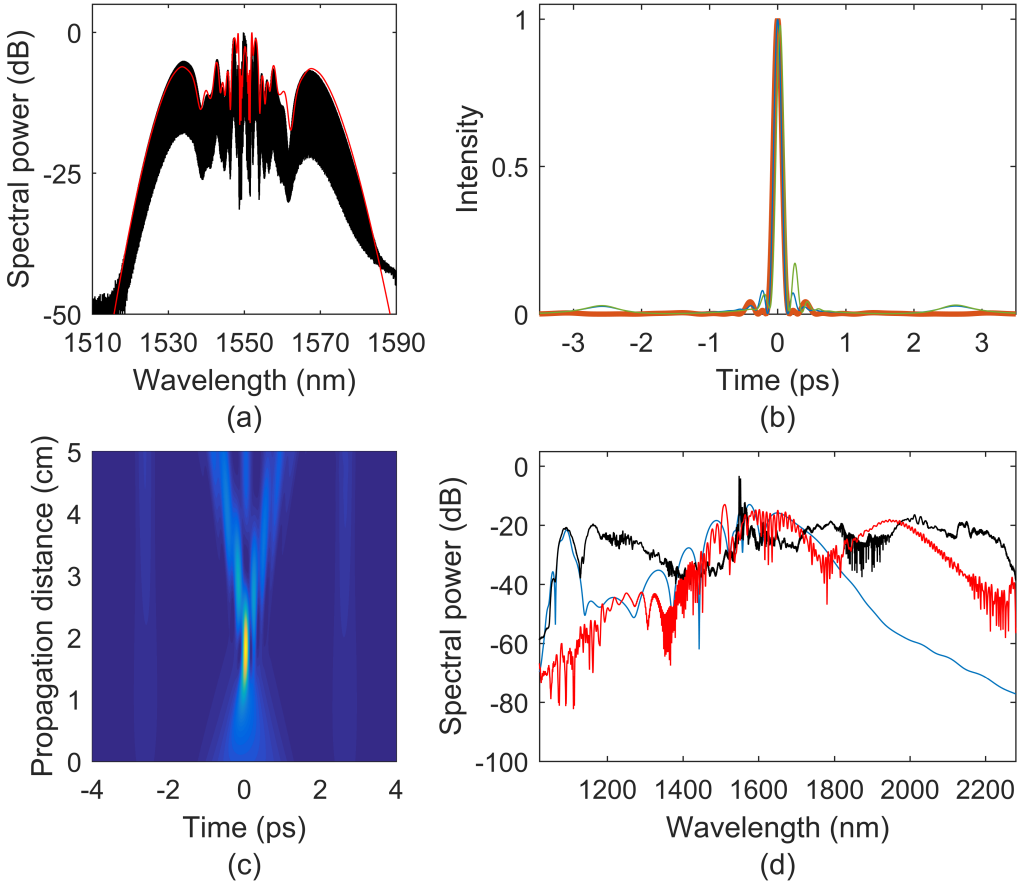


**Figure 7.3: Spectral broadening for generation of an octave-spanning supercontinuum.** (a) Measured optical spectrum after propagation in 100 m of low-normal-dispersion HNLF (black). The spectrum is broadened by self-phase modulation, which imposes a chirp on the pulses. Shown in red is a simulation of the same, conducted as described in the text. (b) Simulated pulse intensity envelopes after temporal re-compression to the transform limit (thick orange), in the SLM with 2<sup>nd</sup>-, 3<sup>rd</sup>-, and 4<sup>th</sup>-order dispersion (blue), and in an appropriate length of SMF (green). FWHM pulse durations are similar, but the SLM- and SMF-compressed pulses have energy in satellite pulses at  $\pm 2.5$  s, and the SMF-compressed pulse has a significant asymmetry. (c) False-color plot of simulated re-compression of the SPM-chirped pulses (red spectrum in panel (a)) in SMF. A minimum pulse duration of  $\sim 140$  fs is achieved after propagating through 1.93 cm of SMF. (d) Measured optical spectrum of the octave-spanning supercontinuum generated by the EOM comb system (black), plotted along with simulated spectra calculated as described in the text to investigate the effects of the 30 cm, highly-dispersive piece of HNLF (blue) and the 7.7 m, lower-dispersion piece of HNLF (red).

selectively transmits every fourth pulse, reducing the repetition rate of the pulse train to 2.5 GHz. This facilitates coherent supercontinuum generation in a second stage of spectral broadening by increasing the pulse energy that can be achieved at a given average power. This step is convenient but not strictly necessary, as shown in Fig. 7.6.

The downsampled 2.5 GHz pulse train is amplified to an average power of 1.4 W, resulting in a train of  $\sim 0.56$  nJ pulses. This pulse train is propagated through 8 m of hybrid HNLF, yielding the spectrum shown in Fig. 7.3d. This hybrid HNLF consists of two segments with different dispersion profiles, with each segment serving a different purpose. The first segment is 30 cm long and highly dispersive<sup>2</sup> ( $D = 6$  ps/nm·km), and generates a dispersive wave centered at 1090 nm. The second segment is 7.7 m long and has lower dispersion ( $D = 1.5$  ps/nm·km), and generates a Raman-self-frequency-shifted soliton centered near 2000 nm. For this final stage of broadening it is difficult to achieve quantitative agreement between the measured supercontinuum spectrum and simulations due to the sensitivity of the higher-order nonlinear effects (e.g. Raman and self-steepening) on the input parameters. However, the qualitative effect of each of the fibers that make up the hybrid HNLF can be understood by modeling propagation in each section separately. To do this we use the LaserFOAM program [139], which employs the generalized NLSE including Raman scattering, self-steepening, and 2nd- through 4th-order dispersion. The simulations are run independently, and both take as their initial conditions 170 fs sech pulses with 350 pJ energy, close to the energy coupled into the HNLF after accounting for losses. The results of these simulations are plotted in Fig. 7.3d.

The supercontinuum generated in the hybrid HNLF is coherent and suitable for  $f - 2f$  self-referencing. To detect the carrier-envelope offset frequency of the EOM comb, we pass the pulse train through an interferometer (see Fig. 1.2) consisting of a dichroic mirror, a delay stage in one path, and a 10 mm sample of periodically-poled lithium niobate that generates the second harmonic of supercontinuum light at 2140 nm. The dichroic mirror and delay stage enable adjustment of the relative timing between the native 1070 nm and doubled 2140 nm components of the supercontinuum so that they are temporally coincident. An optical band-pass filter centered at 1070 nm selects the supercontinuum components required for self-referencing, shown in Fig. 7.4a, and impinging the filtered light on a photodetector reveals the carrier-envelope offset frequency of the EOM comb, shown in Fig. 7.3b. Note that downsampling introduces an ambiguity in the offset frequency due to the increased density of comb modes in the downsampled pulse train; this ambiguity can be removed

---

<sup>2</sup> We quantify the dispersion using the standard  $D$  parameter:  $D = -\frac{2\pi c}{\lambda^2} k''$ , where  $k''$  is the GVD parameter described in Chapter 2.

by measuring the change in measured offset frequency with a change in  $f_{rep} = \omega_{rep}/2\pi$  provided by the synthesizer driving the modulators.

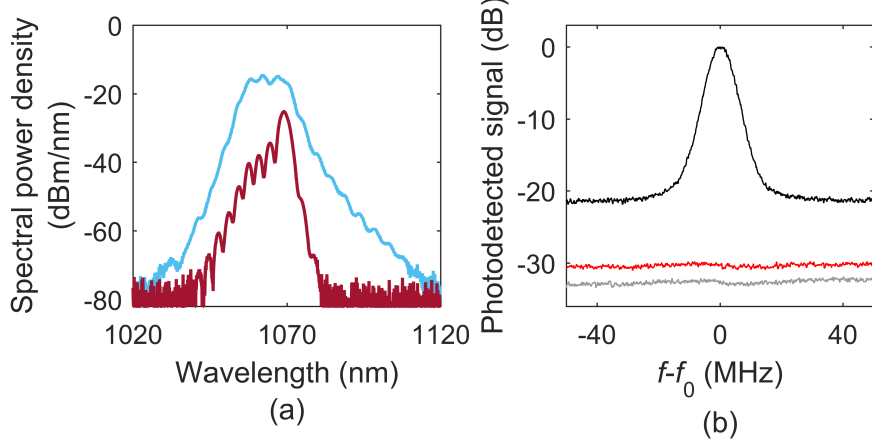


Figure 7.4: **Self-referencing of an EOM comb.** (a) Spectral components used for  $f - 2f$  self-referencing after passing through a 1070-nm optical bandpass filter: native supercontinuum light (blue) and frequency-doubled 2140-nm supercontinuum light (red). (b) Photodetected carrier-envelope offset frequency signal (black), along with a measurement of the intensity noise of the pulse train and the photodetector noise floor (grey). The frequency of the detected signal is  $f_0 = 706.6$  MHz.

### 7.3 Noise considerations in EOM comb generation

The repetition rate of an EOM comb is derived from a microwave source and is multiplied directly by a factor  $\mu$  to yield the frequency-comb mode with seed-laser-referenced mode number  $\mu$ . This is an important contrast with both modelocked-laser-based combs and microcombs, where generation of the comb in a resonant cavity dampens fast fluctuations of  $f_{rep}$ . In the EOM comb case, the contribution to the frequency noise of mode  $\mu$  from the microwave source scales with  $\mu$ ; the contribution to the power spectrum of frequency noise scales as  $\mu^2$ . This presents a challenge in the generation of the coherent octave-spanning supercontinuum spectrum required for  $f - 2f$  self-referencing, as the modes used for self-referencing are at the extreme ends of the supercontinuum where  $\mu$  is large. The factor by which the noise on the modulation tone  $f_{rep}$  is multiplied to determine its contribution to the noise on the measured carrier-envelope offset frequency is the ratio between the frequency  $f_c$  of the seed laser and the repetition rate. It is easiest to see this by recalling that the

carrier-envelope offset frequency, which is measured by  $f - 2f$  self-referencing, is  $f_0 = f_c - Nf_{rep}$ , where  $N$  is the largest integer such that  $f_0 > 0$ ; therefore  $\partial f_0 / \partial f_{rep} = -N$ .

For the 10 GHz comb discussed above the noise on  $f_{rep}$  contributes to the noise on  $f_0$  after multiplication by a factor  $N = f_c/f_{rep} \sim 19340$  (where  $f_c = 193.4$  THz for a 1550 nm seed laser). In Fig. 7.5a we plot this contribution to the spectrum of fluctuations the carrier-envelope offset frequency, as well as the contribution from the noise of the seed laser. The noise on  $f_{rep}$  results from technical noise on the synthesizer tone at low Fourier frequencies and approaches a white Johnson-Nyquist (thermal) phase-noise floor of -177 dBm/Hz at high Fourier frequencies. Noise in each of these regimes impacts the photodetected  $f_0$  signal: low-frequency noise contributes to the linewidth of the comb modes and therefore the  $f_0$  signal, while high-frequency noise contributes to a frequency-noise floor on the photodetected signal [140]. Unmitigated multiplication of this thermal floor by the factor  $N^2 = 19340^2$  leads to a supercontinuum with optical frequency fluctuations that are large enough to prevent detection and measurement of  $f_0$ ; this is evidenced by unsuccessful attempts we have made to measure  $f_0$  without the filter cavity in place.

Inclusion of the Fabry-Perot filter cavity in our system enables detection and measurement of  $f_0$ . We use a Fabry-Perot cavity with free-spectral range  $\sim 10$  GHz that is actively stabilized to the comb's mode spacing. Our filter cavity has linewidth 7.5 MHz; equivalently, it has finesse of  $\mathcal{F}=1333$ . The filter cavity's Lorentzian transfer function reduces the optical frequency fluctuations of the comb modes at high Fourier frequency—these fluctuations are averaged over the photon lifetime of the cavity. The effect of passing the comb through the cavity is demonstrated concretely in Fig. 7.5b, where we compare the lineshape of a heterodyne beat between the supercontinuum and a CW laser with 1319 nm wavelength with and without the filter cavity in place. The signal-to-noise ratios for the beat with and without the filter cavity are 40 dB and 17 dB, respectively.

The filter cavity reduces the frequency noise of  $f_0$  at Fourier frequencies outside of the cavity linewidth of 7.5 MHz. We explore the effect of fluctuations inside of the filter cavity's linewidth by changing the microwave source from which  $f_{rep}$  is derived. The  $f_0$  signal shown in Fig. 7.4b is acquired with a tunable commercial synthesizer providing  $f_{rep}$  after repetition-rate downsampling

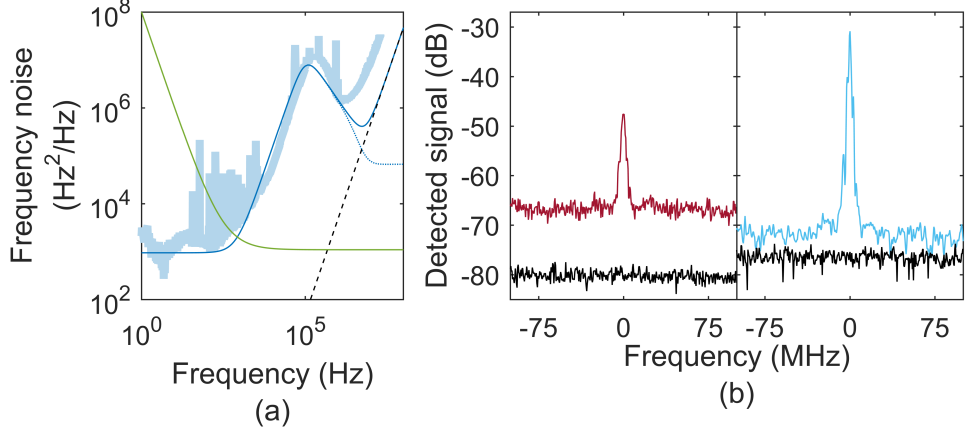


**Figure 7.5: Investigation of the noise properties of the EOM comb.** (a) Contributions to the frequency-noise spectrum of the carrier-envelope offset frequency: model of the seed laser based on past measurements (green), model of the 10 GHz synthesizer multiplied by  $19430^2$  without the filter cavity (solid blue, measurement thick blue), and synthesizer multiplied by  $19340^2$  and the Lorentzian filter-cavity transfer function (dotted blue). The synthesizer is modeled at high frequency by noise increasing as  $f^2$  (associated with a white phase-noise floor) that arises from Johnson-Nyquist noise with synthesizer power of -8 dBm. The thermal contribution alone is indicated by the dashed black line. (b) Comparison of the detected beats between the supercontinuum and a CW laser with 1319 nm wavelength without (red, left) and with (blue, right) the Fabry-Perot filter cavity. The level of intensity noise on the supercontinuum, measured by removing the 1319 nm CW laser, is shown by the lower gray trace in each plot; the elevated floor of the red trace relative to this background indicates that frequency noise is responsible for the reduced SNR of the beat without the filter cavity. Signal-to-noise ratios for the beat are 17 dB without and 40 dB with the filter cavity.

to 2.5 GHz. In Fig. 7.6 we show the detected  $f_0$  signal with three different sources for the 10 GHz repetition rate: 1. No downsampling, synthesizer at 10 GHz; 2. Dielectric-resonator oscillator; and 3. Sapphire oscillator. The  $f_0$  beat without downsampling with  $f_{rep}$  derived from the synthesizer has signal-to-noise ratio comparable to that of the  $f_0$  beat measured at 2.5 GHz repetition rate, but with higher intensity noise on the supercontinuum due to uncontrolled differences in the nonlinear spectral broadening. The other two sources have significantly less noise at low Fourier frequencies, and the effect of this lower noise is readily apparent in the reduced linewidth of the  $f_0$  signal. This indicates the importance of a high-performance microwave oscillator for future deployments of EOM combs. We emphasize that we have been unable to detect  $f_0$  without the filter cavity, even with  $f_{rep}$  derived from the sapphire oscillator. This is a confirmation that oscillator-independent thermal noise obscures  $f_0$  without the filter cavity in place.

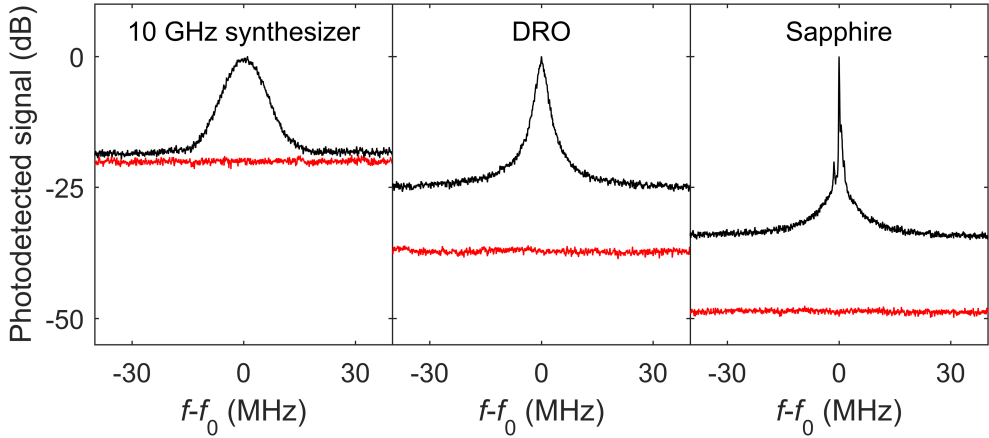


**Figure 7.6: Photodetected carrier-envelope-offset frequency signal with different sources for  $f_{rep}$ .** (a) The  $f_0$  beat with  $f_{rep}$  derived from a synthesizer;  $f_0 = 1.793$  GHz. (b) The same, with  $f_{rep}$  derived from a dielectric-resonator oscillator;  $f_0 = 491$  MHz. (b) The same, with  $f_{rep}$  derived from a sapphire oscillator,  $f_0 = 726$  MHz. Different  $f_0$  linewidths for different  $f_{rep}$  sources illustrate the effect of low-Fourier-frequency noise of  $f_{rep}$  on the frequency-noise characteristics of the EOM comb.

## 7.4 Application: Optical frequency division via double pinning

*Optical frequency division* (OFD) refers to the stabilization of a microwave frequency by locking it to a subharmonic of an optical frequency or frequency difference [8, 9]. This technique transfers the fractional frequency stability of the optical frequency to the microwave tone, and is a method for generation of stable microwaves that is competitive with all-electronic techniques. One method for OFD is to self-reference a frequency comb and lock  $f_0$  to a microwave reference, and then lock the beat between the comb and a stable optical frequency  $\nu_{opt}$  by feeding back to the repetition rate. An ideal lock transfers the noise on  $\nu_{opt}$  to the repetition rate with a division factor  $N$ , where the beat is taken between  $\nu_{opt}$  and mode  $N$  with frequency  $f_0 + Nf_{rep}$ . The repetition rate then acquires the fractional frequency stability of the optical reference.

A second method of performing OFD is *double pinning*, in which the comb is not self-referenced, but instead two optical references are used to control the two comb degrees of freedom  $f_{rep}$  and  $f_0$  [92, 141, 142]. As a demonstration of the utility of the EOM comb system, we perform OFD with double pinning using the EOM comb spectrum generated as described above.

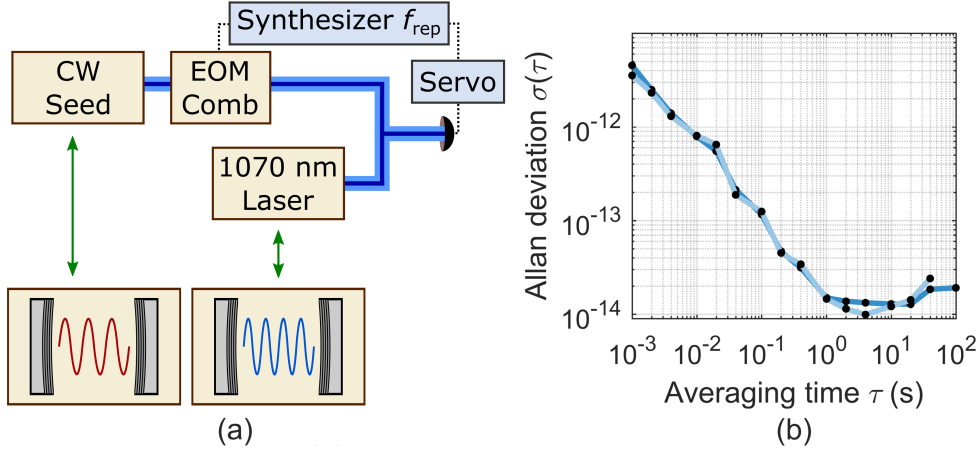


**Figure 7.7: Stable microwave generation with an EOM comb via double pinning.** (a) Experimental setup for double pinning of an EOM comb to two optical references. The seed laser for the EOM comb is locked to a stable reference cavity at 1550 nm, and a mode of the supercontinuum is locked to a second laser stabilized to a reference cavity at 1070 nm. The lock is achieved by feeding back to the synthesizer that generates  $f_{rep}$ . (b) Measurement of the Allan deviation of the repetition rate of the double-pinned EOM comb. The Allan deviation at 1 s averaging time is  $\sim 1.3 \times 10^{-14}$ , considerably better than what can be achieved by the synthesizer alone. At longer averaging times the frequency interval  $f_{1070} - f_{1550}$  begins to change due to thermal drift, so the Allan deviation increases.

For our OFD experiment, we generate the EOM comb using a seed laser with frequency  $f_{1550}$  that is locked to a stable reference cavity for 1550 nm wavelength. We also generate a second laser with frequency  $f_{1070}$  that is stabilized to a reference cavity for 1070 nm wavelength. After generating the EOM comb supercontinuum, we measure the frequency of the beat between a mode of the EOM comb with pump-referenced mode number  $\mu_b$  and frequency  $f_{\mu b} = f_{1550} + \mu_b f_{rep}$  and the cavity-stabilized 1070 nm laser. We lock this beat to a microwave reference with frequency  $f_{lock}$  by feeding back to the repetition rate of the EOM comb. This experimental setup is depicted schematically in Fig. 7.7a. The equation representing an ideal lock is:

$$0 = f_{1550} + \mu_b f_{rep} - f_{1070} - f_{lock}. \quad (7.5)$$

Then the fluctuations on the repetition rate are:

$$\delta f_{rep} = \delta(f_{1070} - f_{1550} + f_{lock})/\mu_b. \quad (7.6)$$

Thus, the fluctuations on the repetition rate are the worse of (a) the absolute fluctuations on  $f_b$

divided by  $\mu_b$  and (b) the fractional fluctuations on  $f_{1070} - f_{1550}$ , since  $f_{1070} - f_{1550} \sim \mu_b f_{rep}$ .

We characterize the output of this OFD scheme by photodetecting the repetition rate of the OFD-stabilized EOM comb and measuring its Allan deviation  $\sigma(\tau)$  [143]. The Allan deviation is the square root of the Allan variance  $\sigma^2(\tau)$ , which is defined as:

$$\sigma^2(\tau) = \frac{1}{2} \langle (\bar{y}_{n+1} - \bar{y}_n)^2 \rangle . \quad (7.7)$$

Here  $\langle g \rangle$  denotes the expectation value of  $g$ , which in practice is determined by recording many samples, and  $\bar{y}_n$  is the  $n^{\text{th}}$  fractional frequency average, where each average is over a time  $\tau$  and there is no dead time between them. The fractional frequency  $y$  is defined relative to a nominal frequency  $f_{nom}$ :  $y(t) = (f(t) - f_{nom})/f_{nom}$ .

We measure the Allan deviation of  $f_{rep}$  by measuring the difference between  $f_{rep}$  and a reference 10 GHz signal that is derived through OFD with a Ti:sapphire modelocked laser [9]; the reference is known to have Allan deviation significantly lower than what we measure, so we know that the observed Allan deviation is not limited by the noise-floor of the measurement. We plot the results of the measurement,  $\sigma(\tau)$  as a function of averaging time  $\tau$ , for two separate measurements in Fig. 7.7b. The observed Allan deviation at one second averaging time  $\sigma(\tau = 1 \text{ s}) \sim 1.3 \times 10^{-14}$  is significantly better than the level  $\sim 10^{-13}$  that is achieved by the synthesizer alone, using just the hydrogen maser at NIST as a reference.

## 7.5 Outlook

The EOM comb approach for frequency-comb generation yields combs that are widely tunable and that can be flexibly tailored for specific applications. Because the comb generation is a non-resonant process (up to the optional inclusion of a filter cavity), the comb properties can be manipulated in real time with speed and range that greatly exceeds the capabilities of mode-locked lasers (where repetition-rate adjustment requires manipulation of moving parts) and microcombs (where repetition-rate control via phase modulation as described in Chap. 3, for example, is limited to the locking range afforded by the resonator dispersion). This has allowed, for example, the proposal

and demonstration of ‘PHIRE’—Parallel Heterodyne Interferometry via Rep-rate Exchange—which is, essentially, dual-comb spectroscopy [11] with a single frequency comb whose repetition-rate is periodically switched [144].

EOM combs, with their lack of moving parts, also offer robust turn-key operation to a degree that is difficult to achieve with other comb sources. This has made them particularly promising for applications where long-term deployment with maximum up-time is important, such as calibration of astronomical spectrograms [145]. While the necessity of the filter cavity described here to enable  $f - 2f$  self-referencing is an apparent limitation, there are promising routes towards eliminating this requirement—using a high-power, tunable microwave oscillator could allow self-referencing of a repetition-rate-tunable EOM comb without a filter cavity.

## Chapter 8

### Downsampling of optical pulse trains

This chapter describes work that was reported in:

- Daniel C. Cole, Scott B. Papp, and Scott A. Diddams. Downsampling of optical frequency combs. *Journal of the Optical Society of America B* **35** (2018), 1666–1673.

This chapter presents a discussion of a technique for repetition-rate reduction of optical pulse trains. While high pulse train repetition rates are appealing for some applications, they are not always appropriate. For example, spectral resolution in spectroscopy applications is sacrificed in a comb with a large mode spacing, and a high repetition rate makes nonlinear optics less efficient at a given average power. This can present a barrier to the generation of octave-spanning spectra for  $f - 2f$  self-referencing. On the other hand, in general the size of the comb package sets the scale for the round-trip time, meaning that low-SWAP combs tend to have inherently high repetition rates. Therefore, to increase the flexibility of low-SWAP and high-repetition-rate comb systems in applications, a method for reducing the repetition rate of a pulse train will be useful.

Here I present an investigation of a method for pulse train repetition-rate reduction, or downsampling, in which an electro-optic gate realized by an RF-driven intensity modulator periodically transmits an incoming pulse at a frequency lower than the input repetition rate. The basic principle is illustrated in Fig. 8.1. Downsampling via pulse gating, also referred to as 'pulse picking' in the literature, has been used extensively in the context of high-field, phase-sensitive ultrafast optics for the generation of energetic, carrier-envelope-phase-stabilized ultrashort pulses [147, 148]. In this application, a comb with initial repetition rate in the  $\sim$ 100 MHz range that has already been self-referenced and stabilized is pulse-picked to a repetition rate on the order of 1-100 kHz. Concerns in

this application center around control and preservation of the carrier-envelope phase in the pulse-picking and amplification process [149, 150]. In contrast, the focus here is on downsampling within the context of optical metrology with frequency combs, and we are concerned with downsampling's effect on the optical phase noise, the pulse-to-pulse energy fluctuations, and the carrier-envelope offset frequency of the comb. In particular, it is important that the downsampled pulse train is suitable for  $f - 2f$  self-referencing.

Sec. 8.1 presents a proof-of-principle experiment in which a 250 MHz pulse train is downsampled to 25 MHz, and then spectrally broadened and self-referenced. A mathematical model of downsampling is presented in Sec. 8.2, and this model informs the discussion of downsampling's effect on the pulse train's noise properties presented in Sec. 8.3 and Sec. 8.4. In Sec. 8.5 I discuss some practical considerations in applications of the technique, including the effect of imperfections in the gating process such as incomplete extinction of rejected pulses.

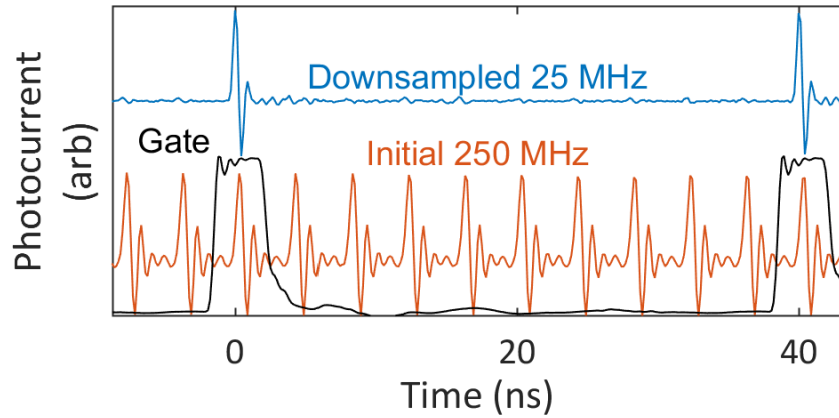


Figure 8.1: **An illustration of pulse-train repetition-rate downsampling.** Orange: A photodetected 250 MHz pulse train. Blue: A photodetected 25 MHz pulse train obtained by downsampling the 250 MHz pulse train by a factor of  $N = 10$ . Black: Oscilloscope trace showing the voltage sent to the RF port of a Mach-Zehnder intensity modulator to selectively transmit a subset of the incoming pulses. With the intensity modulator biased for zero transmission, the voltage trace is indicative of the transmission.

## 8.1 Proof-of-Concept Experiment

Here I present a proof-of-concept experiment in which a 250 MHz comb is downsampled and self-referenced. The setup for and results of this experiment are summarized in Fig. 8.2. Our pulse gating scheme, shown in Fig. 8.2a, employs a Mach-Zehnder (MZ) electro-optic intensity modulator driven by 25 MHz rectangular electronic gating pulses with 80 ps transitions and 3.5 ns duration. The electronic pulse generator and the repetition rate of the input 250 MHz comb are both referenced to a hydrogen maser to maintain synchronization. The DC bias of the intensity modulator is set for maximum extinction outside the electronic gate, whose amplitude is approximately matched to  $V_\pi$  of the EOM. This downsampling scheme results in a stable 25 MHz optical pulse train with >12 dB contrast (Fig. 8.1). This contrast is adequate for this experiment, but could be improved by cascading modulators with higher extinction ratios. The average power of the 250 MHz pulse train is reduced from 30 mW to 400  $\mu$ W by the pulse gating process and the insertion loss of the optical components. The pulse train is amplified to 35 mW by use of a normal-dispersion erbium-doped fiber amplifier, which provides some spectral broadening and temporal pulse compression [151]. An octave-spanning supercontinuum is obtained by launching the amplified, <100 fs,  $\sim$ 1 nJ pulses into 20 cm of highly nonlinear fiber (HNLF) [152]; the resulting spectrum is shown in Fig. 8.2b. For comparison, we also present the supercontinuum generated by the 250 MHz comb with the EOM set for constant maximum transmission under otherwise identical conditions. The 250 MHz comb is amplified by the same EDFA to an average power of 85 mW, corresponding to 340 pJ pulse energy, before it enters the HNLF.

To detect  $f_0$ , the octave-spanning supercontinuum shown in Fig. 8.2b is sent into a free-space  $f - 2f$  interferometer consisting of a half-wave plate and a periodically poled lithium niobate (PPLN) crystal quasi-phase-matched for second-harmonic generation at 1980 nm. The generated 990 nm light is shown in 8.2b. A 10 nm band-pass filter at 990 nm selects this second harmonic and the co-linear supercontinuum at 990 nm, which are then photodetected to observe  $f_0$  with 30 dB signal-to-noise ratio, shown in Fig. 8.2c. Fig. 8.2d shows a 2000 s record of  $f_0$  for the downsampled

comb.

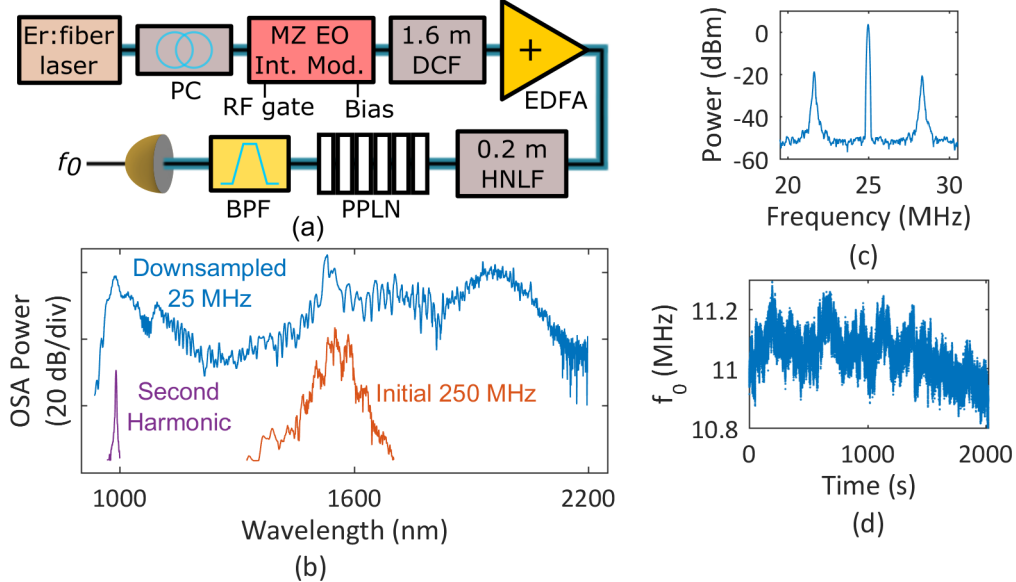


**Figure 8.2: Demonstration of downsampling for  $f_0$  detection.** (a) Schematic depiction of the setup for downsampling a 250 MHz Er:fiber comb and detecting the offset frequency of the resulting 25 MHz pulse train. PC—polarization controller. DCF—dispersion-compensating fiber. EDFA—erbium-doped fiber amplifier. HNLF—highly nonlinear fiber. PPLN—periodically-poled lithium niobate. BPF—(optical) band-pass filter. (b) Octave-spanning supercontinuum generated by downsampling (top, blue), second harmonic generated for  $f_0$  detection (purple), and for comparison the supercontinuum generated by the same apparatus without downsampling (orange). (c) Detected repetition rate and  $f_0$  beat at 100 kHz resolution bandwidth; signal-to-noise ratio of  $f_0$  is 30 dB. e) Counted frequency of the detected free-running offset beat. Data is taken for  $\sim 2000$  s at 10 ms gate time. The offset frequency of the 250 MHz commercial comb was adjusted between measurements shown in Figs. 8.2c and 8.2d to simplify electronic processing.

## 8.2 Mathematical model for downsampling

While Fig. 8.2 presents an absolute frequency measurement of  $f_0$  enabled by downsampling, it does not demonstrate the deterministic connection between the input and downsampled combs that is essential for applications. To understand this relationship, I present first a simple model of downsampling, and then experimental tests of its conclusions.

The downsampled pulse train's electric field is modeled as the product of the incoming comb's field and a time-varying amplitude modulation. For an incoming optical frequency comb with repetition rate  $f_{rep}$ , complex single-pulse field  $A(t)$  that is localized near  $t = 0$ , and pulse-to-pulse

carrier-envelope phase shift  $\phi$ , pulse gating by a train of rectangular pulses of length  $t_g$  and arrival rate  $f_g$  yields a downsampled comb with field

$$a(t) = [\Sigma_n A(t - n/f_{rep})e^{in\phi}] \times [\Sigma_m \text{Rect}((t - m/f_g)/t_g)] \quad (8.1)$$

where  $\text{Rect}(x)$  is the rectangle function, taking the value 1 for  $-1/2 \leq x \leq 1/2$  and 0 elsewhere. Indices  $n$  and  $m$  count the pulse number of the incoming pulse train and the electronic gate respectively. The optical spectrum of the downsampled pulse train  $a(t)$ , calculated via the convolution theorem for the Fourier transform, is:

$$\mathcal{F}\{a\}(f) \sim 4\pi f_{rep} \Sigma_{nm} \frac{1}{m} \mathcal{F}\{A\}(f_0 + nf_{rep}) \times \sin(\pi m t_g f_g) \delta(f - f_0 - nf_{rep} - mf_g) \quad (8.2)$$

where  $f_0 = f_{rep} \cdot \phi / 2\pi$  is the carrier-envelope offset frequency of the incoming comb and  $\delta$  is the Dirac delta function. The downsampled pulse train has spectral content at optical modes  $f_0 + nf_{rep}$ , as well as at intensity modulation sidebands whose frequency offsets  $mf_g$  are harmonics of the gating frequency. To avoid the generation of unwanted modulations, pulse gating at an integer sub-harmonic of the incoming repetition rate,  $f_g = f_{rep}/N$ , is essential. In this case superposition of the intensity modulation components created by pulse gating results in a downsampled frequency comb with a single mode spacing. Moreover, this model predicts that the offset frequency is preserved up to a reduction modulo the comb's new repetition rate.

Notably, for pulse gating at a sub-harmonic of the input comb's repetition rate, timing jitter of the electronic gate that is less than its duration does not contribute to noise on the downsampled comb. By modeling jitter as gate-to-gate arrival-time delays  $\Delta t_m$ , it can be shown that the downsampled comb's amplitude  $a(t)$  and spectrum  $F\{a\}(f)$  do not deviate from Eqn. 8.1 provided that:

- (1) The jitter is a sufficiently small  $|\Delta t_m| < t_g/2$ , i.e., that the optical and electronic pulses are always substantially overlapped, and (2) That the optical pulses are substantially shorter than the electrical pulses, which is true for most systems. Thus, in general we expect that the carrier-envelope offset frequency of the incoming comb is preserved by downsampling even with jitter on the gate signal.

### 8.3 Experimental investigation of the effect of downsampling on the pulse train's noise properties

We supplement the mathematical model presented above with an experimental investigation of the effects of downsampling on the noise properties of the pulse train. First we consider the effects of technical limitations to ideal downsampling, and then we discuss fundamental effects associated with aliasing of high-Fourier-frequency optical noise and shot noise.

We measure the phase-noise spectrum of the downsampled comb's repetition rate at different points in our apparatus, as shown in Fig. 8.3a. We also plot the phase noise of the 250 MHz comb, which has been shifted by  $-10\log_{10}(N^2) = -20$  dB to facilitate comparison [153], and the phase noise of the electronic gate. The downsampled frequency comb's phase-noise spectrum matches that of the 250 MHz comb except for a small increase at  $\sim 3$  kHz, likely corresponding to the corner in the gate generator's phase noise at the same frequency. The phase noise of the high- and low-frequency ends of the supercontinuum similarly matches the 250 MHz comb below 1 kHz. The higher phase noise in the supercontinuum beyond 1 kHz is above the measurement system's noise floor (including shot noise), despite the reduced optical power available after spectral filtering. This higher noise is likely due to noise generation processes in the HNLF, such as the conversion of amplitude fluctuations on input pulses to timing jitter in the supercontinuum [137].

The timing jitter of our gating pulse train is between 5 ps (obtained by integrating the phase noise plotted in Fig. 8.3 to 100 kHz) and 10 ps (extrapolating constant phase noise to the 12.5 MHz Nyquist frequency and integrating). These jitter values are small relative to the 4 ns repetition period of the incoming optical pulse train. As the repetition rate of the incoming optical pulse train increases to  $>10$  GHz, the gate duration must correspondingly decrease for single-pulse gating, and timing jitter on the gate may become a significant fraction of the gate duration. To explore the effects of timing jitter larger than our pulse generator's inherent 5 to 10 ps, we impose excess jitter on the gating signal. We modulate the relative timing between the gating signal and the incoming optical pulse train at a frequency of 5 MHz with an amplitude of 250 ps. The effect of this jitter is

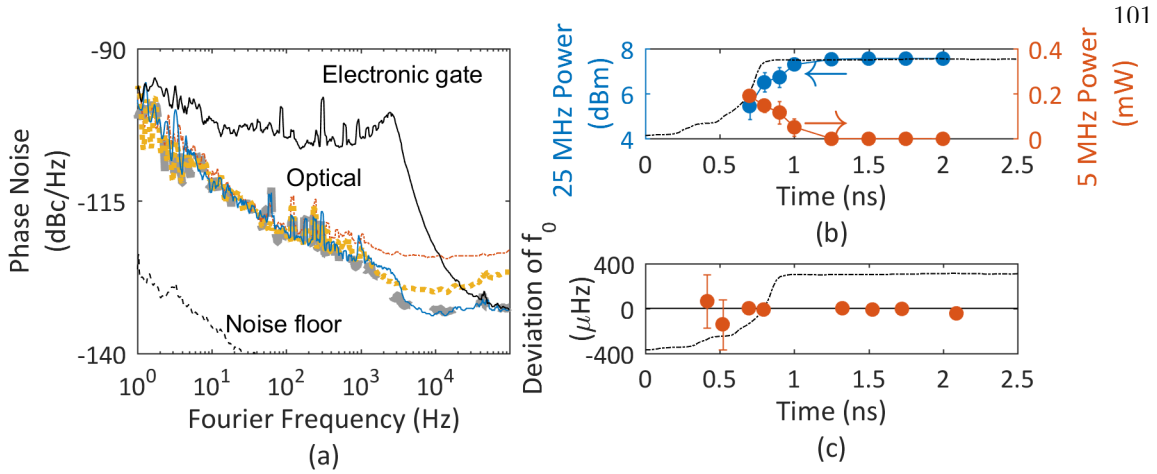


**Figure 8.3: Experimental investigation of noise introduced by downsampling.** (a) Measured repetition-rate phase noise of spectral components of the supercontinuum, selected by a  $990 \pm 5$  nm band-pass filter (dot-dashed orange), 1650 nm long pass filter (dotted yellow), and the entire downsampled 25 MHz frequency comb measured immediately before the EDFA (solid blue). Also shown is the phase noise of the electronic gate generator (top, solid black). (b) Amplitude of the downsampled pulse-train modulation due to 250 ps jitter at 5 MHz rate. The position of a data point on the x-axis indicates its mean position within the gate, shown in dashed black. Measurement uncertainties arise due to a latency between the optical trigger and the start of the electronic gating signal which varies on the order of 50 ps. (c) Deviation of the carrier-envelope offset frequency of the downsampled comb from the 250 MHz comb's offset frequency as a function of the alignment of optical pulses within the gate.

manifest in the microwave power of the gated comb as 5 MHz intensity-modulation sidebands whose amplitude depends on the position of the optical pulses within the gate, as shown in Fig. 8.3b. Pulses with a mean position within 250 ps of the gate edge are substantially modulated by the 5 MHz gate-delay signal. This agrees with the prediction of a sharp threshold on the acceptable level of timing jitter on the gate.

It is essential to establish that the comb's carrier-envelope offset frequency is preserved in the downsampling process. To do this, we perform a frequency comparison of the 25 MHz downsampled comb and a separate output of the 250 MHz comb. This 250 MHz output is intensity modulated so that a measurement of the nonzero optical heterodyne beat frequency between an intensity modulation sideband and a pulse-gating sideband of the downsampled comb reveals the relative frequency offset of the two combs. Figure 8.3c shows the null frequency shift between the 25 MHz and 250 MHz combs, which we have characterized for different alignments of the optical pulse within the

gate. At the level of several microhertz, better than  $10^{-18}$  relative to the 200 THz optical carrier frequency, we observe no frequency shift between the 250 MHz comb and the downsampled 25 MHz comb when the gate is properly aligned. This confirms the utility of downsampling for measurement of a high-repetition-rate comb's offset frequency for subsequent use of the comb in, for example, a spectroscopy experiment requiring high power per comb mode and high frequency precision.

#### 8.4 Effects of ideal downsampling on a pulse train's noise properties

In addition to the conversion of electronic technical noise to optical noise on the downsampled pulse train, there exists a further mechanism by which downsampling can change the measured amplitude noise properties of the pulse train. Even ideal downsampling, free of electronic noise, leads to an increase in the measured power spectral density (PSD) of optical pulse energy fluctuations (PEF) when technical pulse energy noise is present. This is due to aliasing of components of the PSD of pulse energy fluctuations at frequencies above the Nyquist frequency of the original pulse train,  $f_{rep}/2$ , when the Nyquist frequency is reduced to  $f_{rep}/2N$  by downsampling. Assuming random fluctuations from pulse to pulse, downsampling does not change the RMS fractional pulse energy fluctuation  $\sigma_{PEF}$ , whose square is equal to the frequency integral of the PSD of pulse energy fluctuations  $S_{PEF}(f)$ :

$$\sigma_{PEF}^2 = \int_0^{f_{rep}/2} df S_{PEF}(f). \quad (8.3)$$

---

Because the Nyquist frequency defines the upper limit for integration of  $S_{PEF}$ , in order for  $\sigma_{PEF}$  to be preserved  $S_{PEF}(f)$  must increase when the Nyquist frequency is reduced by downsampling. For example, in the simple case of white technical noise on the pulse energies with density  $S_o$ , we have

$$\sigma_{PEF}^2 = \int_0^{f_{rep}/2} df S_o = \int_0^{f_{rep}/2N} df S' \quad (8.4)$$

which shows that downsampling must increase the measured PSD of white technical noise from

$S_o$  to  $S' = NS_o$ , assuming there are no spectral correlations. However, this simple multiplicative increase is restricted to the case of white technical noise. In general, the PSD of pulse energy fluctuations of the new pulse train is determined from the original PSD through the usual method of modeling aliasing of a signal: a new Fourier frequency for each component of the original PSD is obtained by reducing the original Fourier frequency by a multiple of  $-f_{rep}/N$  so that it lies between  $-f_{rep}/2N$  and  $f_{rep}/2N$  and taking its absolute value. The new PSD is then determined by taking the quadrature sum of the PSD components at the same aliased Fourier frequency. This phenomenon is derived mathematically and demonstrated experimentally in Ref. [149], where the analysis of carrier-envelope phase noise applies equally well to pulse energy fluctuations.

In contrast with the increase in the PSD of pulse energy fluctuations arising from coincidence of the optical pulse with the edge of the electrical gate, which increases  $\sigma_{PEF}$ , the aliasing mechanism described above preserves  $\sigma_{PEF}$ . An important consequence of this is that while technical noise can lead to supercontinuum decoherence in external nonlinear spectral broadening, aliasing does not, because it is  $\sigma_{PEF}$  which determines the degree of supercontinuum decoherence. Thus the aliasing mechanism impedes  $f - 2f$  self-referencing only by reducing the available signal-to-noise ratio of an  $f_0$  signal in a straightforward linear fashion.

In practice, the relevance of the aliasing of the PSD of pulse energy fluctuations is determined by the presence of technical noise on the pulse energies at high Fourier frequency  $f > f_{rep}/2N$ . For sufficiently small downsampling factors (e.g.  $f_{rep}/2N \leq \sim 50MHz$ ) and depending on the comb source, it is possible that the only source of intensity noise at frequencies above  $f_{rep}/2N$  is shot noise. Shot noise results in a maximal (shot-noise-limited) signal-to-noise ratio (SNR) of an optical heterodyne beat with a local oscillator laser which is reduced by  $N^2$  (in electrical power units) as the average power of the pulse train is reduced by downsampling by a factor of  $N$ . In contrast, in the case of detection of a carrier-envelope-offset beat with fixed optical detection bandwidth, the shot-noise-limited SNR is preserved in downsampling. One way to understand these results is to model the shot noise at a given Fourier frequency as the incoherent sum of optical heterodyne beats between each optical comb mode and the uncorrelated vacuum fluctuations at the appropriate

optical frequency [154, 155], and to take into account the fact that during downsampling the optical power of each comb mode is reduced by  $N^2$ , with the first factor of  $N$  coming from reduction of the total optical power and the second factor of  $N$  due to the increase in the spectral density of comb modes.

We experimentally investigate the impact of downsampling on the PSD of pulse energy fluctuations by measuring noise on three photodetected optical signals: a shot-noise-limited telecom-band CW laser, a 10 GHz pulse train generated by passing this laser through cascaded optical phase and intensity modulators (see Chapter 7, [125]) and then a low-noise EDFA, and this pulse train after downsampling by a factor of four to 2.5 GHz repetition rate with no additional amplification after downsampling. Shown in Figure 8.4 are curves for each signal of the fluctuations  $\sqrt{S_I(f = 50 \text{ MHz})}$  in the detected photocurrent at a Fourier frequency of 50 MHz versus the total time-averaged detected photocurrent  $\langle I \rangle$  from the optical signal. To measure the scaling of noise with optical power, these curves are generated by beginning with an optical signal which yields more than 800  $\mu\text{A}$  of detected photocurrent and attenuating this signal before photodetection. The data indicate that both the pulse-generation process and the downsampling process contribute some amount of technical noise at 50 MHz Fourier frequency to the photocurrent, because the measured curves are well-modeled by a quadrature sum of a shot-noise contribution and a technical noise contribution. The contributions of these two types of noise can be determined because they scale differently with the photodetected power: shot noise obeys the relationship  $\sqrt{S_I(f = 50 \text{ MHz})} = \sqrt{2e \langle I \rangle}$ ,  $\langle I \rangle$  denoting the time-averaged photocurrent, while the technical-noise contribution arises from fluctuations in the expected photocurrent  $I(t)$  and scales linearly with the detected photocurrent. We observe that downsampling by a factor of four leads to a multiplication of the amplitude of the technical noise by a factor of  $\sim 1.7$  on the optical signal relative to the carrier, which due to finite noise bandwidth is somewhat less than the factor of two (four, in electrical power units) that would be expected for ideal downsampling by a factor of four in the presence of white technical noise. These results further demonstrate that, properly implemented, downsampling does not magnify noise on the pulse train to a degree that is prohibitive for applications.

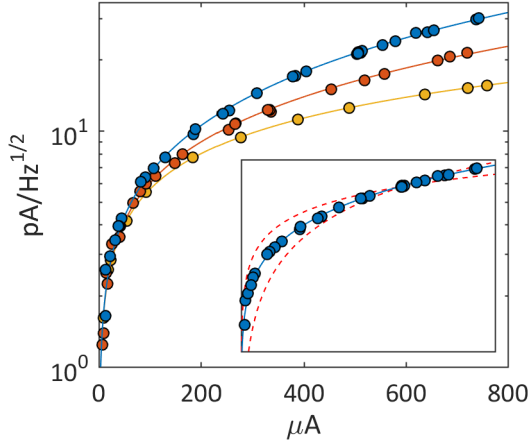


**Figure 8.4: Effect of downsampling on photocurrent fluctuations.** Fluctuations at 50 MHz Fourier frequency in the detected photocurrent as a function of the time-averaged photocurrent in three cases: CW laser at the shot-noise limit (lowest, yellow), 10 GHz pulse train (middle, red), and 2.5 GHz downsampled pulse train (highest, blue). Dots show measured data and curves show fits to the data. The fit for the shot-noise-limited laser has a single free parameter, which is a scaling factor of order 1 due to frequency dependence of the photodetector’s transimpedance gain. The fits for the pulse trains have a scaling factor in common, and have as an additional parameter the amplitude of the technical noise on the pulse train. This is -153.9 dBc/Hz for the 10 GHz pulse train and increases by a factor of  $\sim 1.72$  to -149.3 dBc/Hz for the 2.5 GHz downsampled pulse train. Inset: Optimized fits (dashed red) to the experimental data for the downsampled 2.5 GHz pulse train using only shot noise or linear technical noise scaling, demonstrating that both noise processes are important for explaining the data.

## 8.5 Model for the effect of incomplete extinction of rejected pulses and amplification of a downsampled pulse train

To this point, we have considered effects of downsampling assuming that extinction of the rejected pulses is complete, but in a practical application this is not necessarily the case. The modulators used for pulse extinction may transmit a substantial amount of energy from the rejected pulses—for example, one commercial manufacturer specifies 25 dB extinction ratio, and this number vary in practice. Additionally, the electronic gating signal may not have sufficient bandwidth to completely switch from transmission to extinction within the repetition period of the incoming pulse train, and initial extinction can be followed by some transmission caused by ringing in the gating signal. Bandwidth limitations will be increasingly likely as the repetition rates of frequency combs increase, placing more demanding requirements on gating electronics. Incomplete extinction

will add modulations to the optical spectrum and will raise the total power of the downsampled pulse train while keeping the energy of the fully-transmitted pulses fixed. This will require higher average power to achieve a given target pulse energy.

The effects of incomplete extinction of rejected pulses are exacerbated if the incomplete extinction does not happen in a deterministic and repetitive fashion; this could occur, for example, if intermediate pulses fall near the edge of the gate in the presence of relative timing jitter between the optical and electronic pulse trains, or if the extinction ratio fluctuates in time. Interestingly, if the downsampled pulse train is subsequently amplified and spectrally broadened, the impact of incomplete extinction depends on whether the optical amplifier used operates in the linear regime or in the saturated regime.

As an example, we consider the case where each fully transmitted pulse is preceded and followed by partially-extinguished pulses whose amplitudes fluctuate for each period of the downsampled pulse train. This fluctuation could occur because the pulses lie on the edge of the electronic gate and there is relative timing jitter between the optical pulse train and the gating signal. It is true that these fluctuations will lead to decoherence during nonlinear spectral broadening. However, the coherence is degraded by this mechanism only within the bandwidth that is achieved by the broadened, partially-extinguished pulses. In efficient  $f - 2f$  interferometry only the fully-transmitted pulses should reach an octave in bandwidth. Therefore, this mechanism of supercontinuum decoherence is not a problem in  $f - 2f$  interferometry in general, unless there is coupling between the amplitudes of the amplified partially-extinguished pulses and the amplified fully-transmitted pulses. This coupling can arise, for example, through amplification in the saturation regime, which then leads to decoherence across the full bandwidth of the supercontinuum.

To illustrate this point, we have performed numerical simulations of the spectral broadening of a 100 GHz train of 100 fs pulses which has been downsampled to 10 GHz and then amplified. We use an adaptive [156] split-step Fourier method [157] to simulate spectral broadening in 30 cm of HNLF according to the generalized nonlinear Schrodinger equation [40] (see Appendix B). In the simulation each fully-transmitted pulse, amplified to 1 nJ, is preceded and followed by partially-

extinguished pulses with normally distributed and uncorrelated energies with mean of 0.3 nJ and standard deviation of 0.225 nJ. This models the effect of adjacent pulses that coincide with the edge of the gate. We simulate amplification in two regimes: saturation is simulated using a fixed-energy method wherein the pulse energies in each three-pulse burst are rescaled by a common factor so that the total energy is 1.6 nJ; linear amplification is simulated using a fixed-gain model, which involves no such rescaling of pulses. Numerically, we simulate the spectral broadening of each pulse individually, which is acceptable because terms in the generalized nonlinear Schrodinger equation operate only locally or, in the case of the Raman term, on the timescale of several femtoseconds, while the separation between the pulses in each burst is 10 ps (the inverse of the initial 100 GHz repetition rate). We have verified that during simulated time-evolution each broadened pulse remains well-centered in its 5 ps simulation window.

Results of this study are shown in Figure 8.5. Figure 8.5a depicts a three-pulse burst before and after propagation in HNLF. In Figure 8.5b we show spectra corresponding to spectral broadening of this three-pulse burst, as well as plots of the spectral coherence averaged over many simulations. The first-order spectral coherence  $g_{12}^{(1)}(\lambda)$  is defined as:

$$\left| g_{12}^{(1)}(\lambda) \right| = \left| \frac{\langle E_1^*(\lambda) E_2(\lambda) \rangle}{\sqrt{\langle |E_1(\lambda)|^2 \rangle \langle |E_2(\lambda)|^2 \rangle}} \right| = \left| \frac{\langle E_1^*(\lambda) E_2(\lambda) \rangle}{\langle |E(\lambda)|^2 \rangle} \right|. \quad (8.5)$$

Curves are plotted for the fixed-gain and fixed-energy cases, as well as for the case with ideal downsampling (no partially-extinguished pulses) and only shot-noise on the pulse train. The averages in the formula above are over 1000 instantiations of the pair  $E_1$  and  $E_2$ , for a total of 2000 broadened spectra for each pulse within the burst of three. In both the fixed-gain and fixed-energy cases the coherence is poor in the center of the spectrum, but in the fixed-gain case, which models amplification in the linear regime, the coherence is preserved in the high- and low-frequency ends of the spectrum where it is needed for self-referencing.

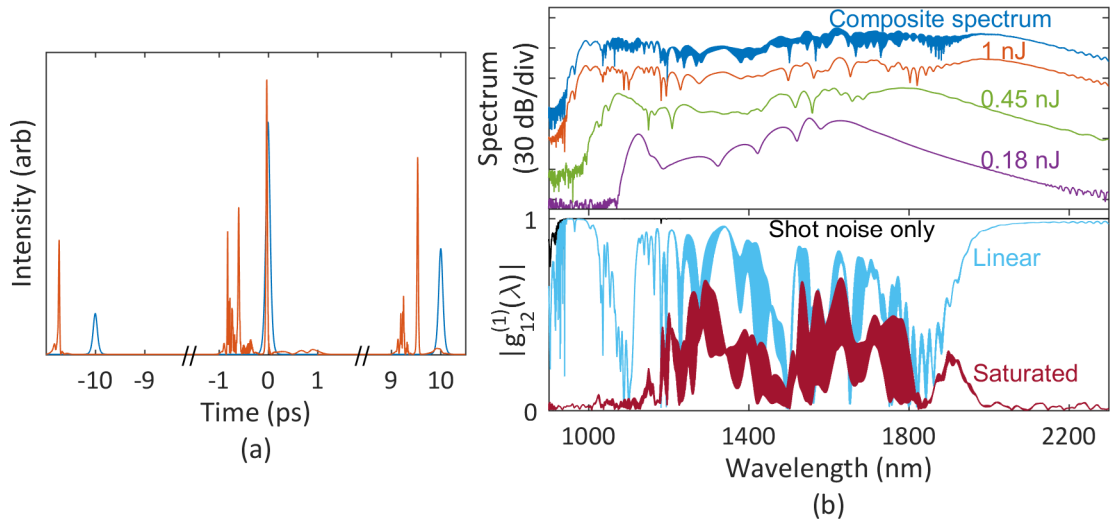


**Figure 8.5: Investigation of incomplete pulse extinction and amplification.** (a) A burst consisting of a fully-transmitted 1 nJ, 100 fs pulse and 100 fs partially-transmitted adjacent pulses with energies of 0.18 nJ and 0.45 nJ. Blue indicates initial  $\text{sech}^2$  pulses, and orange indicates the intensity after propagation through 30 cm HNLF. Note that the  $x$ -axis has been broken. (b) Top panel: optical spectra corresponding to the pulses shown in orange in (a), showing the composite spectrum of the three pulses (top, blue) and the spectra of the 1 nJ central pulse (second, orange), the 0.45 nJ adjacent pulse (third, green), and the 0.18 nJ adjacent pulse (bottom, purple). Bottom panel: Calculated spectral coherence averaged over 2000 simulations for the case of shot noise only (top, black) and for the case of fluctuating amplitudes of the first and third pulses as described in the text, after simulated amplification in a linear-regime optical amplifier (second, teal), and a saturated optical amplifier (bottom, maroon). For the case of linear-regime operation, high spectral coherence is preserved in the extreme ends of the supercontinuum even as it is lost in the center, in contrast with the complete loss of coherence after amplification in saturation.

## 8.6 Further remarks on the application of downsampling

Downsampling via pulse gating is a promising tool to manipulate high-repetition-rate frequency combs from low size, weight, and power packages and to aid in the detection of their offset frequencies. In our experiments downsampling enabled detection of  $f_0$  at a signal-to-noise ratio sufficient for measurement and stabilization, which otherwise would have required significantly higher average power. The effects of the electronic timing jitter of the gate signal are negligible so long as incoming optical pulses do not arrive coincidentally with the edge of the gate; when they do, timing jitter induces amplitude noise on the transmitted pulses. This results in an increase in RMS optical pulse energy fluctuations  $\sigma_{PEF}$ . Independently, the PSD of pulse energy fluctuations may be increased by aliasing of technical noise and by shot noise, depending on the relative magnitudes of these two

types of noise. Each of these sources of signal-to-noise-ratio degradation has the potential to interfere with detection of  $f_0$ . This investigation of these challenges will facilitate application of the technique in high-repetition-rate frequency comb systems. Importantly, our experiments demonstrated that downsampling does not add a significant amount of noise to the frequency components of the pulse train, and in a separate experiment the technique has recently been used successfully to detect the carrier-envelope offset frequency of a 10 GHz comb by downsampling by a factor of four ([126], see Chapter 7).

To employ downsampling as demonstrated here with repetition rates  $>10$  GHz will require electronic gates with duration  $\leq 100$  ps. Technology to downsample with gates as short as 20 ps is commercially available, while 100 Gb/s integrated circuits and 25 GHz demultiplexing have been demonstrated [158, 159]. Barring the use of such state-of-the-art electronics, pulse gates of duration longer than the incoming optical pulse train's repetition period can be employed. This will be technically easier to achieve, but will result in additional modulations on the spectrum of the downsampled pulse train.

The ambiguity of the input comb's offset frequency as a result of the reduction of the offset frequency modulo the new repetition rate makes downsampling most suitable for applications where the ambiguity can be removed by some other method. Two such applications are frequency comb calibration of astronomical spectrographs, where measurement of the wavelength of a comb mode can remove the ambiguity, and microresonator-based frequency combs, where the uncertainty in the offset frequency is determined by the frequency stability of the pump laser and can be much less than the repetition rate of the downsampled comb.

## Appendix A

### Derivation of the Lugiato-Lefever equation from the nonlinear Schrodinger equation

Here we show how the Lugiato-Lefever equation can be obtained by modeling propagation in a high-finesse ring cavity with the nonlinear Schrodinger equation and periodically applying an operator that implements in-coupling and out-coupling, including the effects of the round-trip phase shift associated with the detuning of the pump laser from a cavity mode. To my knowledge, the derivation given here was first performed by Haelterman, Trillo, and Wabnitz [59]. We use the NLSE for a pulse of restricted bandwidth such that higher-order nonlinearities are unimportant, but this derivation may also be carried out using a generalized nonlinear Schrodinger equation to include higher-order effects (e.g. Raman and self-steepening) in the LLE. Our equation is:

$$\frac{\partial A}{\partial z} = -\frac{\alpha_\ell}{2}A + i\gamma|A|^2A - i\frac{k''}{2}\frac{\partial^2 A}{\partial T^2}. \quad (\text{A.1})$$

This equation is ubiquitous in the study of pulse propagation in Kerr-nonlinear media, and a derivation of it is provided, for example, in Ref. [40]. As discussed in Sec. 2.3.3.1, it describes the evolution of a pulse envelope  $A$  in a ‘fast-time’ reference frame parametrized by  $T$  as it propagates in a Kerr-nonlinear medium, where the propagation distance is parametrized by the variable  $z$ . Here  $\gamma = \frac{2\pi}{\lambda} \frac{n_2}{A_{eff}}$  is the nonlinear coefficient of the medium, where  $n_2$  is the Kerr index,  $A_{eff}$  is the effective nonlinear mode area,  $\lambda$  the wavelength of the carrier wave, and  $k'' = \frac{\partial^2}{\partial \omega^2} \frac{n_{eff}(\omega)\omega}{c}$  is the GVD parameter. Propagation loss described by the coefficient  $\alpha_\ell$  has been included in Eq. A.1, with  $\alpha_\ell$  the loss coefficient in power (i.e.  $\partial P/\partial z = -\alpha_\ell P$ , where  $P = |A|^2$ ).

The dynamics in a ring resonator constructed of a Kerr medium can be described by evolving the field envelope  $A$  over a round trip of length  $L$  and then applying an operator that accounts for out-coupling of the circulating field  $A$  and in-coupling of a pump field  $A_{in}$ , as well as a round-trip phase shift  $\phi_{RT}$  associated with the detuning of the carrier frequency from a cavity mode. This allows us to advance the field at the end of the  $n^{\text{th}}$  round trip  $A_n(L, T)$  to the field  $A_{n+1}(0, T)$  at the beginning of the  $n + 1^{\text{th}}$  as:

$$A_{n+1}(0, T) = e^{i\phi_{RT}} \left( 1 - \frac{T_{RT}}{2\tau_{ext}} \right) A_n(L, T) + \sqrt{\frac{T_{RT}}{\tau_{ext}}} A_{in}, \quad (\text{A.2})$$

where  $\tau_{ext}$  describes in- and out-coupling as explained in Sec. 2.1.1 and  $T_{RT} = L/v_g$  is the round-trip time. If we define an operator  $G_L(A)$  that advances the field over a distance  $L$  according to Eq. A.1 as  $A(z + L, T) = G_L(A)A(z, T)$ , then we have:

$$A_{n+1}(0, T) = e^{i\phi_{RT}} \left( 1 - \frac{T_{RT}}{2\tau_{ext}} \right) G_L [A_n(0, T)] A_n(0, T) + \sqrt{\frac{T_{RT}}{\tau_{ext}}} A_{in}. \quad (\text{A.3})$$

The description of the field envelope in a Kerr-nonlinear ring cavity according to Eq. A.3 through iterated evolution according to the NLSE and then application of the in- and out-coupling operator is referred to as an Ikeda map [160]. We obtain the LLE by assuming that the operator  $G_L(A) \approx 1$ , that is, that the field does not evolve much over the round-trip length. This is equivalent to the assumption that the cavity length  $L$  is much less than the loss, nonlinear, and dispersion length scales  $L_\ell = 1/\alpha_\ell$ ,  $L_{NL} = 1/\gamma P_0$ , and  $L_D = T_0^2/|k''|$  over which the terms on the right-hand side of Eq. A.1 lead to appreciable evolution of the pulse envelope [40]. Here  $P_0$  and  $T_0$  are the peak power and temporal width, respectively, of a localized excitation in the pulse envelope  $A$ .

We can write the operator  $G_L$  explicitly as:

$$G_L(A) = \left[ 1 + L \left( -\alpha_\ell/2 + i\gamma|A|^2 - i\frac{k''}{2} \frac{\partial^2}{\partial T^2} \right) \right]. \quad (\text{A.4})$$

We assume that each term in this operator besides the identity term is small. If we note that the round-trip phase shift  $\phi_{RT}$  must also be small in a high-finesse cavity for appreciable build-up to occur, then we can expand the first term on the right-hand side of Eq. A.3 and retain only first

order terms to find:

$$A_{n+1}(0, T) = \left( 1 - \frac{T_{RT}}{2\tau_{ext}} + i\phi_{RT} - \frac{L\alpha_\ell}{2} + iL\gamma|A|^2 - iL\frac{k''}{2}\frac{\partial^2}{\partial T^2} \right) A_n(0, T) + \sqrt{\frac{T_{RT}}{\tau_{ext}}} A_{in}. \quad (\text{A.5})$$

By replacing  $n$  with the slow time  $t = nT_{RT}$  and allowing  $t$  to vary continuously we arrive at a Lugiato-Lefever equation, albeit in a different form from the one presented in Eq. 2.12:

$$T_{RT} \frac{\partial A}{\partial t} = \left( -T_{RT}/2\tau_{ext} + i\phi_{RT} - L\alpha_\ell/2 + iL\gamma|A|^2 - iL\frac{k''}{2}\frac{\partial^2}{\partial T^2} \right) A + \sqrt{\frac{T_{RT}}{\tau_{ext}}} A_{in}. \quad (\text{A.6})$$

To recast this equation in the standard form used in the body of this thesis, we first pass to the normalized temporal and spatial variables  $\tau$  and  $\theta$  and the parameters  $\alpha$  and  $\beta_2$ . We note that  $L\alpha_\ell/2 = T_{RT}/2\tau_{int}$  (as each describes the intrinsic loss over one round trip), and we define  $\theta = 2\pi T/T_{RT}$ , so that  $\frac{\partial^2}{\partial T^2} = \left(\frac{2\pi}{T_{RT}}\right)^2 \frac{\partial^2}{\partial \theta^2}$ . We divide by  $T_{RT}$  and obtain:

$$\frac{\partial A}{\partial t} = -\frac{\Delta\omega}{2} A + \frac{1}{T_{RT}} (i\phi_{RT} + iL\gamma|A|^2) A - i\frac{L}{T_{RT}} \left(\frac{2\pi}{T_{RT}}\right)^2 \frac{k''}{2} \frac{\partial^2 A}{\partial \theta^2} + A_{in}/\sqrt{T_{RT}\tau_{ext}} \quad (\text{A.7})$$

Dividing this by  $\Delta\omega/2$  brings us to the normalized temporal variable  $\tau = t/2\tau_{ph} = \Delta\omega t/2$ . The quantity  $\phi_{RT}/T_{RT}$  is exactly the frequency detuning  $\sigma = \omega_p - \omega_0$  between the pump laser and the cavity resonance frequency, so that the quantity  $2\phi_{RT}/T_{RT}\Delta\omega$  that results from division by  $\Delta\omega/2$  is simply equal to the normalized detuning term  $-\alpha = 2\sigma/\Delta\omega$ . Further, recalling from Sec. 2.2.1 that  $D_1 = 2\pi/T_{RT} = 2\pi v_g/L$  and  $D_2 = -D_1^2 v_g k''$ , we have:

$$\frac{L}{T_{RT}} \left(\frac{2\pi}{T_{RT}}\right)^2 \frac{k''}{2} = -D_2/2. \quad (\text{A.8})$$

Using the definition of the normalized dispersion for the LLE  $\beta_2 = -2D_2/\Delta\omega$  and combining these relations, we have:

$$\frac{\partial A}{\partial \tau} = -(1 + i\alpha)A + i\frac{2L\gamma}{T_{RT}\Delta\omega}|A|^2 A - i\frac{\beta_2}{2}\frac{\partial^2 A}{\partial \theta^2} + \sqrt{\frac{4\Delta\omega_{ext}}{T_{RT}\Delta\omega^2}} A_{in}, \quad (\text{A.9})$$

where we recall the definition  $\Delta\omega_{ext} = 1/\tau_{ext}$ . By defining  $\psi = \sqrt{\frac{2L\gamma}{T_{RT}\Delta\omega}} A$ , we arrive at the LLE as presented in Eq. 2.12:

$$\frac{\partial \psi}{\partial \tau} = -(1 + i\alpha)\psi + i|\psi|^2\psi - i\frac{\beta_2}{2}\frac{\partial^2 \psi}{\partial \theta^2} + F. \quad (\text{A.10})$$

Here the pump term has been normalized as:

$$F = A_{in} \sqrt{\frac{8L\gamma\Delta\omega_{ext}}{T_{RT}^2\Delta\omega^3}} \quad (\text{A.11})$$

$$= A_{in} \sqrt{\frac{8g_0\Delta\omega_{ext}}{\Delta\omega^3} \frac{1}{\hbar\omega_p}}, \quad (\text{A.12})$$

with

$$g_0 = n_2 c \hbar \omega_p^2 / n_g^2 V_0 \quad (\text{A.13})$$

as defined in Sec. 2.2.1, where  $V_0 = L A_{eff}$ . Assuming that  $A_{in}$  is real simply fixes the phase of  $\psi$ , which is otherwise arbitrary. With this assumption we have  $A_{in} = \sqrt{P_{in}}$ , and we recover the normalization from Sec. 2.2.1:

$$F = \sqrt{\frac{8g_0\Delta\omega_{ext}}{\Delta\omega^3} \frac{P_{in}}{\hbar\omega_p}}. \quad (\text{A.14})$$

### A.1 *A posteriori* confirmation that $L_D \gg L$ and $L_{NL} \gg L$ for LLE solitons

The analytical approximation to the soliton solution of the LLE presented in Eq. 2.27 has  $\theta$ -width  $\sqrt{\frac{-\beta}{2\alpha}}$ , and therefore temporal width  $T_0 = \frac{T_{RT}}{2\pi} \sqrt{\frac{-\beta}{2\alpha}}$ , and has approximate peak power  $2\alpha$ . Using the expressions presented above, one can calculate that for an LLE soliton the nonlinear length  $L_{NL} = 1/\gamma P_0$  and the dispersion length  $L_D = T_0/|k''|$  are the same, and depend on the detuning  $\alpha$ :

$$L_{NL} = L_D = \frac{v_g \tau_{ph}}{\alpha}. \quad (\text{A.15})$$

Using the definition of the cavity finesse  $\mathcal{F} = 2\pi\tau_{ph}/T_{RT}$ , we find that the ratio of these characteristic lengths to the cavity length is:

$$\frac{L_{NL}}{L} = \frac{L_D}{L} = \frac{\mathcal{F}}{2\pi\alpha}, \quad (\text{A.16})$$

and therefore that the assumption  $G_L \approx 1$  clearly holds for LLE solitons, since  $\mathcal{F} \gg 1$  for a high-finesse cavity and  $\alpha$  is of order 1 or 10.

## A.2 Normalization of the Ikeda map

For direct comparison of numerical results between the Ikeda map and the LLE, and also possibly for future work involving simulations of Kerr-combs outside of the high-finesse limit, it is useful to normalize the Ikeda map given in Eq. A.3 in the same way that the LLE is normalized. To conduct an Ikeda map calculation that corresponds to the LLE with parameters  $\alpha$ ,  $\beta_2$ , and  $F$ , it is natural to describe the Ikeda-map system by specifying two additional parameters: the resonator finesse  $\mathcal{F}$  and the coupling ratio  $\eta = \Delta\omega_{ext}/\Delta\omega$ . Then the following representations of the operators in Eq. A.3 can be used:

$$1 - \frac{T_{RT}}{2\tau_{ext}} = 1 - \frac{\pi\eta}{\mathcal{F}}, \quad (\text{A.17})$$

$$\sqrt{\frac{T_{RT}}{\tau_{ext}}} = \sqrt{\frac{2\pi\eta}{\mathcal{F}}}, \quad (\text{A.18})$$

$$e^{i\phi_{RT}} = e^{-i\frac{\pi}{\mathcal{F}}\alpha}, \quad (\text{A.19})$$

$$\frac{L\alpha_\ell}{2} = \frac{T_{RT}}{2\tau_{int}} = \frac{\pi(1-\eta)}{\mathcal{F}}. \quad (\text{A.20})$$

Using a normalized distance  $s = z \cdot \pi/\mathcal{F}L$  we define an operator  $G_1$  that advances the field  $\psi(s, \theta)$  a distance  $\Delta s = \pi/\mathcal{F}$  as  $G_1\psi(s, \theta) = \psi(s + \pi/\mathcal{F}, \theta)$  according to a nonlinear Schrodinger equation of the form:

$$\frac{\partial\psi}{\partial s} = -(1-\eta)\psi + i|\psi|^2\psi - i\frac{\beta_2}{2}\frac{\partial^2\psi}{\partial\theta^2}, \quad (\text{A.21})$$

where in general the operation is now performed continuously and not approximated as a single step as in the operator  $G_L$  above. The Ikeda map that is equivalent to the LLE with parameters  $\alpha$ ,  $\beta_2$  and  $F$  in the limit of high finesse is:

$$\psi_{n+1}(0, \theta) = e^{-i\frac{\pi}{\mathcal{F}}\alpha} \left(1 - \frac{\pi\eta}{\mathcal{F}}\right) G_1 [\psi_n(0, \theta)] \psi_n(0, \theta) + \sqrt{\frac{\pi}{2\mathcal{F}\eta}} F. \quad (\text{A.22})$$

The output  $\psi_n(0, \theta)$  of this Ikeda map can be directly compared to the output  $\psi(\theta, \tau)$  of the LLE at times  $\tau = \tau_n = n\pi/\mathcal{F}$ .

## Appendix B

### Numerical simulations of nonlinear optics

This appendix describes the algorithm used for numerical simulation of the generalized nonlinear Schrodinger equation (GNLSE) and Lugiato-Lefever equation (LLE) to obtain the results presented in the preceding chapters in this thesis. These equations are simulated with Matlab using a fourth-order Runge-Kutta interaction picture (RK4IP) method [157] with adaptive step size [156]. The RK4IP method is a particular algorithm in the broader class of split-step Fourier algorithms, in which nonlinearity is implemented in the time domain and dispersion is implemented in the frequency domain. An illustrative example of this split-step Fourier approach is a far simpler algorithm carried out with a single line of Matlab code to simulate the LLE:

```
psi=ifft(exp(delta*L).*fft(exp(delta*(1i*abs(psi).^2+F./psi)).*psi));
```

where `delta` is the step size and `L` is a linear frequency-domain dispersion operator ( $\hat{L}$ , see below) that has been defined in the preceding code. The RK4IP algorithm with adaptive step size is advantageous over this simple algorithm in calculation time and in the scaling of error with the step size.

#### B.1 RK4IP algorithm

The LLE (NLSE) describes the evolution of the field  $\psi$  ( $A$ ), a function of a fast variable  $\theta$  ( $T$ ), over a timescale parametrized by a slow variable  $\tau$  ( $z$ ). In what immediately follows we use the variable names corresponding to the LLE for simplicity. Each of these equations can be written as the sum of a nonlinear operator  $\hat{N}$  and a linear operator  $\hat{L}$  acting on  $\psi$ , so that the field  $\psi$  evolves

as

$$\frac{\partial \psi}{\partial \tau} = (\hat{N} + \hat{L})\psi, \quad (\text{B.1})$$

which can be implemented with the split-step Fourier approach.

The RK4IP algorithm specifies a recipe for advancing the field a single step  $\delta$  in the slow variable  $\tau$  to obtain  $\psi(\theta, \tau + \delta)$  from  $\psi(\theta, \tau)$ . This specific algorithm has the attractive feature that it reduces the number of Fourier transformations that must be performed to achieve a given calculation accuracy relative to other common algorithms. The RK4IP algorithm is[157]:

$$\psi_I = \exp\left(\frac{\delta}{2}\hat{L}\right)\psi(\theta, \tau) \quad (\text{B.2})$$

$$k_1 = \exp\left(\frac{\delta}{2}\hat{L}\right)\left[\delta\tau\hat{N}(\psi(\theta, \tau))\right]\psi(\theta, \tau) \quad (\text{B.3})$$

$$k_2 = \delta\hat{N}(\psi_I + k_1/2)[\psi_I + k_1/2] \quad (\text{B.4})$$

$$k_3 = \delta\hat{N}(\psi_I + k_2/2)[\psi_I + k_2/2] \quad (\text{B.5})$$

$$k_4 = \delta\hat{N}\left(\exp\left(\frac{\delta}{2}\hat{L}\right)(\psi_I + k_3)\right) \quad (\text{B.6})$$

$$\times \exp\left(\frac{\delta}{2}\hat{L}\right)(\psi_I + k_3) \quad (\text{B.7})$$

$$\psi(\theta, \tau + \delta) = \exp\left(\frac{\delta}{2}\hat{L}\right)[\psi_I + k_1/6 + k_2/3 + k_3/3 + k_4/6]. \quad (\text{B.8})$$

In the above it is understood that  $\hat{L}$  is applied in the frequency domain and  $\hat{N}$  is applied in the time domain. Calculation of  $\psi(\theta, \tau + \delta)$  from  $\psi(\theta, \tau)$  therefore requires eight Fourier transformations.

## B.2 Adaptive step-size algorithm

An adaptive step-size algorithm is a strategy for adjusting the magnitude of the steps  $\delta$  that are taken to optimize the simulation speed while maintaining a desired degree of accuracy. The RK4IP algorithm exhibits error that scales locally as  $O(\delta^5)$ . Since reducing the step size naturally requires more steps and therefore increases the number of small errors that accumulate, the resulting global accuracy of the algorithm is  $O(\delta^4)$ . One appropriate step-size adjustment algorithm for this scaling is described by Heidt [156]. For a given goal error  $e_G$ , the algorithm goes as follows:

- Calculate a field  $\psi_{coarse}$  by advancing the field  $\psi(\theta, \tau)$  according to RK4IP by a step of size  $\delta$ .
- Calculate a field  $\psi_{fine}$  by advancing the field  $\psi(\theta, \tau)$  according to RK4IP by two steps of size  $\delta/2$ .
- Calculate the measured error  $e = \sqrt{\sum_j |\psi_{coarse,j} - \psi_{fine,j}|^2 / \sum_j |\psi_{fine,j}|^2}$ , where  $j$  indexes over the discrete points parametrizing the fast variable  $\theta$ .
  - \* If  $e > 2e_G$ , discard the solution and repeat the process with coarse step size  $\delta' = \delta/2$ .
  - \* If  $e_G < e < 2e_G$ , the evolution continues and the step size is reduced to  $\delta' = \delta/2^{1/5} \approx 0.87\delta$ .
  - \* If  $e_G/2 < e < e_G$ , the evolution continues and the step size is not changed.
  - \* If  $e < e_G/2$ , the evolution continues and the step size is increased to  $\delta' = 2^{1/5}\delta \approx 1.15\delta$ .

When the simulation continues, the new field  $\psi(\theta, \tau+\delta)$  is taken to be  $\psi(\theta, \tau+\delta) = 16\psi_{fine}/15 - \psi_{coarse}/15$ . In the calculations described in this thesis, the goal error  $e_G$  is typically  $10^{-6}$ .

### B.3 Pseudocode for numerical simulation with the RK4IP algorithm and adaptive step size

The pseudocode shown in Algorithm 1 shows how the RK4IP algorithm with adaptive step size is implemented. This pseudocode neglects the specific details of the RK4IP algorithm.

Two notes:

- The current field  $\psi(\theta, \tau)$  is stored until the approximation to the new field  $\psi(\theta, \tau + \delta)$  is found to be acceptable.
- This implementation makes use of an extra efficiency that is possible when the solution is discarded and the step size is halved: the first step of the fine solution  $\psi_{fine,1}$  for the previous attempt becomes the coarse solution  $\psi_{coarse}$  for the current attempt.

---

**Algorithm 1** Pseudocode showing the implementation of RK4IP with adaptive step size.

---

```

procedure
  while  $\tau < \tau_{end}$  do
     $e = 1$                                  $\triangleright$  Initialize the error to a large value
     $firsttry = TRUE$                        $\triangleright$  For more efficiency if this is not the first attempt (see below)
     $\delta = 2\delta$                           $\triangleright$  To account for halving on the first iteration

    while  $e > 2e_G$  do
      if  $firsttry$  then
         $\psi_{coarse} = \text{RK4IP}(\psi, \delta)$ 
      else
         $\psi_{coarse} = \psi_{fine,1}$             $\triangleright$  We get to re-use the first step of the previous attempt's fine solution

       $\delta = \delta/2$ 
       $\psi_{fine} = \psi$ 

      for  $jstep = 1 : 2$  do
         $\psi_{fine} = \text{RK4IP}(\psi_{fine}, \delta)$ 
        if  $jstep = 1$  then
           $\psi_{fine,1} = \psi_{fine}$ 

       $e = \sqrt{\sum |\psi_{coarse} - \psi_{fine}|^2 / \sum |\psi_{fine}|^2}$ 
       $firsttry = FALSE$ 

       $\psi = 16\psi_{fine}/15 - \psi_{coarse}/15$ 
       $\tau = \tau + 2\delta$                       $\triangleright$  We took two fine steps of size  $\delta$ 

      if  $e > e_G$  then
         $\delta = \delta/2^{1/5}$ 
      if  $e < e_G/2$  then
         $\delta = 2^{1/5}\delta$ 

```

---

### B.3.1 Simulation of the LLE

For simulation of the LLE, the operators are:

$$\hat{N} = i|\psi|^2 + F/\psi, \quad (\text{B.9})$$

$$\hat{L} = -(1 + i\alpha_\mu), \text{ where} \quad (\text{B.10})$$

$$\alpha_\mu = \alpha - \sum_{n=1}^N \beta_n \mu^n / n!. \quad (\text{B.11})$$

The subscript  $\mu$  indicates the pump-referenced mode number upon which the operator acts. Note, in particular, that the pump term  $F$  has been incorporated into the nonlinear operator, so that it is implemented in the time domain. The quantity  $\hat{N}\psi$  then becomes  $i|\psi|^2\psi + F$ , as required for computation of  $\partial\psi/\partial\tau$ .

### B.3.2 Simulation of the GNLSE

In addition to self-phase modulation, the GNLSE used in the simulations conducted for Chapter 8 contains nonlinear terms that describe the medium's Raman response and self-steepening. The equation employed can be written as [40, 157]:

$$\frac{\partial A}{\partial z} = - \left( \sum_n k^{(n)} \frac{i^{n-1}}{n!} \frac{\partial^n}{\partial T^n} \right) A + i\gamma \left( 1 + \frac{1}{\omega_0} \frac{\partial}{\partial T} \right) \times \left( (1 - f_R)A|A|^2 + f_R A \int_0^\infty h_R(\tau) |A(z, T - \tau)|^2 d\tau \right). \quad (\text{B.12})$$

For Chapter 8, second- and third-order dispersion is used with  $k^{(2)} = -7.7 \text{ ps}^2/\text{km}$  and  $k^{(3)} = 0.055 \text{ ps}^3/\text{km}$ , where  $k^{(n)}$  is the  $n^{\text{th}}$  frequency-derivative of the propagation constant. The nonlinear coefficient  $\gamma = \frac{2\pi}{\lambda} \frac{n_2}{A_{\text{eff}}}$  used is 11 W/km [152], coming from an effective mode-field diameter of  $\sim 3.5 \mu\text{m}$  for the HNLF used in the experiment and the nonlinear index  $n_2 = 2.7 \times 10^{-16} \text{ cm}^2/\text{W}$  of silica. The quantity  $\omega_0 = 2\pi c/\lambda_0$  is the (angular) carrier frequency of the pulse, and the parameter  $f_R = 0.18$  and function

$$h_R(\tau > 0) = (\tau_1^2 + \tau_2^2)/(\tau_1 \tau_2^2) \times e^{-\tau/\tau_2} \sin \tau/\tau_1 \quad (\text{B.13})$$

describe the medium's Raman response, with  $\tau_1 = 12.2 \text{ fs}$  and  $\tau_2 = 32 \text{ fs}$  used here [40, 157, 161].

The linear frequency-domain operator applied in the RK4IP algorithm is

$$\hat{L} = i \frac{k^{(2)}}{2} (\omega_\mu - \omega_0)^2 - \frac{k^{(3)}}{6} (\omega_\mu - \omega_0)^3 \quad (\text{B.14})$$

Here  $\omega_\mu$  is defined by the discretization of the frequency domain due to Fourier-transformation of a finite temporal window of length  $T_{\text{comp}}$  via  $\omega_\mu = \omega_0 + 2\pi\mu/T_{\text{comp}}$ ; where  $T_{\text{comp}}$  is the size of the domain for the fast time variable  $T$ .

The nonlinear operator  $\hat{N}$  for the GNLSE implements the convolution as a product in the frequency domain. That is,

$$\hat{N} = i\gamma \frac{1}{A} \left( 1 + \frac{1}{\omega_0} \frac{\partial}{\partial T} \right) \times \left[ (1 - f_R)A|A|^2 + f_R A \mathcal{F}^{-1} \{ \chi_R \cdot \mathcal{F}(|A|^2) \} \right], \quad (\text{B.15})$$

where  $\chi_R = \mathcal{F}\{h_R(\tau)\}$  and  $\mathcal{F}$  denotes Fourier transformation. Procedurally, the quantity in the

square brackets is calculated first, and then the fast-time derivative is implemented and the sum in the curved brackets is calculated.

## References

- [1] Scott A. Diddams, David J. Jones, Jun Ye, Steven T. Cundiff, John L. Hall, Jinendra K. Ranka, Robert S. Windeler, Ronald Holzwarth, Thomas Udem, and T. W. Hänsch. Direct link between microwave and optical frequencies with a 300 THz femtosecond laser comb. *Physical Review Letters* **84** (2000), 5102–5105 (cited on page 1).
- [2] David J. Jones, Scott A. Diddams, Jinendra K. Ranka, Andrew Stentz, Robert S. Windeler, John L. Hall, and Steven T. Cundiff. Carrier-Envelope Phase Control of Femtosecond Mode-Locked Lasers and Direct Optical Frequency Synthesis. *Science* **288** (2000), 635–639 (cited on page 1).
- [3] Th. Udem, R. Holzwarth, and T. W. Hänsch. Optical frequency metrology. *Nature* **416** (2002), 233–237 (cited on page 1).
- [4] John L. Hall. Nobel lecture: Defining and measuring optical frequencies. *Reviews of Modern Physics* **78** (2006), 1279–1295 (cited on page 1).
- [5] Theodor W. Hänsch. Nobel lecture: Passion for precision. *Reviews of Modern Physics* **78** (2006), 1297–1309 (cited on page 1).
- [6] Jinendra K. Ranka, Robert S. Windeler, and Andrew J. Stentz. Visible continuum generation in air–silica microstructure optical fibers with anomalous dispersion at 800 nm. *Optics Letters* **25** (2000), 25 (cited on page 1).
- [7] S. A. Diddams, Th. Udem, J. C. Bergquist, E. A. Curtis, R. E. Drullinger, L. Hollberg, W. M. Itano, W. D. Lee, C. W. Oates, K. R. Vogel, and D. J. Wineland. An Optical Clock Based on a Single Trapped  $^{199}\text{Hg}^+$  Ion. *Science* **293** (2001), 825–828 (cited on page 1).
- [8] J. J. McFerran, E. N. Ivanov, A. Bartels, G. Wilpers, C. W. Oates, S. A. Diddams, and L. Hollberg. Low-noise synthesis of microwave signals from an optical source. *Electronics Letters* **41** (2005), 650–651 (cited on pages 1, 91).
- [9] T. M. Fortier, M. S. Kirchner, F. Quinlan, J. Taylor, J. C. Bergquist, T. Rosenband, N. Lemke, A. Ludlow, Y. Jiang, C. W. Oates, and S. A. Diddams. Generation of ultrastable microwaves via optical frequency division. *Nature Photonics* **5** (2011), 425–429 (cited on pages 1, 91, 93).
- [10] Scott A. Diddams, Leo Hollberg, and Vela Mbele. Molecular fingerprinting with the resolved modes of a femtosecond laser frequency comb. *Nature* **445** (2007), 627–630 (cited on page 1).
- [11] Ian Coddington, Nathan Newbury, and William Swann. Dual-comb spectroscopy. *Optica* **3** (2016), 414–426 (cited on pages 1, 94).

- [12] Steven T. Cundiff and Andrew M. Weiner. Optical arbitrary waveform generation. *Nature Photonics* **4** (2010), 760–766 (cited on page 1).
- [13] Tilo Steinmetz, Tobias Wilken, Constanza Araujo-Hauck, Ronald Holzwarth, Theodor W Hänsch, Luca Pasquini, Antonio Manescau, Sandro D’Odorico, Michael T Murphy, Thomas Kentischer, Wolfgang Schmidt, and Thomas Udem. Laser frequency combs for astronomical observations. *Science* **321** (2008), 1335–1337 (cited on page 1).
- [14] Brian R. Washburn, Scott A. Diddams, Nathan R. Newbury, Jeffrey W. Nicholson, Man F. Yan, and Carsten G. Jørgensen. Phase-locked, erbium-fiber-laser-based frequency comb in the near infrared. *Optics Letters* **29** (2004), 250–252 (cited on page 1).
- [15] Christoph Gohle, Thomas Udem, Maximilian Herrmann, Jens Rauschenberger, Ronald Holzwarth, Hans A. Schuessler, Ferenc Krausz, and Theodor W. Hänsen. A frequency comb in the extreme ultraviolet. *Nature* **436** (2005), 234–237 (cited on page 1).
- [16] Scott A. Diddams. The evolving optical frequency comb [Invited]. *Journal of the Optical Society of America B* **27** (2010), B51–B62 (cited on page 1).
- [17] Jerome Faist, Gustavo Villares, Giacomo Scalari, Markus Rosch, Christopher Bonzon, Andreas Hugi, and Mattias Beck. Quantum Cascade Laser Frequency Combs. *Nanophotonics* **5** (2016), 272–291 (cited on page 1).
- [18] Daryl T. Spencer, Tara Drake, Travis C. Briles, Jordan Stone, Laura C. Sinclair, Connor Fredrick, Qing Li, Daron Westly, B. Robert Ilic, Aaron Bluestone, Nicolas Volet, Tin Komljenovic, Lin Chang, Seung Hoon Lee, Dong Yoon Oh, Myoung-gyun Suh, Ki Youl Yang, Martin H. P. Pfeiffer, Tobias J. Kippenberg, Erik Norberg, Luke Theogarajan, Kerry Vahala, Nathan R. Newbury, Kartik Srinivasan, John E. Bowers, Scott A. Diddams, and Scott B. Papp. An optical-frequency synthesizer using integrated photonics. *Nature* **557** (2018), 81–85 (cited on pages 6, 34).
- [19] Travis C. Briles, Jordan R. Stone, Tara E. Drake, Daryl T. Spencer, Connor Frederick, Qing Li, Daron A. Westly, B. Robert Ilic, Kartik Srinivasan, Scott A. Diddams, and Scott B. Papp. Kerr-microresonator solitons for accurate carrier-envelope-frequency stabilization. *arXiv* (2017), 1711.06251 (cited on pages 6, 7, 34).
- [20] Robert W. Boyd. **Nonlinear Optics**. San Diego, CA: Elsevier, 2003 (cited on pages 7, 17).
- [21] T. M. Fortier, David J. Jones, and S. T. Cundiff. Phase stabilization of an octave-spanning Ti:sapphire laser. *Optics Letters* **28** (2003), 2198–2200 (cited on page 7).
- [22] David R. Carlson, Daniel D. Hickstein, Alex Lind, Stefan Droste, Daron Westly, Nima Nader, Ian Coddington, Nathan R. Newbury, Kartik Srinivasan, Scott A. Diddams, and Scott B. Papp. Self-referenced frequency combs using high-efficiency silicon-nitride waveguides. *Optics Letters* **42** (2017), 2314–2317 (cited on page 7).
- [23] David S. Hum and Martin M. Fejer. Quasi-phasematching. *Comptes Rendus Physique* **8** (2007), 180–198 (cited on page 8).

- [24] P. Del'Haye, A. Schliesser, O. Arcizet, T. Wilken, R. Holzwarth, and T. J. Kippenberg. Optical frequency comb generation from a monolithic microresonator. *Nature* **450** (2007), 1214–1217 (cited on pages 9, 18).
- [25] T. J. Kippenberg, R. Holzwarth, and S. A. Diddams. Microresonator-Based Optical Frequency Combs. *Science (New York, N.Y.)* **332** (2011), 555–559 (cited on pages 9, 18).
- [26] A. A. Savchenkov, A. B. Matsko, and L. Maleki. On Frequency Combs in Monolithic Resonators. *Nanophotonics* **5** (2016), 363–391 (cited on page 9).
- [27] Yanne K. Chembo. Kerr optical frequency combs: Theory, applications and perspectives. *Nanophotonics* **5** (2016), 214–230 (cited on page 9).
- [28] Alessia Pasquazi, Marco Peccianti, Luca Razzari, David J. Moss, Stéphane Coen, Miro Erkintalo, Yanne K. Chembo, Tobias Hansson, Stefan Wabnitz, Pascal Del'Haye, Xiaoxiao Xue, Andrew M. Weiner, and Roberto Morandotti. Micro-combs: A novel generation of optical sources. *Physics Reports* **729** (2017), 1–81 (cited on page 9).
- [29] Hansuek Lee, Tong Chen, Jiang Li, Ki Youl Yang, Seokmin Jeon, Oskar Painter, and Kerry J. Vahala. Chemically etched ultrahigh-Q wedge-resonator on a silicon chip. *Nature Photonics* **6** (2012), 369–373 (cited on pages 9, 11, 39, 48).
- [30] Xu Yi, Qi-Fan Yang, Ki Youl Yang, Myoung-Gyun Suh, and Kerry Vahala. Soliton frequency comb at microwave rates in a high-Q silica microresonator. *Optica* **2** (2015), 1078–1085 (cited on pages 9, 34, 53).
- [31] Pascal Del'Haye, Scott A. Diddams, and Scott B. Papp. Laser-machined ultra-high-Q microresonators for nonlinear optics. *Applied Physics Letters* **102** (2013), 221119 (cited on pages 9, 12, 48).
- [32] W. Liang, A. A. Savchenkov, A. B. Matsko, V. S. Ilchenko, D. Seidel, and L. Maleki. Generation of near-infrared frequency combs from a MgF<sub>2</sub> whispering gallery mode resonator. *Optics Letters* **36** (2011), 2290–2292 (cited on page 9).
- [33] Anatoliy A. Savchenkov, Andrey B. Matsko, Vladimir S. Ilchenko, Iouri Solomatine, David Seidel, and Lute Maleki. Tunable optical frequency comb with a crystalline whispering gallery mode resonator. *Physical Review Letters* **101** (2008), 093902 (cited on page 9).
- [34] Yoshitomo Okawachi, Kasturi Saha, Jacob S. Levy, Y. Henry Wen, Michal Lipson, and Alexander L. Gaeta. Octave-spanning frequency comb generation in a silicon nitride chip. *Optics Letters* **36** (2011), 3398–3400 (cited on page 9).
- [35] D. J. Moss, R. Morandotti, A. L. Gaeta, and M. Lipson. New CMOS-compatible platforms based on silicon nitride and Hydex for nonlinear optics. *Nature Photonics* **7** (2013), 597–607 (cited on page 9).
- [36] Danielle Braje, Leo Hollberg, and Scott Diddams. Brillouin-Enhanced Hyperparametric Generation of an Optical Frequency Comb in a Monolithic Highly Nonlinear Fiber Cavity Pumped by a cw Laser. *Physical Review Letters* **102** (2009), 193902 (cited on pages 10, 66, 78).

- [37] Ewelina Obrzud, Steve Lecomte, and Tobias Herr. Temporal solitons in microresonators driven by optical pulses. *Nature Photonics* **11** (2017), 600–607 (cited on pages 10, 34, 35, 66, 78).
- [38] Vladimir S. Ilchenko and Andrey B. Matsko. Optical resonators with whispering-gallery modes - Part II: Applications. *IEEE Journal on Selected Topics in Quantum Electronics* **12** (2006), 15–32 (cited on page 10).
- [39] Ki Youl Yang, Katja Beha, Daniel C. Cole, Xu Yi, Pascal Del’Haye, Hansuek Lee, Jiang Li, Dong Yoon Oh, Scott A. Diddams, Scott B. Papp, and Kerry J. Vahala. Broadband dispersion-engineered microresonator on a chip. *Nature Photonics* **10** (2016), 316–320 (cited on page 11).
- [40] Govind P. Agrawal. **Nonlinear Fiber Optics**. 4th. Burlington, MA: Elsevier, 2007 (cited on pages 11, 17, 19, 21, 28, 85, 106, 110, 111, 119).
- [41] Maria L Calvo and Vasudevan Lakshminarayanan, eds. **Optical Waveguides: From Theory to Applied Technologies**. Boca Raton, FL: Taylor & Francis, 2007 (cited on page 11).
- [42] A. N. Oraevsky. Whispering-gallery waves. *Quantum Electronics* **32** (2002), 377–400 (cited on page 12).
- [43] Hermann A. Haus. **Waves and Fields in Optoelectronics**. Englewood Cliffs: Prentice-Hall, 1984 (cited on pages 12, 13).
- [44] J. C. Knight, G. Cheung, F. Jacques, and T. A. Birks. Phase-matched excitation of whispering-gallery-mode resonances by a fiber taper. *Optics Letters* **22** (1997), 1129 (cited on page 14).
- [45] S. M. Spillane, T. J. Kippenberg, O. J. Painter, and K. J. Vahala. Ideality in a Fiber-Taper-Coupled Microresonator System for Application to Cavity Quantum Electrodynamics. *Physical review letters* **91** (2003), 043902 (cited on page 14).
- [46] Ehsan Shah Hosseini, Siva Yegnanarayanan, Amir Hossein Atabaki, Mohammad Soltani, and Ali Adibi. Systematic design and fabrication of high-Q single-mode pulley-coupled planar silicon nitride microdisk resonators at visible wavelengths. *Optics Express* **18** (2010), 2127 (cited on page 14).
- [47] Tal Carmon, Lan Yang, and Kerry J Vahala. Dynamical thermal behavior and thermal self-stability of microcavities. *Optics Express* **12** (2004), 4742–4750 (cited on page 15).
- [48] Raúl del Coso and Javier Solis. Relation between nonlinear refractive index and third-order susceptibility in absorbing media. *Journal of the Optical Society of America B* **21** (2004), 640 (cited on page 17).
- [49] Roger H. Stolen and John E. Bjorkholm. Parametric Amplification and Frequency Conversion in Optical Fibers. *IEEE Journal of Quantum Electronics* **18** (1982), 1062–1072 (cited on page 17).
- [50] T. Kippenberg, S. Spillane, and K. Vahala. Kerr-Nonlinearity Optical Parametric Oscillation in an Ultrahigh-Q Toroid Microcavity. *Physical Review Letters* **93** (2004), 083904 (cited on page 17).

- [51] Anatoliy A. Savchenkov, Andrey B. Matsko, Dmitry Strekalov, Makan Mohageg, Vladimir S. Ilchenko, and Lute Maleki. Low threshold optical oscillations in a whispering gallery mode CaF<sub>2</sub> resonator. *Physical Review Letters* **93** (2004), 243905 (cited on page 17).
- [52] Imad H. Agha, Yoshitomo Okawachi, Mark A. Foster, Jay E. Sharping, and Alexander L. Gaeta. Four-wave-mixing parametric oscillations in dispersion-compensated high- Q silica microspheres. *Physical Review A* **76** (2007), 043837 (cited on page 17).
- [53] T. Herr, V. Brasch, J. D. Jost, C. Y. Wang, N. M. Kondratiev, M. L. Gorodetsky, and T. J. Kippenberg. Temporal solitons in optical microresonators. *arXiv* (2012), 1211.0733 (cited on pages 18, 33).
- [54] T. Herr, V. Brasch, J. D. Jost, C. Y. Wang, N. M. Kondratiev, M. L. Gorodetsky, and T. J. Kippenberg. Temporal solitons in optical microresonators. *Nature Photonics* **8** (2014), 145–152 (cited on pages 18, 21, 31–33, 50, 73).
- [55] François Leo, Stéphane Coen, Pascal Kockaert, Simon-Pierre Gorza, Philippe Emplit, and Marc Haelterman. Temporal cavity solitons in one-dimensional Kerr media as bits in an all-optical buffer. *Nature Photonics* **4** (2010), 471–476 (cited on pages 18, 78).
- [56] T. Herr, K. Hartinger, J. Riemensberger, C. Y. Wang, E. Gavartin, R. Holzwarth, M. L. Gorodetsky, and T. J. Kippenberg. Universal formation dynamics and noise of Kerr-frequency combs in microresonators. *Nature Photonics* **6** (2012), 480–487 (cited on page 18).
- [57] Yanne K. Chembo and Curtis R. Menyuk. Spatiotemporal Lugiato-Lefever formalism for Kerr-comb generation in whispering-gallery-mode resonators. *Physical Review A* **87** (2013), 053852 (cited on page 19).
- [58] Stéphane Coen, Hamish G Randle, Thibaut Sylvestre, and Miro Erkintalo. Modeling of octave-spanning Kerr frequency combs using a generalized mean-field Lugiato-Lefever model. *Optics Letters* **38** (2013), 37–39 (cited on pages 19, 21, 22).
- [59] M. Haelterman, S. Trillo, and S. Wabnitz. Dissipative modulation instability in a nonlinear dispersive ring cavity. *Optics Communications* **91** (1992), 401–407 (cited on pages 19, 110).
- [60] T. Hansson, M. Bernard, and S. Wabnitz. Modulational Instability of Nonlinear Polarization Mode Coupling in Microresonators. *Journal of the Optical Society of America B* **35** (2018), 835–841 (cited on page 21).
- [61] Y. K. Chembo, I. S. Grudinin, and N. Yu. Spatiotemporal dynamics of Kerr-Raman optical frequency combs. *Physical Review A* **92** (2015), 043818 (cited on page 21).
- [62] Cyril Godey, Irina V. Balakireva, Aurélien Coillet, and Yanne K. Chembo. Stability analysis of the spatiotemporal Lugiato-Lefever model for Kerr optical frequency combs in the anomalous and normal dispersion regimes. *Physical Review A* **89** (2014), 063814 (cited on pages 22, 25).
- [63] I. V. Barashenkov and Yu S. Smirnov. Existence and stability chart for the ac-driven, damped nonlinear Schrödinger solitons. *Physical Review E* **54** (1996), 5707–5725 (cited on pages 22, 31).

- [64] A. Coillet and Y. K. Chembo. Routes to spatiotemporal chaos in Kerr optical frequency combs. *Chaos* **24** (2014), 013113 (cited on pages 25, 76).
- [65] L. A. Lugiato and R. Lefever. Spatial Dissipative Structures in Passive Optical Systems. *Physical Review Letters* **58** (1987), 2209–2211 (cited on pages 26, 28).
- [66] L. A. Lugiato and R. Lefever. Diffraction stationary patterns in passive optical systems. *Interaction of Radiation with Matter* (1987) (cited on page 26).
- [67] William H. Renninger and Peter T. Rakich. Closed-form solutions and scaling laws for Kerr frequency combs. *Scientific Reports* **6** (2016), 24742 (cited on page 26).
- [68] John Scott Russell. Report on Waves. *Fourteenth meeting of the British Association for the Advancement of Science* (1844), 311–390 (cited on page 28).
- [69] M. Brambilla, L. A. Lugiato, F. Prati, L. Spinelli, and W. J. Firth. Spatial soliton pixels in semiconductor devices. *Physical Review Letters* **79** (1997), 2042–2045 (cited on page 28).
- [70] S. Minardi, F. Eilenberger, Y. V. Kartashov, A. Szameit, U. Röpke, J. Kobelke, K. Schuster, H. Bartelt, S. Nolte, L. Torner, F. Lederer, A. Tünnermann, and T. Pertsch. Three-dimensional light bullets in arrays of waveguides. *Physical Review Letters* **105** (2010), 263901 (cited on page 28).
- [71] F. X. Kärtner, I. D. Jung, and U. Keller. Soliton mode-locking with saturable absorbers. *IEEE Journal on Selected Topics in Quantum Electronics* **2** (1996), 540–556 (cited on page 28).
- [72] P. Grelu and N. Akhmediev. Dissipative solitons for mode-locked lasers. *Nature Photonics* **6** (2012), 84–92 (cited on page 28).
- [73] L. F. Mollenauer and J. P. Gordon. **Solitons in Optical Fibers**. Academic Press, 2006, p. 296 (cited on page 28).
- [74] A. Hasegawa and Y. Kodama. **Solitons in Optical Communications**. Academic Press, 1995 (cited on page 28).
- [75] Hermann A. Haus and William S. Wong. Solitons in optical communications. *Reviews of Modern Physics* **68** (1996), 423–444 (cited on page 28).
- [76] Stéphane Coen and Miro Erkintalo. Universal scaling laws of Kerr frequency combs. *Optics Letters* **38** (2013), 1790–1792 (cited on page 31).
- [77] H. Guo, M. Karpov, E. Lucas, A. Kordts, M. H.P. Pfeiffer, V. Brasch, G. Lihachev, V. E. Lobanov, M. L. Gorodetsky, and T. J. Kippenberg. Universal dynamics and deterministic switching of dissipative Kerr solitons in optical microresonators. *Nature Physics* **13** (2017), 94–102 (cited on pages 31, 34).
- [78] N. J. Zabusky and M. D. Kruskal. Interaction of “solitons” in a collisionless plasma and the recurrence of initial states. *Physical Review Letters* **15** (1965), 240 (cited on page 31).
- [79] J. P. Gordon. Interaction forces among solitons in optical fibers. *Optics Letters* **8** (1983), 596–598 (cited on page 31).

- [80] Boris A. Malomed. Bound solitons in the nonlinear Schrodinger-Ginzburg-Landau equation. *Physical Review A* **44** (1991), 6954–6957 (cited on page 31).
- [81] J. K. Jang, M. Erkintalo, S. G. Murdoch, and S. Coen. Ultraweak long-range interactions of solitons observed over astronomical distances. *Nature Photonics* **7** (2013), 657–663 (cited on page 31).
- [82] Pedro Parra-Rivas, Damia Gomila, Pere Colet, and Lendert Gelens. Interaction of solitons and the formation of bound states in the generalized Lugiato-Lefever equation. *European Physical Journal D* **71** (2017), 198 (cited on pages 31, 32, 54).
- [83] Yadong Wang, Fran ois Leo, Julien Fatome, Miro Erkintalo, Stuart G. Murdoch, and St phane Coen. Universal mechanism for the binding of temporal cavity solitons. *Optica* **4** (2017), 855–863 (cited on pages 32, 54).
- [84] Victor Brasch, Tobias Herr, Michael Geiselmann, Grigoriy Lihachev, Martin H. P. Pfeiffer, Michael L. Gorodetsky, and Tobias J. Kippenberg. Photonic chip-based optical frequency comb using soliton Cherenkov radiation. *Science* **351** (2016), 357 (cited on page 34).
- [85] Jordan R. Stone, Travis C. Briles, Tara E. Drake, Daryl T. Spencer, David R. Carlson, Scott A. Diddams, and Scott B. Papp. Thermal and Nonlinear Dissipative-Soliton Dynamics in Kerr Microresonator Frequency Combs. *arXiv* (2017), 1708.08405 (cited on pages 34, 39).
- [86] V. E. Lobanov, G. V. Lihachev, N. G. Pavlov, A. V. Cherenkov, T. J. Kippenberg, and M. L. Gorodetsky. Harmonization of chaos into a soliton in Kerr frequency combs. *Optics Express* **24** (2016), 27382 (cited on pages 34, 35).
- [87] Chaitanya Joshi, Jae K. Jang, Kevin Luke, Xingchen Ji, Steven A. Miller, Alexander Klenner, Yoshitomo Okawachi, Michal Lipson, and Alexander L. Gaeta. Thermally controlled comb generation and soliton modelocking in microresonators. *Optics Letters* **41** (2016), 2565–2568 (cited on page 34).
- [88] Weiqiang Wang, Zhizhou Lu, Wenfu Zhang, Sai T. Chu, Brent E. Little, Leiran Wang, Xiaoping Xie, Mulong Liu, Qinghua Yang, Lei Wang, Jianguo Zhao, Guoxi Wang, Qibing Sun, Yuanshan Liu, Yishan Wang, and Wei Zhao. Robust soliton crystals in a thermally controlled microresonator. *Optics Letters* **43** (2018), 2002–2005 (cited on page 34).
- [89] Jae K. Jang, Miro Erkintalo, Stuart G. Murdoch, and St phane Coen. Writing and erasing of temporal cavity solitons by direct phase modulation of the cavity driving field. *Optics Letters* **40** (2015), 4755–4758 (cited on pages 34, 35).
- [90] Jae K. Jang, Miro Erkintalo, Stephane Coen, and Stuart G. Murdoch. Temporal tweezing of light through the trapping and manipulation of temporal cavity solitons. *Nature Communications* **6** (2015), 7370 (cited on pages 34, 35, 37, 43).
- [91] Yadong Wang, Bruno Garbin, Francois Leo, Stephane Coen, Miro Erkintalo, and Stuart G. Murdoch. Writing and Erasure of Temporal Cavity Solitons via Intensity Modulation of the Cavity Driving Field. *arXiv* (2018), 1802.07428 (cited on pages 34, 35).

- [92] Scott B. Papp, Katja Beha, Pascal Del'Haye, Franklyn Quinlan, Hansuek Lee, Kerry J. Vahala, and Scott A. Diddams. Microresonator frequency comb optical clock. *Optica* **1** (2014), 10–14 (cited on pages 34, 91).
- [93] Myoung Gyun Suh, Qi Fan Yang, Ki Youl Yang, Xu Yi, and Kerry J. Vahala. Microresonator soliton dual-comb spectroscopy. *Science* **354** (2016), 1–5 (cited on page 34).
- [94] Pablo Marin-Palomo, Juned N. Kemal, Maxim Karpov, Arne Kordts, Joerg Pfeifle, Martin H.P. Pfeiffer, Philipp Trocha, Stefan Wolf, Victor Brasch, Miles H. Anderson, Ralf Rosenberger, Kovendhan Vijayan, Wolfgang Freude, Tobias J. Kippenberg, and Christian Koos. Microresonator-based solitons for massively parallel coherent optical communications. *Nature* **546** (2017), 274–279 (cited on page 34).
- [95] J. D. Jost, T. Herr, C. Lecaplain, V. Brasch, M. H. P. Pfeiffer, and T. J. Kippenberg. Counting the cycles of light using a self-referenced optical microresonator. *Optica* **2** (2015), 706–711 (cited on page 34).
- [96] Pascal Del'Haye, Aurélien Coillet, Tara Fortier, Katja Beha, Daniel C. Cole, Ki Youl Yang, Hansuek Lee, Kerry J. Vahala, Scott B. Papp, and Scott A. Diddams. Phase-coherent microwave-to-optical link with a self-referenced microcomb. *Nature Photonics* **10** (2016), 1–5 (cited on page 34).
- [97] Victor Brasch, Erwan Lucas, John D. Jost, Michael Geiselmann, and Tobias J. Kippenberg. Self-referenced photonic chip soliton Kerr frequency comb. *Light: Science & Applications* **6** (2017), e16202 (cited on page 34).
- [98] Hossein Taheri, Ali A. Eftekhar, Kurt Wiesenfeld, and Ali Adibi. Soliton formation in whispering-gallery-mode resonators via input phase modulation. *IEEE Photonics Journal* **7** (2015), 2200309 (cited on pages 35, 36, 41).
- [99] Daniel C. Cole, Erin S. Lamb, Pascal Del'Haye, Scott A. Diddams, and Scott B. Papp. Soliton crystals in Kerr resonators. *Nature Photonics* **11** (2017), 671–676 (cited on page 48).
- [100] M. Zajnulina, M. Böhm, D. Bodenmüller, K. Blow, J.M. Chavez Boggio, A.A. Rieznik, and M.M. Roth. Characteristics and stability of soliton crystals in optical fibres for the purpose of optical frequency comb generation. *Optics Communications* **393** (2017), 95–102 (cited on page 48).
- [101] Adil Haboucha, Hervé Leblond, Mohamed Salhi, Andrey Komarov, and François Sanchez. Coherent soliton pattern formation in a fiber laser. *Optics Letters* **33** (2008), 524–526 (cited on page 48).
- [102] Foued Amrani, Mohamed Salhi, Philippe Grelu, Hervé Leblond, and François Sanchez. Universal soliton pattern formations in passively mode-locked fiber lasers. *Optics letters* **36** (2011), 1545–1547 (cited on page 48).
- [103] A. Haboucha, H. Leblond, M. Salhi, A. Komarov, and F. Sanchez. Analysis of soliton pattern formation in passively mode-locked fiber lasers. *Physical Review A* **78** (2008), 043806 (cited on page 48).

- [104] B A Malomed, A Schwache, and F Mitschke. Soliton lattice and gas in passive fiber-ring resonators. *Fiber and Integrated Optics* **17** (1998), 267–277 (cited on page 48).
- [105] F. Mitschke and A. Schwache. Soliton ensembles in a nonlinear resonator. *Journal of Optics B: Quantum and Semiclassical Optics* **10** (1998), 779–788 (cited on page 48).
- [106] A. Schwache and F. Mitschke. Properties of an optical soliton gas. *Physical Review E* **55** (1997), 7720–7725 (cited on page 48).
- [107] Pascal Del'Haye, Katja Beha, Scott B. Papp, and Scott A. Diddams. Self-Injection Locking and Phase-Locked States in Microresonator-Based Optical Frequency Combs. *Physical Review Letters* **112** (2014), 043905 (cited on page 48).
- [108] Pascal Del'Haye, Aurélien Coillet, William Loh, Katja Beha, Scott B. Papp, and Scott a. Diddams. Phase steps and resonator detuning measurements in microresonator frequency combs. *Nature Communications* **6** (2015), 5668 (cited on page 48).
- [109] Hermann A. Haus and Weiping Huang. Coupled-Mode Theory. *Proceedings of the IEEE* **79** (1991), 1505–1518 (cited on page 53).
- [110] A. A. Savchenkov, A. B. Matsko, W. Liang, V. S. Ilchenko, D. Seidel, and L. Maleki. Kerr frequency comb generation in overmoded resonators. *Optics Express* **20** (2012), 27290–27298 (cited on page 53).
- [111] T. Herr, V. Brasch, J. D. Jost, I. Mirgorodskiy, G. Lihachev, M. L. Gorodetsky, and T. J. Kippenberg. Mode Spectrum and Temporal Soliton Formation in Optical Microresonators. *Physical Review Letters* **113** (2014), 123901 (cited on page 53).
- [112] Yang Liu, Yi Xuan, Xiaoxiao Xue, Pei-Hsun Wang, Steven Chen, Andrew J. Metcalf, Jian Wang, Daniel E. Leaird, Minghao Qi, and Andrew M. Weiner. Investigation of mode coupling in normal-dispersion silicon nitride microresonators for Kerr frequency comb generation. *Optica* **1** (2014), 137–144 (cited on page 53).
- [113] Xiaoxiao Xue, Yi Xuan, Yang Liu, Pei-Hsun Wang, Steven Chen, Jian Wang, Dan E. Leaird, Minghao Qi, and Andrew M. Weiner. Mode-locked dark pulse Kerr combs in normal-dispersion microresonators. *Nature Photonics* **9** (2015), 594–600 (cited on page 53).
- [114] Chengying Bao, Yi Xuan, Daniel E. Leaird, Stefan Wabnitz, Minghao Qi, and Andrew M. Weiner. Spatial mode-interaction induced single soliton generation in microresonators. *Optica* **4** (2017), 1011 (cited on page 53).
- [115] T. Hansson and S. Wabnitz. Bichromatically pumped microresonator frequency combs. *Physical Review A* **90** (2014), 013811 (cited on page 54).
- [116] D. V. Skryabin and William J. Firth. Interaction of cavity solitons in degenerate optical parametric oscillators. *Optics Letters* **24** (1999), 1056–1058 (cited on page 54).
- [117] S. Wabnitz. Control of soliton train transmission, storage, and clock recovery by cw light injection. *Journal of the Optical Society of America B* **13** (1996), 2739–2749 (cited on page 54).
- [118] J. A. Barker and D. Henderson. What is “liquid”? Understanding the states of matter. *Reviews of Modern Physics* **48** (1976), 587–671 (cited on pages 57, 58).

- [119] Takeshi Egami and Simon Billinge. **Underneath the Bragg Peaks**. 2nd. Oxford, UK: Elsevier, 2012, p. 422 (cited on pages 57, 58).
- [120] Niel W. Ashcroft and David N. Mermin. **Solid State Physics**. 1st ed. Belmont, CA: Brooks/Cole, 1976, p. 826 (cited on page 60).
- [121] Andrew Weiner. **Ultrafast Optics**. 1st ed. Hoboken, NJ: Wiley, 2009, p. 598 (cited on page 63).
- [122] Daniel C. Cole, Alessandra Gatti, Scott B. Papp, Franco Prati, and Luigi Lugiato. Theory of Kerr frequency combs in Fabry-Perot resonators. *Physical Review A* (2018), accepted (cited on page 66).
- [123] W. Zhang, D. C. Cole, and S. B. Papp. Forthcoming (2018) (cited on page 78).
- [124] Su-Peng Yu and Scott B. Papp. Forthcoming (2018) (cited on page 79).
- [125] Daniel C. Cole, Katja M. Beha, Scott A. Diddams, and Scott B. Papp. Octave-spanning supercontinuum generation via microwave frequency multiplication. *Proceedings of the 8th Sympson on Frequency Standards and Metrology 2015, Journal of Physics: Conference Series* **723** (2016), 012035 (cited on pages 80, 104).
- [126] Katja Beha, Daniel C. Cole, Pascal Del'Haye, Aurélien Coillet, Scott A. Diddams, and Scott B. Papp. Electronic synthesis of light. *Optica* **4** (2017), 406–411 (cited on pages 80, 109).
- [127] T. Kobayashi, T. Sueta, Y. Cho, and Y. Matsuo. High-repetition-rate optical pulse generator using a Fabry-Perot electro-optic modulator. *Applied Physics Letters* **21** (1972), 341–343 (cited on page 80).
- [128] Motonobu Kourogi, Ken Nakagawa, and Motoichi Ohtsu. Wide-Span Optical Frequency Comb Generator for Accurate Optical Frequency Difference Measurement. *IEEE Journal of Quantum Electronics* **29** (1993), 2693–2701 (cited on page 80).
- [129] H. Murata, A. Morimoto, T. Kobayashi, and S. Yamamoto. Optical pulse generation by electrooptic-modulation method and its application to integrated ultrashort pulse generators. *IEEE Journal of Selected Topics in Quantum Electronics* **6** (2000), 1325–1331 (cited on page 80).
- [130] Takahide Sakamoto, Tetsuya Kawanishi, and Masayuki Izutsu. Asymptotic formalism for ultraflat optical frequency comb generation using a Mach-Zehnder modulator. *Optics Letters* **32** (2007), 1515–1517 (cited on page 80).
- [131] Isao Morohashi, Takahide Sakamoto, Hideyuki Sotobayashi, Tetsuya Kawanishi, Iwao Hosako, and Masahiro Tsuchiya. Widely repetition-tunable 200 fs pulse source using a Mach-Zehnder-modulator-based flat comb generator and dispersion-flattened dispersion-decreasing fiber. *Optics Letters* **33** (2008), 1192–1194 (cited on page 80).
- [132] A. Ishizawa, T. Nishikawa, A. Mizutori, H. Takara, S. Aozasa, A. Mori, H. Nakano, A. Takada, and M. Koga. Octave-spanning frequency comb generated by 250 fs pulse train emitted from 25 GHz externally phase-modulated laser diode for carrier-envelope-offset-locking. *Electronics Letters* **46** (2010), 1343 (cited on page 80).

- [133] Rui Wu, V. R. Supradeepa, Christopher M. Long, Daniel E. Leaird, and Andrew M. Weiner. Generation of very flat optical frequency combs from continuous-wave lasers using cascaded intensity and phase modulators driven by tailored radio frequency waveforms. *Optics Letters* **35** (2010), 3234 (cited on page 80).
- [134] V. R. Supradeepa and Andrew M. Weiner. Bandwidth scaling and spectral flatness enhancement of optical frequency combs from phase-modulated continuous-wave lasers using cascaded four-wave mixing. *Optics Letters* **37** (2012), 3066 (cited on page 80).
- [135] Andrew J. Metcalf, Victor Torres-Company, Daniel E. Leaird, and Andrew M. Weiner. High-Power Broadly Tunable Electrooptic Frequency Comb Generator. *IEEE Journal of Selected Topics in Quantum Electronics* **19** (2013), 3500306 (cited on page 80).
- [136] Rui Wu, Victor Torres-Company, Daniel E Leaird, and Andrew M Weiner. Supercontinuum-based 10-GHz flat-topped optical frequency comb generation. *Optics Express* **21** (2013), 6045–6052 (cited on page 80).
- [137] John M. Dudley, Goëry Genty, and Stéphane Coen. Supercontinuum generation in photonic crystal fiber. *Reviews of Modern Physics* **78** (2006), 1135–1184 (cited on pages 85, 100).
- [138] A. M. Weiner. Femtosecond pulse shaping using spatial light modulators. *Review of Scientific Instruments* **71** (2000), 1929–1960 (cited on page 85).
- [139] A. A. Amorim, M. V. Tognetti, P. Oliveira, J. L. Silva, L. M. Bernardo, F. X. Kärtner, and H. M. Crespo. Sub-two-cycle pulses by soliton self-compression in highly nonlinear photonic crystal fibers. *Optics Letters* **34** (2009), 3851–3853 (cited on page 87).
- [140] Gianni Di Domenico, Stéphane Schilt, and Pierre Thomann. Simple approach to the relation between laser frequency noise and laser line shape. *Applied Optics* **49** (2010), 4801–4807 (cited on page 89).
- [141] William C. Swann, Esther Baumann, Fabrizio R. Giorgetta, and Nathan R. Newbury. Microwave generation with low residual phase noise from a femtosecond fiber laser with an intracavity electro-optic modulator. *Optics Express* **19** (2011), 24387 (cited on page 91).
- [142] Jiang Li, Xu Yi, Hansuek Lee, Scott A. Diddams, and Kerry J. Vahala. Electro-optical frequency division and stable microwave synthesis. *Science* **345** (2014), 309–314 (cited on page 91).
- [143] Judah Levine. Introduction to time and frequency metrology. *Review of Scientific Instruments* **70** (1999), 2567–2596 (cited on page 93).
- [144] David R. Carlson, Daniel D. Hickstein, Daniel C. Cole, Scott A. Diddams, and Scott B. Papp. Dual-comb interferometry via repetition-rate switching of a single frequency comb. *arXiv* (2018), 1806.05311 (cited on page 94).

- [145] A. J. Metcalf, C. Bender, S. Blakeslee, W. Brand, D. Carlson, S. A. Diddams, C. Fredrick, S. Halverson, F. Hearty, D. Hickstein, J. Jennings, S. Kanodia, K. Kaplan, E. Lubar, S. Mahadevan, A. Monson, J. Ninan, C. Nitroy, S. Papp, L. Ramsey, P. Robertson, A. Roy, C. Schwab, K. Srinivasan, G. K. Stefansson, and R. Terrien. Infrared Astronomical Spectroscopy for Radial Velocity Measurements with 10 cm/s Precision. In: **Conference on Lasers and Electro-Optics**. 2018, JTh5A.1 (cited on page 94).
- [146] Daniel C. Cole, Scott B. Papp, and Scott A. Diddams. Downsampling of optical frequency combs. *Journal of the Optical Society of America B* **35** (2018), 1666–1673 (cited on page 95).
- [147] Sterling Backus, Charles G. Durfee, Margaret M. Murnane, and Henry C. Kapteyn. High power ultrafast lasers. *Review of Scientific Instruments* **69** (1998), 1207 (cited on page 95).
- [148] Andrius Baltuska, Matthias Uiberacker, Eleftherios Goulielmakis, Reinhard Kienberger, Vladislav S Yakovlev, Thomas Udem, Theodor W Hänsch, and Ferenc Krausz. Phase-Controlled Amplification of Few-Cycle Laser Pulses. *IEEE Journal of Selected Topics in Quantum Electronics* **9** (2003), 972–989 (cited on page 95).
- [149] Christoph Gohle, Jens Rauschenberger, Takao Fuji, Thomas Udem, Alexander Apolonski, Ferenc Krausz, and Theodor W Hänsch. Carrier envelope phase noise in stabilized amplifier systems. *Optics Letters* **30** (2005), 2487–2489 (cited on pages 96, 103).
- [150] J. Rauschenberger, T. Fuji, M. Hentschel, A.-J. Verhoef, T. Udem, C. Gohle, T. W. Hänsch, and F. Krausz. Carrier-envelope phase-stabilized amplifier system. *Laser Physics Letters* **3** (2006), 37–42 (cited on page 96).
- [151] M. E. Fermann, V. I. Kruglov, B. C. Thomsen, J. M. Dudley, and J. D. Harvey. Self-similar propagation and amplification of parabolic pulses in optical fibers. *Physical Review Letters* **84** (2000), 6010–6013 (cited on page 97).
- [152] Masaaki Hirano, Tetsuya Nakanishi, Toshiaki Okuno, and Masashi Onishi. Silica-Based Highly Nonlinear Fibers and Their Application. *IEEE Journal of Selected Topics in Quantum Electronics* **15** (2009), 103–113 (cited on pages 97, 119).
- [153] Dimitrios Mandridis, Ibrahim Ozdur, Franklyn Quinlan, Mehmetcan Akbulut, Jason J. Plant, Paul W. Juodawlkis, and Peter J. Delfyett. Low-noise, low repetition rate, semiconductor-based mode-locked laser source suitable for high bandwidth photonic analog – digital conversion. *Applied Optics* **49** (2010), 2850–2857 (cited on page 100).
- [154] Hans-A. Bachor and Peter J. Manson. Practical Implications of Quantum Noise. *Journal of Modern Optics* **37** (1990), 1727–1740 (cited on page 104).
- [155] Franklyn Quinlan, Tara M. Fortier, Haifeng Jiang, and Scott A. Diddams. Analysis of shot noise in the detection of ultrashort optical pulse trains. *Journal of the Optical Society of America B* **30** (2013), 1775–1785 (cited on page 104).
- [156] Alexander M. Heidt. Efficient Adaptive Step Size Method for the Simulation of Supercontinuum Generation in Optical Fibers. *Journal of Lightwave Technology* **27** (2009), 3984–3991 (cited on pages 106, 115, 116).

- [157] J. Hult. A Fourth-Order Runge-Kutta in the Interaction Picture Method for Simulating Supercontinuum Generation in Optical Fibers. *Journal of Lightwave Technology* **25** (2007), 3770–3775 (cited on pages 106, 115, 116, 119).
- [158] Rachid Driad, Josef Rosenzweig, Robert Elvis Makon, Rainer Lösch, Volker Hurm, Herbert Walcher, and Michael Schlechtweg. InP DHBT-Based IC Technology for 100-Gb / s Ethernet. *IEEE Trans. on Electron. Devices* **58** (2011), 2604–2609 (cited on page 109).
- [159] Damir Ferenci, Markus Grozing, Manfred Berroth, Robert Makon, Rachid Driad, and Josef Rosenzweig. A 25 GHz Analog Demultiplexer with a Novel Track and Hold Circuit for a 50 GS / s A / D-Conversion System in InP DHBT Technology. In: **Microwave Symposium Digest**. 2012, pp. 1–3 (cited on page 109).
- [160] Kensuke Ikeda. Multiple-valued stationary state and its instability of the transmitted light by a ring cavity system. *Optics Communications* **30** (1979), 257–261 (cited on page 111).
- [161] K. J. Blow and D. Wood. Theoretical description of transient stimulated Raman scattering in optical fibers. *IEEE Journal of Quantum Electronics* **25** (1989), 2665–2673 (cited on page 119).